Studying normal and cancer stem cells in the kidney using 3D organoids and genetic mouse models

Dissertation zur Erlangung des akademischen Grades

Doctor rerum naturalium (Dr. rer. nat.)

im Promotionsfach Biologie, Spezialisierung Biotechnologie

eingereicht an der Lebenswissenschaftlichen Fakultät
der Humboldt-Universität zu Berlin

von Adam Myszczyszyn
Master of Science (M.Sc.) Medizinische Biotechnologie

Präsidentin der Humboldt-Universität zu Berlin
Prof. Dr.-Ing. Dr. Sabine Kunst

Dekan der Lebenswissenschaftlichen Fakultät
Prof. Dr. Dr. Christian Ulrichs

Gutachter:
1. Prof. Dr. Walter Birchmeier
2. Prof. Dr. Achim Leutz
3. Prof. Dr. Michael Hummel

Tag der mündlichen Prüfung: 15.06.2021

Table of contents

Zusammenfassung ... 3
Summary ... 5
Introduction ... 8
1. Kidney tumorigenesis ... 8
1.1. Kidney cancer ... 8
1.1.1. Genetics and heterogeneity ... 8
1.1.2. Pseudo-hypoxia and dysregulated HIF-independent phenotypes upon VHL loss ... 9
1.1.3. Aggressiveness and treatment limitations ... 11
1.2. Cell of origin of kidney cancer ... 12
1.2.1. Normal adult kidney stem cells ... 12
1.2.2. Kidney cancer stem cells ... 13
1.2.3. Stem cell-associated Wnt and Notch signaling in kidney cancer ... 14
1.2.4. Genetic mouse models of kidney cancer ... 20
2. 3D organoids to study normal and cancer stem cells in the kidney ... 22
2.1. Adult stem cell-derived organoids ... 22
2.2. Organoids for cancer modeling ... 23
2.3. Normal and kidney cancer organoids ... 25
Aims of my study ... 27
Results ... 28
1. A long-term 3D tubuloid model of the adult mouse kidney ... 28
1.1. Growth of long-term 3D kidney tubuloid cultures ... 28
1.2. Kidney tubuloids resemble the adult mouse kidney epithelia, are stable over time and display enhanced proliferative capacity ... 28
1.3. Kidney tubuloids contain differentiated, polarized and functional tubular epithelial cells ... 29
1.4. Signaling systems, which control self-renewal, growth and differentiation of kidney tubuloids ... 32
2. Genetic mouse models with β-catenin-GOF, Notch-GOF and Vhl-LOF to study kidney tumorigenesis ... 57
2.1. Generation of the mutant mice ... 57
2.2. Doxycycline-induced recombination ... 58
2.3. Macroscopic phenotypes of the mutant mice ... 59
2.4. β-catenin, Notch and Vhl mutagenesis ... 59
2.5. No tumorigenesis was observed in the mutant kidneys ... 60
2.6. The mutant mice displayed hallmarks of chronic kidney disease ... 61
Discussion ... 80
A long-term 3D tubuloid model of the adult mouse kidney ... 80
Genetic mouse models with β-catenin-GOF, Notch-GOF and Vhl-LOF to study kidney tumorigenesis ... 83
Materials and methods ... 86
References ... 98
Acknowledgements ... 112
Selbstständigkeitserklärung ... 113

Zusammenfassung

Organoide aus adulten Mäusen sind vielversprechende Modelle für die Nierenforschung. Ihre Charakterisierung wurde jedoch nicht auf ein zufriedenstellendes Niveau gebracht. Hier habe ich 3D-Mausorganoide (Tubuloide) etabliert, die aus einzelnen Nierenepithelzellen in Matrigel unter serumfreien Bedingungen gezüchtet wurden. Die Tubuloidbildung in passagierten Kulturen war im Vergleich zu frisch ausgesäten Kulturen deutlich verstärkt, was auf die Fähigkeit der Tubuloid bildenden Zellen zur Selbsterneuerung hinweist. In Übereinstimmung mit der Anreicherung in Stamm- oder Vorläuferzellen zeigten die Tubuloide auch eine erhöhte Proliferationskapazität und die Hochregulation der Wnt-, Notch- und Yap-Signalsysteme. Die Kulturen konnten für mindestens 3,5 Monate seriell passagiert werden. Wir haben Tubuloidkomponenten durch proteomische und phosphoproteomische Ansätze, durch konfokale Mikroskopie und Elektronenmikroskopie sowie durch Immunfluoreszenz und Real-Time qPCR bestimmt. Die Tubuloide waren über die Zeit stabil und bezüglich des Proteoms und des Phosphoproteoms stark mit den adulten Nierenepithelien verwandt. Die Tubuloide enthielten differenzierte Epithelzellen, welche Polarität, komplexe interzelluläre Übergänge und Marker für proximale und distale Nephronlinien aufwiesen, was auf das Vorhandensein multipotenter Stamm- oder Vorläuferzellen hinweist. Funktionell zeigten die Tubuloide Endozytose und Empfindlichkeit gegenüber dem nephrotoxischen Arzneimittel Cisplatin. Die Aktivierung der EGF-Rezeptor- und Wnt-Signalübertragung sowie die Hemmung der TGFβ-Signalübertragung trieben die Bildung und das Wachstum der Tubuloide an, während Wnt allein Differenzierung kontrollierte. Insgesamt habe ich ein langfristiges 3D-Maus-Tubuloid-Modell etabliert und charakterisiert, das die Erneuerung und die Reparatur sowie die Architektur und die Funktionalität der adulten tubulären Epithelien rekapituliert. In der Zukunft wird das Modell detaillierte Untersuchungen der Trajektorien selbsterneuernder Zellen sowohl zur teilweisen Wiederherstellung der Niere als auch zur malignen Transformation der Niere ermöglichen.

Das klarzellige Nierenzellkarzinom (ccRCC) ist der häufigste und aggressivste Nierenkrebs. Die Inaktivierung des Tumorsuppressorgens Von Hippel-Lindau (*VHL*) ist der Haupttreiber des ccRCCs. Zuvor hatten wir die Hochregulation der Wnt- und Notch-Signalübertragung in den $CXCR4^{+}MET^{+}CD44^{+}$-Krebsstammzellen (CSC) aus primären humanen ccRCC-Tumoren identifiziert. Das Blockieren von Wnt und Notch in von Patienten stammenden Xenotransplantaten, Organoiden und nicht-anhaftenden Sphären unter Verwendung von niedermolekularen Inhibitoren beeinträchtigte die

Selbsterneuerung der CSC und das Tumorwachstum. Um CSC-gesteuertes humanes ccRCC in genetischen Mausmodellen nachzuahmen, begann ich mit der Erzeugung von zwei Doppelmausmutanten; β-Catenin-GOF; Notch-GOF und Vhl-LOF; β-Catenin-GOF. Die adulten tubulären Epithelien waren spezifische Ziele für die Rekombination unter Verwendung der induzierbaren LC1-Cre-Rekombinase, die abhängig vom Pax8-reversen Tetracyclin-kontrollierten Transaktivator (rtTA) war. Die LacZ-Färbung zeigte, dass die Rekombination proximale tubuläre Zellen umfasste, die Zellen des ccRCC-Ursprungs sind. Ich bestätigte die Mutagenese von β-Catenin-, Notch- und Vhl-loxP-Allelen auf DNA-Ebene, mRNA-Zielgen-Ebene und Protein-Ebene. Sowohl die β-Catenin-GOF; Notch-GOF Mausmutante als auch die Vhl-LOF; β-Catenin-GOF Mausmutante entwickelten innerhalb einiger Monate schwere Krankheitssymptome. Überraschenderweise beobachtete ich weder Tumore oder Tumorvorläuferläsionen noch höhere Zellproliferationsraten in den mutierten Nieren. Weitere Analysen ergaben, dass die Mausmutanten Merkmale chronischer Nierenerkrankung (CKD) aufwiesen. Somit entwickelten die β-Catenin-GOF; Notch-GOF und Vhl-LOF; β-Catenin-GOF Mausmutanten unter den gegebenen Versuchsbedingungen keine Nierentumore.

Summary

Adult mouse organoids are promising models for kidney research. However, their characterization has not been pushed forward to a satisfying level. Here, I have established 3D mouse organoids (tubuloids) grown from single kidney epithelial cells in Matrigel under serum-free conditions. Tubuloid formation in passaged cultures was strongly enhanced in comparison to freshly seeded cultures, indicating the self-renewal ability of tubuloid-forming cells. In line with the enrichment in stem or progenitor cells, the tubuloids also displayed elevated proliferative capacity and the upregulation of the Wnt, Notch and Yap signaling systems. The cultures could be serially passaged for at least 3.5 months. We determined tubuloid components by proteomic and phosphoproteomic approaches, by confocal and electron microscopy and by immunofluorescence and real-time qPCR. The tubuloids were stable over time and greatly shared the proteome and phosphoproteome with the adult kidney epithelia. The tubuloids contained differentiated epithelial cells, which exhibited polarity, complex intercellular junctions and markers of proximal tubule and distal nephron lineages, suggesting the presence of multipotent stem or progenitor cells. Functionally, the tubuloids displayed endocytosis and sensitivity to nephrotoxic cisplatin. Activation of the EGF receptor and Wnt signaling and inhibition of TGFβ signaling drove tubuloid formation and growth, while Wnt alone controlled differentiation. Altogether, I generated and characterized a long-term 3D mouse tubuloid model, which recapitulates renewal and repair, and the architecture and functionality of the adult tubular epithelia. In the future, the model will allow detailed investigations of trajectories of self-renewing cells towards both the partial recreation and malignant transformation of the kidney.

Clear cell renal cell carcinoma (ccRCC) is the most common and aggressive kidney cancer. Inactivation of the Von Hippel-Lindau (*VHL*) tumor suppressor gene is the major driver of ccRCC. Earlier, we identified the upregulation of Wnt and Notch signaling in $CXCR4^{+}MET^{+}CD44^{+}$ cancer stem cells (CSCs) from primary human ccRCCs. Blocking Wnt and Notch in patient-derived xenografts, organoids and non-adherent spheres using small-molecule inhibitors impaired self-renewal of CSCs and tumor growth. To mimic CSC-governed human ccRCC in genetic mouse models, I started from the generation of two double mouse mutants; β-catenin-GOF; Notch-GOF and Vhl-LOF; β-catenin-GOF. The adult tubular epithelia were specific targets for recombination using the inducible Pax8-reverse tetracycline-controlled transactivator (rtTA)-dependent LC1-Cre recombinase. LacZ staining showed that recombination encompassed proximal tubular cells, which are the cells of ccRCC origin. I confirmed mutagenesis of β-catenin-, Notch-

and Vhl-loxP alleles on DNA, mRNA target gene and protein levels. Both β-catenin-GOF; Notch-GOF and Vhl-LOF; β-catenin-GOF mouse mutants developed severe symptoms of sickness within several months. Surprizingly, I observed neither tumors or tumor precursor lesions nor higher cell proliferation rates in the mutant kidneys. Further analyses revealed that the mutant mice displayed features of chronic kidney disease (CKD). Thus, β-catenin-GOF; Notch-GOF and Vhl-LOF; β-catenin-GOF mouse mutants did not develop kidney tumors under the given experimental conditions.

The present dissertation has been carried out under the supervision of Prof. Dr. Walter Birchmeier in the laboratory of Signal Transduction in Development and Cancer at the Max Delbrück Center for Molecular Medicine (MDC) in the Helmholtz Association in Berlin.

Introduction

1. Kidney tumorigenesis

1.1. Kidney cancer

1.1.1. Genetics and heterogeneity

In the USA in 2021, kidney cancer is expected to represent the 6th most common malignancy in men (accounting for 5% of all male cancer cases) and the 9th in women (accounting for 3% of all female cancer cases) (Siegel *et al*, 2021). Renal cell carcinoma (RCC) constitutes more than 90% of kidney cancers. Clear cell renal cell carcinoma (ccRCC) is the most frequent subtype of RCC, which affects more than 80% of patients (Hsieh *et al*, 2017). High-throughput genome sequencing revealed that biallelic disruption of the Von Hippel-Lindau (*VHL*) tumor suppressor gene occurs in the majority of ccRCC cases. The loss of one copy of *VHL* in 91-95% of patients results from the loss of chromosome 3p, where *VHL* is located. The second copy is inactivated through either mutation in 52-82% of cases or promoter methylation in 7-16% of cases. 3p loss encloses three further tumor suppressor genes, *PBRM1*, *SETD2* and *BAP1*, whose second copy is also often mutated. Further tumor suppressor genes such as *KDM5C*, *PTEN*, *MTOR*, *P53* and *PIK3CA* are less frequently mutated. Other common genetic alterations are the gain of 5q chromosome, and 14q and 9p loss (Creighton *et al*, 2013; Sato *et al*, 2013; Turajlic *et al*, 2018b) (Figure 1). Subsequent genome sequencing of multiple tumor regions deciphered evolutionary trajectories of primary and metastatic ccRCCs. *VHL* inactivation is the ubiquitous earliest clonal event in tumorigenesis, and subclonal alterations of other genes and chromosomes occur in spatially separated tumor regions. This branched evolution contributes to intratumor heterogeneity of ccRCCs, which hinders the validation of molecular biomarkers in personalized treatment (Gerlinger *et al*, 2012, 2014; Mitchell *et al*, 2018; Turajlic *et al*, 2018a, 2018b).

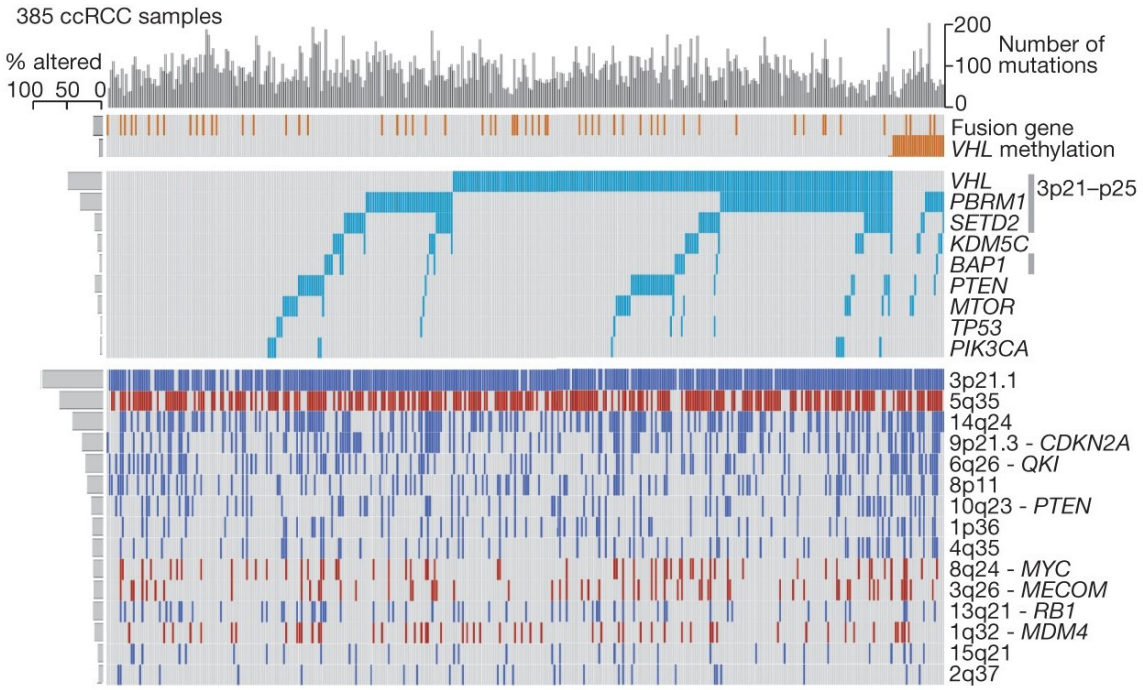

Figure 1

Genetic alterations in human ccRCC. Top histogram: number of mutations per sample. Histograms below: distribution and frequency of gene fusions, *VHL* methylation, gene mutations and chromosomal copy number losses and gains across 385 ccRCC samples from The Cancer Genome Atlas (TCGA) cohort (Creighton *et al*, 2013).

1.1.2. Pseudo-hypoxia and dysregulated HIF-independent phenotypes upon VHL loss

The product of the *VHL* gene plays a key role in cellular oxygen sensing. VHL is the substrate recognition subunit of an E3 ubiquitin ligase complex for the hypoxia-inducible factors-1α and -2α (HIF-1α/2α), which are constitutively expressed. This complex also contains CUL2, ELOB, ELOC and RBX1. In the presence of oxygen and 2OG, critical proline residues of HIF-1α/2α are hydroxylated by the EGLN family of evolutionarily conserved dioxygenases. This allows recognition of HIF-1α/2α by VHL, which results in their ubiquitination by the E3 ligase complex and proteasomal degradation. In hypoxic conditions, HIF-1α/2α are not hydroxylated, and thus escape recognition and ubiquitination by the VHL E3 ligase complex. This leads to accumulation of HIF-1α/2α and their heterodimerization with HIF-1β, which is constantly present in the cytoplasm. HIF-1α/2α-HIF-1β heterodimers translocate to the nucleus and bind to the hypoxia response elements (HRE) to regulate the expression of hundreds of HIF target genes involved in cellular adaptations to hypoxia such as anaerobic glycolysis, angiogenesis, proliferation, survival and motility (Bertout *et al*, 2008; Gossage *et al*, 2015; Lindgren *et al*, 2018) (Figure 2). For their seminal discoveries on how cells sense and respond to

oxygen availability via the VHL-HIF axis, Kaelin, Ratcliffe and Semenza jointly won the 2019 Nobel Prize in Physiology or Medicine (Ledford & Callaway, 2019).

VHL-deficient ccRCCs display lack of oxygen sensing. This results in the pseudo-hypoxic state with stabilization of HIF-1α/2α, followed by the hyperactivation of HIF targets, which contribute to tumor initiation and progression (Bertout *et al*, 2008; Gossage *et al*, 2015; Lindgren *et al*, 2018) (Figure 2). However, accumulated evidence on the role of HIF-1α and -2α in ccRCC tumorigenesis is inconsistent. Genetic studies using ccRCC xenografts indicated the oncogenic role of HIF-2α (Schödel *et al*, 2016). In addition, treatment with a small-molecule antagonist of HIF-2α in two preclinical studies inhibited tumor growth in xenografts derived from ccRCC patients and cell lines. These studies validated previously undruggable HIF-2α as the target for anti-ccRCC therapy (Chen *et al*, 2016b; Cho *et al*, 2016). In a subsequent clinical trial of a close analogue of the HIF-2α antagonist, mostly stable disease, but also partial and complete responses were achieved in patients with heavily pretreated advanced or metastatic ccRCCs (Courtney *et al*, 2018). In turn, in studies using ccRCC xenografts, investigators argued that HIF-1α plays the tumor suppressive function (Schödel *et al*, 2016). In contrast, several studies using genetic mouse models suggested that HIF-1α is an oncogene, while HIF-2α was not essential for ccRCC formation (Hoefflin *et al*, 2020; Nanus & Gudas, 2016). Another study in mice indicated that both HIF-1α and -2α are necessary for ccRCC development (Schönenberger *et al*, 2016). These differing effects of HIF-1α and -2α in ccRCC xenografts, genetic mouse models and patients appear context-dependent and are a matter of discussion in the field (Hoefflin *et al*, 2020; Nanus & Gudas, 2016; Schödel *et al*, 2016). VHL also exhibits numerous HIF-independent tumor suppressive functions such as direct or indirect β-catenin ubiquitination, extracellular matrix regulation, microtubule stabilization, intercellular junction formation, apoptosis induction by P53 activation and NF-κB inhibition, cell senescence control and transcriptional regulation. A complete understanding of VHL loss-driven ccRCC tumorigenesis will require the elucidation of the interplay between dysregulated HIF-dependent and -independent processes (Calzada *et al*, 2006; Chitalia *et al*, 2008; Gossage *et al*, 2015; Peruzzi *et al*, 2006; Young *et al*, 2008; Zhang *et al*, 2018).

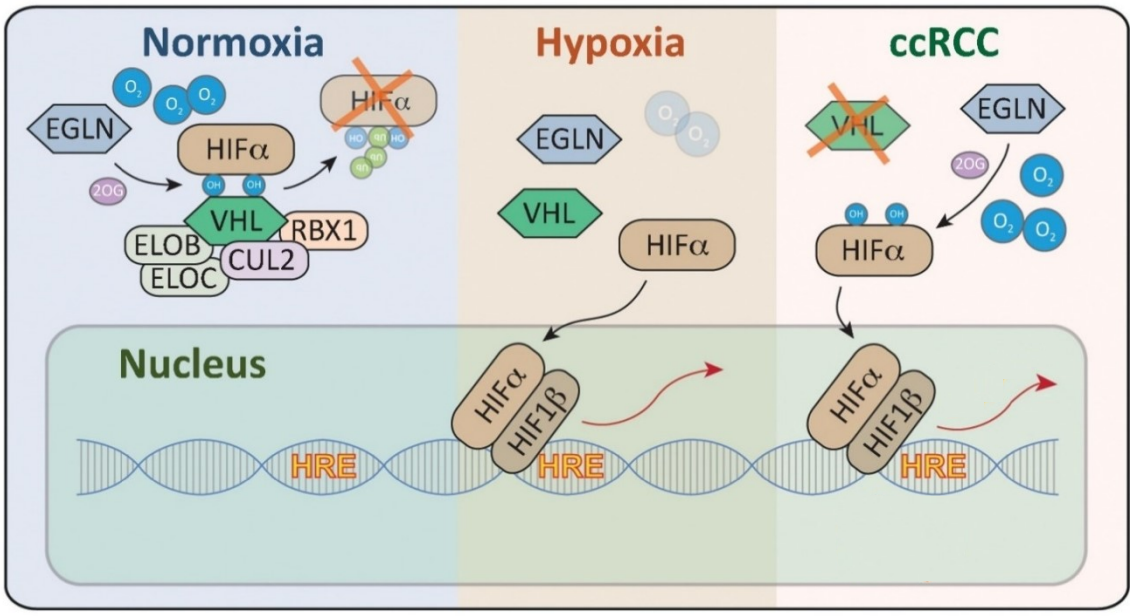

Figure 2

VHL-HIF signaling in normoxia, hypoxia and pseudo-hypoxia of ccRCC (Lindgren *et al*, 2018).

1.1.3. Aggressiveness and treatment limitations

65% of ccRCC patients are diagnosed with localized tumors, 16% with lymph node involvement and 16% with metastases (Siegel *et al*, 2021). Despite radical or partial nephrectomy with curative intent, 30% of patients with localized ccRCCs finally develop metastases (Hsieh *et al*, 2017). Over the past two decades, targeted treatment based on small-molecule inhibitors of multiple tyrosine kinases such as the VEGF and PDGF receptor, on mTOR inhibitors, on an anti-VEGF monoclonal antibody and on immune-checkpoint inhibitors significantly improved outcomes of patients with metastatic ccRCCs. However, durable complete responses are rare, and most patients with partial remission or stable disease experience tumor relapse due to acquired resistance (Kotecha *et al*, 2019; Posadas *et al*, 2017). Therefore, the 5-year survival rate for patients with metastatic ccRCCs lies at only 13% (Siegel *et al*, 2021). This makes ccRCC the most aggressive subtype of RCC (Hsieh *et al*, 2017). The reason for treatment failure and poor prognosis is incomplete understanding of ccRCC tumorigenesis, which results in therapies not sufficiently tailored to molecular driver mechanisms. Improving patient outcomes requires the development of new disease-relevant preclinical models to further explore and inhibit clonal founder events of ccRCC and their functional downstream oncogenic mediators and to establish biomarkers of drug response for clinical trials. Besides patients with metastatic tumors, these driver-targeted therapies should also be investigated in patients with localized tumors in the neo-adjuvant or adjuvant setting to prevent metastatic dissemination after nephrectomy.

1.2. Cell of origin of kidney cancer

1.2.1. Normal adult kidney stem cells

The kidney is made up of about one million nephrons. The nephron is a highly complex structural and functional unit of the kidney, which originates in the cortex and stretches out into the medulla (Figure 3). The cortical nephron consists of the Bowman's capsule with the glomerulus, which produces the primary urine by filtering the blood, followed by the proximal convoluted tubule, Loop of Henle composed of three limbs, distal convoluted tubule, connecting tubule and collecting duct, which reabsorb important substances from the primary urine and concentrate it. The medullary collecting duct directs the urine to the pelvis and ureter. The nephron segments contain about 25 different cell types with specialized functions (Lindgren *et al*, 2018).

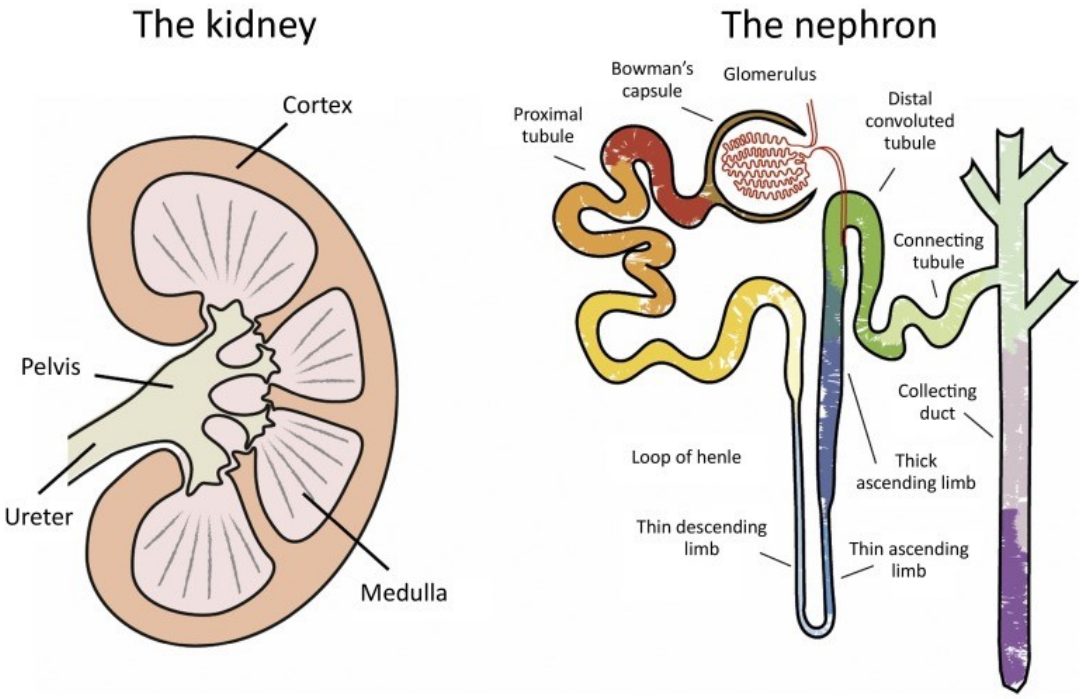

Figure 3

The segmented architecture of the kidney and nephron (Lindgren *et al*, 2018).

The kidney has a great capacity to regenerate following injury, but factors governing this response are largely unknown. Lineage tracing revealed the presence of multipotent Lgr5-positive stem cells in the developing mouse kidney. Unlike in other organs, Lgr5 expression is permanently silenced in the adult kidney (Barker *et al*, 2012). A number of putative populations of multipotent stem or progenitor cells were described in the adult human kidney based on the expression of the CD133, CD24, CD106 and CD146 surface markers in different combinations, but the studies lack strong experimental proof of

functional stemness properties of these cells (Angelotti *et al*, 2012; Bruno & Camussi, 2012; Bussolati *et al*, 2005; Sagrinati *et al*, 2006). In addition, lineage tracing of Cd133-positive cells in the mouse kidney questioned their stem or progenitor cell characteristics, because these cells display limited generative capacity in the postnatal kidney and are quiescent in the adult kidney (Zhu *et al*, 2016). However, fast-cycling, multi-lineage Sox9-positive progenitors drive the repair of proximal tubule, Loop of Henle and distal tubule cells in the adult mouse kidney (Kang *et al*, 2016). Another mouse study revealed that Sox9-positive progenitors exclusively contribute to the proximal tubule lineage during repair (Kumar *et al*, 2015). Troy-positive unipotent progenitors, which reside in the developing mouse papilla, can regenerate adult collecting duct cells only to certain extent (Schutgens *et al*, 2017). In turn, a study in *Rainbow* mice demonstrated that adult unipotent progenitors specific for the proximal, distal or collecting duct segment exist, but no markers were defined. These progenitors drive both homeostatic maintenance and repair of the kidney (Rinkevich *et al*, 2014). As an alternative to resident stem or progenitor cells, a plastic process of injury-induced dedifferentiation, proliferation and redifferentiation of survived terminally specialized proximal tubular cells was proposed to contribute to repair of the adult mouse kidney (Kusaba *et al*, 2014). The unresolved questions regarding the biology of stem or progenitor cells in the adult kidney remain a matter of debate in the field.

1.2.2. Kidney cancer stem cells

Correlative studies on cancer patients revealed that during the life of individuals, the number of stem cell divisions in self-renewing tissues dictate the cancer risk by accumulated driver gene mutations, which randomly result from these divisions. Approximately three mutations occur during a division of a human stem cell (Tomasetti *et al*, 2017). Mouse models confirmed that the generative capacity of mutated stem cells determines the life-long tumor incidence in many organs (Zhu *et al*, 2016). It is believed that transformed stem cells are the source of intratumor heterogeneity and thus crucial units of Darwinian selection. These so-called cancer stem cells (CSCs), also called tumor-initiating cells or tumor-propagating cells, are non-genetic determinants of hierarchically organized cancer tissues, which can be integrated in the genetic clonal evolution paradigm and can contribute to tumor initiation and progression (Kreso & Dick, 2014). According to the CSC concept, a small population of tumor cells exhibits an extraordinary capacity for initiation and long-term maintenance of primary tumors and metastases. This is due to unlimited potential for self-renewal and differentiation towards heterogeneous progeny, which form the tumor bulk. Because solid tumors display features of the organization of normal self-renewing tissues, the development of these

tumors is considered as the caricature of organogenesis. However, for most solid tumors, the cellular origin, plasticity and stemness-governing signaling systems of individual CSC populations have not yet been elucidated. Subcutaneous and orthotopic xenotransplantation at limiting dilutions into immunodeficient mice is a standard functional assay to examine the capacity of FAC-sorted human CSCs to recapitulate parental tumors over serial passages (Batlle & Clevers, 2017; Lytle *et al*, 2018; Nassar & Blanpain, 2016; Shibue & Weinberg, 2017; Visvader & Lindeman, 2012).

Several studies on putative CSCs from human ccRCCs were performed (Hu *et al*, 2017; di Martino *et al*, 2018; see also my review: Myszczyszyn *et al*, 2015). These studies aimed at the enrichment of CSCs based on single markers such as CXCR4, CD105, ALDH or CTR2 and the combination of CD44, CD146 and EpCAM, but suffered from experimental limitations and inconsistency. In contrast, we identified $CXCR4^{+}MET^{+}CD44^{+}$ CSCs from primary human ccRCCs. We confirmed the self-renewal and tumorigenic capacity of these CSCs in complementary patient-derived functional models, i.e. subcutaneous and orthotopic xenografts, and organoids and non-adherent spheres in culture (Fendler, Myszczyszyn *et al*, 2020).

1.2.3. Stem cell-associated Wnt and Notch signaling in kidney cancer

In the past 40 years, Wnt has emerged as a fundamental and ancient signal transduction system during development and adult life, which is involved in the regulation of cell fate (van Amerongen, 2020; Grigoryan *et al*, 2008; Klaus & Birchmeier, 2008; Nusse & Clevers, 2017; Wiese *et al*, 2018). The transcriptional coactivator β-catenin is the key mediator of canonical Wnt signaling, and our laboratory contributed to the discoveries of the mechanisms of the β-catenin signal cascade (Behrens *et al*, 1996, 1998). This protein moves from adherens junctions between the membranes of neighboring cells (Hülsken *et al*, 1994; Takeichi, 1991) to the cytoplasm and nucleus. In the Wnt-off state of resting cells, the cytoplasmic pool of β-catenin is phosphorylated by the so-called destruction complex composed of the tumor suppressor proteins Axin1/2 and Apc and of the kinases Ck1 and Gsk3β. Phosphorylated β-catenin is targeted by ubiquitination for proteasome-mediated degradation (Behrens *et al*, 1998). In the Wnt-on state, Wnt ligands, which are secreted glycoproteins palmitoylated by the membrane O-acyltransferase Porcn, bind to Frizzled receptors and Lrp co-receptors at the cell surface (Nusse & Clevers, 2017; Wiese *et al*, 2018), which results in Dishevelled (Dvl)-mediated disassembly of the destruction complex (Schwarz-Romond *et al*, 2007). Non-phosphorylated β-catenin accumulates in the cytoplasm and translocates into the nucleus, where it binds to the Tcf/Lef family of transcription factors, and this complex

drives the transcription of context-dependent Wnt target genes (Behrens *et al*, 1996; Molenaar *et al*, 1996). Active Wnt signaling is controlled by numerous negative feedback regulators, which include the secreted Wnt antagonists Dkk, Igfbp, Sfrp and Wif (Cruciat & Niehrs, 2013; Nusse & Clevers, 2017) as well as the membrane E3 ubiquitin ligases Rnf43 and Znr43, which promote the internalization of the Frizzled-Lrp complexes. The negative feedback by Rnf43 and Znr43 is blocked by the secreted R-spondin agonists, which bind to Lgr receptors. The Lgr-R-spondin complexes mediate the clearance of Rnf43 and Znr43 from the membrane (de Lau *et al*, 2014).

Notch is an evolutionarily conserved multi-faceted signaling system, which is crucial for fetal and adult tissues (Kopan & Ilagan, 2009; Ntziachristos *et al*, 2014; Siebel & Lendahl, 2017). Canonical Notch signaling is activated by the interaction of Jag or Dll ligands at the surface of signal-sending cells with Notch receptors of signal-receiving cells, which are presented on the membrane after the S1 cleavage in the Golgi apparatus. This interaction induces the S2 cleavage by Adam metalloproteinases, followed by the S3 cleavage by the γ-secretase complex composed of Psen1/2, Pen2, Aph1 and Ncstn. The cleaved Notch intracellular domain (Nicd) is transported to the nucleus, where it forms a transcriptional complex with the coactivators Rbpj and Maml. This complex mediates the transcription of pleiotropic Notch downstream effectors. Notch signaling is regulated by various post-translational modifications of its receptors and ligands (Kopan & Ilagan, 2009; Ntziachristos *et al*, 2014; Siebel & Lendahl, 2017).

Wnt and Notch signaling regulate maintenance, migration, differentiation and lineage commitment of stem cells in embryogenesis and in homeostasis and regeneration of adult organs (Grigoryan *et al*, 2008; Klaus & Birchmeier, 2008; Koch *et al*, 2013; Liu *et al*, 2010; Siebel & Lendahl, 2017; Wiese *et al*, 2018). Wnt and Notch signaling play critical roles in kidney development. Wnt induces mesenchymal-to-epithelial transition, i.e. differentiation of mesenchymal cells into epithelial cells, which initiates nephron formation. Notch acts later in nephron segmentation by patterning proximal tubules and glomerular cells (Edeling *et al*, 2016; Little & Kairath, 2017). While Wnt and Notch are silenced in the kidney once nephrogenesis is completed, it was proposed that kidney repair is regulated by the reactivation of developmental signaling systems (Little & Kairath, 2017). Indeed, Wnt and Notch are upregulated in Sox9-positive multipotent progenitor cells, which expand in response to kidney injury in mice (Kang *et al*, 2016). In addition, Wnt-responsive unipotent progenitor cells contribute to regeneration of proximal tubules and collecting ducts in the mouse kidney (Rinkevich *et al*, 2014). Consistent with these findings, deletion of the Wnt mediator β-catenin in kidney tubular cells (Zhou *et al*,

2012) or knockout of the Wnt ligand Wnt7b in inflammatory macrophages (Lin *et al*, 2010) as well as blocking Notch with a γ-secretase inhibitor (Chen *et al*, 2013) delay kidney recovery upon injury in mice.

According to Vogelstein and colleagues, Wnt and Notch are among cell fate-controlling oncogenic signaling systems, which are activated by mutations of known driver genes (Vogelstein *et al*, 2013). Driver genes encoding components and regulators of Wnt and Notch can not only be recurrently mutated, amplified or lost, but also epigenetically modified in a number of solid tumors, which results in the upregulation of these signaling systems, followed by the unbalance of self-renewal, motility, proliferation and differentiation of stem cells and tumorigenesis (Bugter *et al*, 2021; Jung & Park, 2020; Lytle *et al*, 2018; Meisel *et al*, 2020; Ntziachristos *et al*, 2014; Ranganathan *et al*, 2011; Siebel & Lendahl, 2017; Wiese *et al*, 2018).

To study the causative role of Wnt signaling in the development of breast and salivary gland cancer, our laboratory generated genetic mouse models, which were driven by CSCs dependent on β-catenin hyperactivation (Holland *et al*, 2013; Wend *et al*, 2013). In addition, we showed that knockout of the epigenetic regulator Mll1 in the salivary gland cancer model (Zhu *et al*, 2019) and in a Wnt-high model of colorectal cancer (Grinat *et al*, 2020) as well as deletion of Yap in the breast cancer model (Quinn *et al*, 2021) resulted in the loss of self-renewal of CSCs and impaired tumor formation. Thus, our results indicate that Mll1 and Yap are essential mediators of Wnt-induced CSC-governed tumorigenesis. Furthermore, single cell RNA sequencing in our genetic mouse model of salivary gland cancer revealed that tumor development proceeds through heterogeneous subpopulations of CSCs, which display basal or luminal identity and different levels of Wnt signaling (Praktiknjo *et al*, 2020). Remarkably, γ-secretase inhibition of Notch signaling in mouse intestinal adenomas with genetic upregulation of Wnt signaling revealed that Notch cooperates with Wnt in the maintenance of an undifferentiated, proliferative premalignant phenotype (van Es *et al*, 2005). In another genetic mouse model of colorectal cancer, concomitant genetic hyperactivation of Nicd and knockout of p53 contributed to the formation of metastatic tumors (Chanrion *et al*, 2014).

The results of our laboratory and of other groups support the importance of the Wnt and Notch signaling systems also in ccRCC tumorigenesis. Mutations of Wnt and Notch signaling components are rare in ccRCCs (Creighton *et al*, 2013; Kandoth *et al*, 2013; Kim *et al*, 2000; Sanchez-Vega *et al*, 2018; Sato *et al*, 2013). However, the overexpression of mediator molecules of Wnt (Hsu *et al*, 2012; Janssens *et al*, 2004; Kim

et al, 2000; Kruck *et al*, 2013; Lian *et al*, 2012) and Notch (Ai *et al*, 2012; Bhagat *et al*, 2017; Johansson *et al*, 2016; Lee *et al*, 2016; Liu *et al*, 2013; Sjölund *et al*, 2008; Wang *et al*, 2014b; Wu *et al*, 2011) in primary ccRCCs and ccRCC cell lines was demonstrated. Widespread activation of Notch in The Cancer Genome Atlas (TCGA) RNA sequencing data sets from ccRCC samples was also observed (Bhagat *et al*, 2017; Johansson *et al*, 2016). In addition, our laboratory identified the upregulation of Wnt and Notch in $CXCR4^{+}MET^{+}CD44^{+}$ CSCs from primary ccRCCs by gene expression profiling and single cell RNA sequencing (Fendler, Myszczyszyn *et al*, 2020).

Several genetic and epigenetic mechanisms were described, which lead to the activation of Wnt and Notch signaling in ccRCCs. Based on the analysis of ccRCC samples from the TCGA cohort, a core signature of 16 frequently amplified genes involved in Wnt signaling was linked to transcriptional upregulation of Wnt (Chang & Lai, 2019). Moreover, the Wnt antagonists SFRP1/2/4/5 and WIF1 as well as the LRP5/6 antagonists DKK1-3 and IGFBP1 are frequently downregulated in ccRCCs by promoter hypermethylation, which results in the loss of negative upstream regulation of Wnt signaling, followed by β-CATENIN liberation (Joosten *et al*, 2018; Morris & Latif, 2017; Saini *et al*, 2011). In addition, the promoter of the *APC* gene is hypermethylated in up to 54% of ccRCCs, which blocks the formation of the β-CATENIN destruction complex (Joosten *et al*, 2018; Morris & Latif, 2017). Also, hypermethylation of SLIT-2 and its receptor ROBO1 in a subset of ccRCCs inhibits GSK-3β, preventing phosphorylation and ubiquitination of β-CATENIN (Joosten *et al*, 2018; Morris & Latif, 2017). Furthermore, we proposed that kidney CSCs use autocrine mechanisms to upregulate Wnt signaling, as shown by higher secretion of WNT10A (Fendler, Myszczyszyn *et al*, 2020). WNT10A was suggested as an oncogenic Wnt ligand in ccRCC (Hsu *et al*, 2012), but it has not been linked with kidney CSCs so far. Notch gene sets are altered in almost half of ccRCC patients from the TCGA cohort. Copy number variations of the Notch coactivators MAML1 and KAT2B are predominant alterations, which occur in 19% and 13% of patients, respectively (Feng *et al*, 2016). In addition, the overexpression of the Notch ligands JAG1 and JAG2 is associated with gene amplification and hypomethylation of H3K4me1-associated enhancer regions in ccRCCs (Bhagat *et al*, 2017). Moreover, the E3 ubiquitin ligase NEURL, which negatively regulates Notch ligands, is inactivated by promoter methylation in about 50% of ccRCCs (Schouten *et al*, 2016; van Vlodrop *et al*, 2017). We showed that Notch signaling in kidney CSCs is promoted downstream of Wnt signaling, likely via JAG1 activation (Fendler, Myszczyszyn *et al*, 2020).

In context-dependent manners, both Wnt and Notch signaling can be enhanced upon VHL disruption, and vice versa, Wnt and Notch can potentiate hypoxia signaling. HIF-1α modulates Wnt signaling in hypoxic embryonic stem cells (ESCs) by enhancing β-CATENIN activation and expression of the transcriptional Wnt coactivators TCF1 and LEF1 (Mazumdar *et al*, 2010). In a differentiated colorectal cancer cell line, the opposite effect was observed, i.e. β-CATENIN enhances HIF-1α-mediated transcription, while HIF-1α inhibits the formation of the β-CATENIN transcriptional complex (Kaidi *et al*, 2007). VHL can also affect Wnt signaling independently of HIFs. As shown in normal kidney and ccRCC cell lines, the loss of VHL stabilizes β-CATENIN via the downregulation of the single-subunit E3 ubiquitin ligase JADE-1, which mediates β-CATENIN ubiquitination in addition to β-TrCP. Both β-TrCP and JADE-1 mark phosphorylated β-CATENIN for degradation in the Wnt-off state. β-TrCP cannot completely compensate for JADE-1 silencing, indicating that the ligases are partly redundant (Behrens, 2008; Chitalia *et al*, 2008). In addition, β-CATENIN can also be directly targeted for degradation by the E3 ubiquitin ligase activity of VHL in normal kidney and ccRCC cell lines. The loss of VHL enables HGF-MET-driven Wnt signaling (Peruzzi *et al*, 2006). In myogenic and neural progenitors under hypoxic conditions, HIF-1α was reported to promote Notch signaling by binding to NICD at the promoters of Notch target genes, inducing their expression (Gustafsson *et al*, 2005). A converse Notch-driven potentiation of hypoxic downstream response was noted in a myogenic cell line by NICD-mediated sequestering factor-inhibiting HIF-1 (FIH1) away from HIF-1α under normoxic conditions. Therefore, Notch signaling may allow HIF-1α downstream effects, when HIF-1α is stabilized by VHL loss in the presence of oxygen (Zheng *et al*, 2008). Another study demonstrated constitutive activation of Notch signaling in a ccRCC cell line independently of VHL disruption (Sjölund *et al*, 2008).

The upregulation of mediator molecules of Wnt and Notch signaling was associated with advanced, aggressive ccRCCs and poor patient survival (Ai *et al*, 2012; Hsu *et al*, 2012; Kruck *et al*, 2013; Lee *et al*, 2016; Lian *et al*, 2012; Ricketts *et al*, 2018; van Vlodrop *et al*, 2017; Wang *et al*, 2014b; Wu *et al*, 2011). In addition, a Wnt hyperactivation phenotype in ccRCCs from the TCGA cohort was associated with stem cell features, epithelial-to-mesenchymal transition (EMT) and hypoxic tumors, resulting in higher mortality rates (Chang & Lai, 2019). We observed that both Wnt and Notch, and stem cell signatures in the TCGA RNA sequencing data sets from ccRCC patients are correlated with decreased survival. Indeed, we found that high-Wnt and high-Notch kidney CSCs quantitatively correlate with advanced tumor stages and tumor aggressiveness and metastasis (Fendler, Myszczyszyn *et al*, 2020), similar to other solid

tumors (Saygin *et al*, 2019). However, two other analyses indicated that Notch signatures are associated with a favorable prognosis (Bhagat *et al*, 2017; Feng *et al*, 2016).

CSCs contribute to tumor resistance to standard therapies and consequently to relapse and metastasis. Therefore, targeting crucial signaling systems driving self-renewal, like Wnt and Notch, represents a promising strategy for eradicating CSCs and increasing the survival of patients. Over the past decade, small-molecule inhibitors and antibodies against various components of CSC-associated Wnt and Notch signaling in numerous solid tumors other than ccRCC have been successfully developed in preclinical models. However, the outcomes from clinical trials revealed substantial barriers in translating these investigational compounds into the clinic as single regimens or in combination with standard interventions. The major challenge is to avoid on-target toxicity in normal self-renewing tissues, which share the dependence on Wnt and Notch. The identification of cancer-specific downstream effectors of Wnt and Notch signaling will overcome this limitation. In turn, patient stratification based on the discovery of predictive biomarkers of the response to Wnt and Notch inhibition will increase treatment efficacy. Developing improved assays to examine end points for Wnt and Notch downregulation and CSC depletion in tumor samples during clinical trials might also be beneficial (Jung & Park, 2020; Meisel *et al*, 2020; Saygin *et al*, 2019; Takebe *et al*, 2015).

Inhibition of Notch signaling with small-molecule inhibitors attenuated proliferation and growth of ccRCC cell lines and xenografts (Bhagat *et al*, 2017; Sjölund *et al*, 2008). In addition, proliferation and growth of ccRCC primary cells and cell lines was inhibited by NOTCH1 and HES1 downregulation using siRNA (Liu *et al*, 2013; Sjölund *et al*, 2008). We showed that single-agent and combination treatment with small-molecule inhibitors of Wnt and Notch blocked self-renewal of CSCs in organoid and non-adherent sphere cultures established from primary human ccRCCs and impaired cell proliferation and tumor growth in subcutaneous and orthotopic patient-derived xenografts (PDXs). In line with this, ablation of β-CATENIN and NOTCH1 by siRNA attenuated growth of the sphere cultures. Thus, we confirmed the relevance of CSC-associated Wnt and Notch signaling as druggable targets in a patient-specific setting. This strategy may be translatable in the future into promising personalized therapies for ccRCC patients (Fendler, Myszczyszyn *et al*, 2020).

1.2.4. Genetic mouse models of kidney cancer

Genetically controlled mouse models enable reproducible *de novo* tumor initiation, progression and metastasis, also coupled with lineage tracing of mutated cell clones, in conditions of a defined genetic background, immunocompetence and natural tumor microenvironment, and without mechanical perturbation of cells. In addition, these models closely mimick histopathological and molecular features of human counterpart tumors. Therefore, genetic mouse systems are indispensable for preclinical oncology research, drug development and biomarker discovery and are powerful tools to study CSCs in their intact niches (Batlle & Clevers, 2017; Hou & Ji, 2018; Kersten *et al*, 2017; Nassar & Blanpain, 2016).

Histopathological data (Lindgren *et al*, 2018) and correlative transcriptomic analyses (Büttner *et al*, 2015; Chen *et al*, 2016a; Lindgren *et al*, 2017; Young *et al*, 2018) indicate that ccRCC most likely originates from proximal tubular epithelial cells. In order to establish faithful genetic mouse models for sporadic human ccRCC over the past two decades, several groups inactivated in the mouse kidney *Vhl* in isolation or in combination with deletion of other tumor suppressor genes such as *Pbrm1*, *Bap1*, *p53* and *Pten*, which are mutated in human ccRCCs (Albers *et al*, 2013; Frew *et al*, 2008; Gu *et al*, 2017; Guinot *et al*, 2016; Nargund *et al*, 2017; Pritchett *et al*, 2015; Rankin *et al*, 2006; Wang *et al*, 2014a). These attempts were unsuccessful, because the mutants displayed cystic lesions, which were associated with morbidity, and tumor precursor lesions with only few histopathological and molecular phenotypes of ccRCC. The major limitation was using non-inducible Cre under control of the promoters of genes constitutively active in nephrogenesis, including *Pax8*, *Six2*, *Ksp*, *Hoxb7* and *Pepck*.

By using inducible Cre systems that were activated in adult kidney epithelial cells, three groups succeeded to create relevant genetic mouse models, which reproduced hallmarks of sporadic human ccRCC. Genetic alterations encompassed *Vhl* inactivation in cooperation with either *Pbrm1* deletion (Espana-Agusti *et al*, 2017), with *p53* and *Rb1* knockout (Harlander *et al*, 2017) or with *Cdkn2a (p16)* loss and *Myc* overactivation (Bailey *et al*, 2017). In line with the prevalence of genetic alterations of *VHL* in human ccRCCs, these mouse models revealed the critical role of *Vhl* deficiency in ccRCC tumorigenesis, even though *Vhl* disruption alone is insufficient for transformation (Albers *et al*, 2013; Bailey *et al*, 2017; Bhagat *et al*, 2017; Espana-Agusti *et al*, 2015, 2016, 2017; Frew *et al*, 2008; Gu *et al*, 2017; Johansson *et al*, 2016; Kimura *et al*, 2008; Mathia *et al*, 2013; Nargund *et al*, 2017; Pritchett *et al*, 2015; Rankin *et al*, 2006; Schönenberger *et al*, 2016; Wang *et al*, 2014a). The models also indicated that additional genetic

alterations are required for the progression of *Vhl*-deficient kidney epithelial cells to malignant tumors. The mutants produced large, high grade solid tumors with full or nearly full penetrance. These tumors exhibited clear or eosinophilic cytoplasms, high proliferative indexes, prominent vasculatures and necrotic and haemorrhagic regions. Tumor cells shared diagnostic histopathological markers such as Ca9, Cd10 and Pax8, mTOR hyperactivation, and mutational profiles and transcriptional signatures with human ccRCCs. Combined *Vhl-Cdkn2a (p16)-Myc* mutagenesis resulted in the most aggressive ccRCCs, which expressed EMT-related genes and developed liver metastases. This is consistent with a genomic study in metastatic human ccRCCs, which revealed specific loss of *CDKN2A (P16)* associated with poor survival (Turajlic *et al*, 2018a). Tumor cells in all three models resembled histological markers and transcriptional profiles of proximal tubular cells, which provided causative evidence that the latter ones are the cells of ccRCC origin.

Inter- and intratumor heterogeneity in the three genetic mouse models implies that ccRCC can develop via different mechanisms, which mimics tumor heterogeneity in humans. Thus, the models represent different subsets of human ccRCC, which can serve in preclinical studies. For example, different mouse tumors produced by concomitant loss of *Vhl*, *p53* and *Rb1* displayed varying responses to standard treatment for metastatic human ccRCC, which mimicked the range of clinical behaviors in the human disease and can be useful for examining molecular determinants of tumor sensitivity and resistance to new therapeutic strategies.

Similar to Vhl knockout alone, the overactivation of Wnt (Clark *et al*, 2011; Cole *et al*, 2010; Qian *et al*, 2005; Saadi-Kheddouci *et al*, 2001; Sansom *et al*, 2005, 2006; Wong *et al*, 2018; Yi *et al*, 2015; Zhu *et al*, 2016) or Notch (Bielesz *et al*, 2010; Park *et al*, 2018; Zhu *et al*, 2016) signaling in mouse kidneys was insufficient for carcinogenesis. In turn, the hyperactivation of Wnt signaling together with genetic interferences at p53, p21 or K-ras did not result in the development of aggressive tumors with ccRCC characteristics (Clark *et al*, 2011; Cole *et al*, 2010; Sansom *et al*, 2005, 2006; Yi *et al*, 2015). The upregulation of Notch signaling in combination with Vhl loss contributed to formation of premalignant lesions with some ccRCC hallmarks such as clear cytoplasm with lipid accumulation (Bhagat *et al*, 2017; Johansson *et al*, 2016). The cooperative function of Wnt and Notch in ccRCC tumorigenesis, also in the context of Vhl inactivation, has not been defined so far.

2. 3D organoids to study normal and cancer stem cells in the kidney

2.1. Adult stem cell-derived organoids

Organoids from adult tissues are 3D structures grown from specific stem or progenitor cells. During organoid formation, cells self-renew, differentiate and self-organize through cell sorting and spatially restricted lineage commitment in a manner similar to the *in vivo* situation (Figure 4). Apart from architectural characteristics, organoids recapitulate functional features of their natural organs (Clevers, 2016; Lancaster & Knoblich, 2014; Schutgens & Clevers, 2020). Long-term organoid cultures can be established in hydrogels, which mimick the extracellular matrix, often Matrigel, in the absence of feeder cells, and require supplementing medium with well-defined niche growth factors, which control self-renewal, differentiation and self-organization of stem or progenitor cells (Kretzschmar & Clevers, 2016). In the last decade, organoids were generated from various human and mouse organs using distinct culture conditions and represent model systems, which are superior over 2D cell lines and non-adherent spheres and are complementary to genetic mouse models and PDXs. Organoids are emerging as powerful tools for basic and translational research applications such as studying tissue homeostasis and physiology, genetics of hereditary diseases and cancer, and infectious diseases as well as biobanking for personalized drug development, drug toxicity testing and regenerative medicine (Clevers, 2016; Lancaster & Knoblich, 2014; Li & Izpisua Belmonte, 2019; Schutgens & Clevers, 2020; Tuveson & Clevers, 2019). For their exciting potential as platforms to examine human biology and disease, organoids were awarded by *Nature* as the method of the year 2017 (Method of the Year 2017: Organoids, 2018). Despite the advances, there are still major limitations of organoids such as robustness, heterogeneity, reproducibility and direct transferability to the clinic (Aqeilan, 2021).

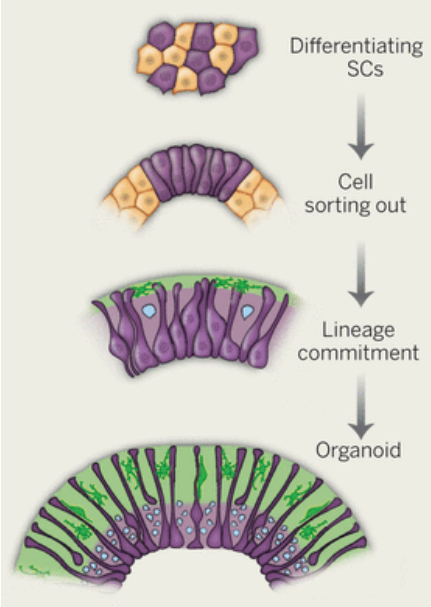

Figure 4

The development of adult stem cell (SC)-derived organoids mimicks renewal and self-organization of parental tissues (Lancaster & Knoblich, 2014).

2.2. Organoids for cancer modeling

Normal adult organoids can be used to explore the causative potential of driver mutations in cancer initiation and progression (Figure 5). For instance, two groups utilized CRISPR/Cas9 genome editing to introduce combinations of common driver mutations of colorectal cancer to human intestinal organoids to generate progression models of this tumor. Upon xenotransplantation into mice, mutant organoids grew as tumors with features of invasive colorectal cancers (Drost *et al*, 2015; Matano *et al*, 2015). Moreover, establishing organoids from adult mice with specific transgenes enabled rapid examination of the functional effects of driver mutations in the context of a defined genetic background. For example, the overexpression of the oncogenic *K-ras* transgene in mouse pancreatic organoids was sufficient to induce preinvasive pancreatic cancer after orthotopic implantation into mice (Boj *et al*, 2015). Mutant mouse prostate organoids with alterations of known oncogenes and tumor suppressor genes of prostate cancer resembled phenotypes of corresponding mouse tumors (Karthaus *et al*, 2014). Orthotopic engraftment of transformed mouse intestinal organoids into immunocompetent mice recapitulated the progression of adenomas to malignant tumors and to metastasis of colorectal cancer in the context of the functional immune system (O'Rourke *et al*, 2017). Furthermore, CRISPR/Cas9-mediated screening studies using lentiviral libraries facilitated high-throughput functional identification of new tumor

suppressor genes of colorectal cancer in premalignant human and mouse intestinal organoids (Michels *et al*, 2020; Ringel *et al*, 2020; Takeda *et al*, 2019).

Remarkably, transformed organoids can be utilized to further elucidate the biology of CSCs. Our laboratory showed that genetic knockout of the epigenetic regulator Mll1 in Wnt-high mouse colorectal cancer organoids results in depletion of Lgr5-positive CSCs, confirming that Mll1 is required for the maintenance of Wnt-dependent CSCs (Grinat *et al*, 2020). In line with this, the laboratory also demonstrated that CSC-driven organoids derived from Wnt-Bmpr mouse mutants of salivary gland cancer collapsed upon Mll1 knockout (Zhu *et al*, 2019). In addition, selective ablation of Lgr5-positive CSCs in human and mouse colorectal cancer organoids using genetic engineering revealed the plasticity of CSCs and the crucial role of these cells in the progression of primary and metastatic tumors in PDXs and allografts (de Sousa e Melo *et al*, 2017; Shimokawa *et al*, 2017). In another study, xenotransplantation of transformed human prostate organoids derived from luminal or basal stem cells resulted in tumors with different levels of aggressiveness, which identified two alternative types of cells of origin for prostate cancer (Park *et al*, 2016). As mutant organoids can be continously manipulated throughout the process of tumorigenesis, they can also be a tool to study CSC-driven intratumor clonal evolution and heterogeneity. For instance, the number of driver mutations in mouse colorectal cancer organoids governed by Lgr5-positive CSCs was proportional to the extent of chromosomal instability and organoid tumorigenicity in allografts (de Sousa e Melo *et al*, 2017). In line with this, sequential alterations of *APC* and *P53* in human intestinal organoids were sufficient to induce chromosomal instability (Drost *et al*, 2015). In addition, induction of chromosomal instability in human colorectal cancer organoids with the upregulation of *K-RAS* and *PIK3CA* promoted metastasis in PDXs (Matano *et al*, 2015).

A second strategy for cancer modeling in organoids is establishing tumor organoids directly from patient tumors (Figure 5). So-called living biobanks of tumor organoids were generated in the last years from patients with colorectal, gastroesophageal, breast, lung, pancreatic, liver, bladder, ovarian and gastric cancer (Broutier *et al*, 2017; Fujii *et al*, 2016; Hill *et al*, 2018; Kim *et al*, 2019; Lee *et al*, 2018; Nanki *et al*, 2018; Sachs *et al*, 2018; Seino *et al*, 2018; Tiriac *et al*, 2018; Vlachogiannis *et al*, 2018; van de Wetering *et al*, 2015). These organoid biobanks represent histological, genomic and transcriptomic heterogeneity of parental primary and metastatic tumors. Drug responses obtained in organoid biobanks are well translatable to individual patients, confirming that organoids will be applicable in preclinical development of personalized therapies. Organoid

biobanks can advance large-scale screenings of new drug candidates. These biobanks can also enable the identification of new genes with prognostic value and the discovery of predictive biomarkers of drug sensitivity and resistance to stratify individual patients to specific treatment. For example, colorectal cancer organoids harboring a specific mutation in the negative Wnt feedback regulator *RNF43* were sensitive to PORCN inhibitors, which inhibit the secretion of Wnt ligands (van de Wetering *et al*, 2015).

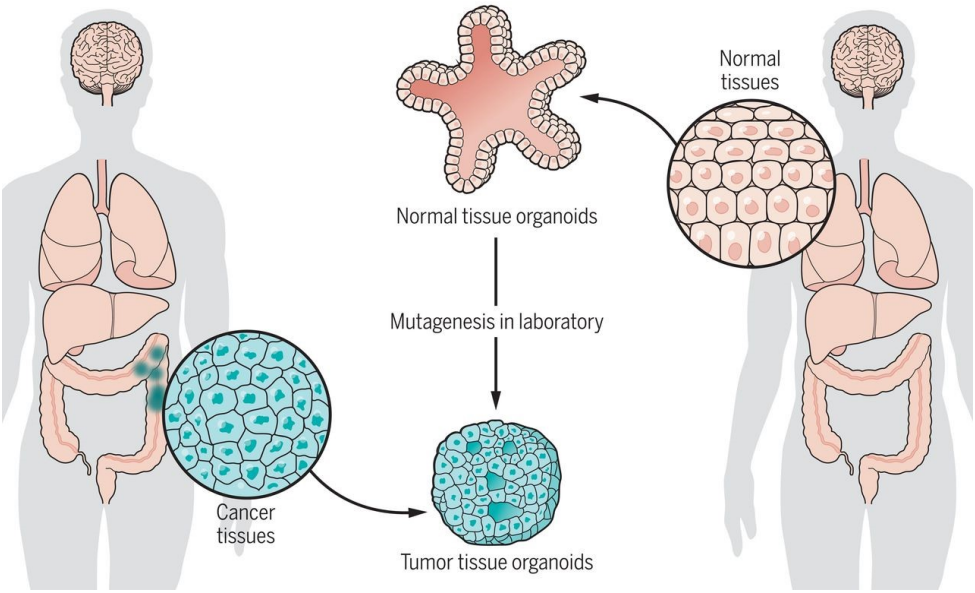

Figure 5

Cancer modeling in organoids. Tumor organoids can be established either through mutagenesis of normal organoids using genetic engineering or directly from patient tumors (Tuveson & Clevers, 2019).

2.3. Normal and kidney cancer organoids

Kidney organoids and tubuloids were created from human induced pluripotent stem cells (iPSCs) (Morizane & Bonventre, 2017a; Morizane *et al*, 2015; Takasato *et al*, 2015, 2016), and more recently from healthy human and mouse kidneys (Grassi *et al*, 2019; Rinkevich *et al*, 2014; Schutgens *et al*, 2019) as well as from human kidney cancers (Bolck *et al*, 2021; Calandrini *et al*, 2020; Grassi *et al*, 2019; di Martino *et al*, 2018; Schutgens *et al*, 2019) and from human urine (Schutgens *et al*, 2019). Organoid cultures are valuable additions in basic and translational kidney research (Morizane & Bonventre, 2017b; Rookmaaker *et al*, 2015; Wang *et al*, 2017; Woolf, 2019; Yousef Yengej *et al*, 2020). We showed earlier that organoids established from primary human ccRCCs originate from and are maintained by CSCs, which display the activation of stem cell-associated Wnt and Notch signaling. In these organoids, we were able to test responses to inhibition of Wnt and Notch in a patient-tailored setting (Fendler, Myszczyszyn *et al*,

2020). Thus, ccRCC-derived organoids will advance the development of personalized therapies, similiarly to organoids derived from other tumors. Moreover, kidney organoid cultures generated from healthy adults, pediatric Wilms' tumors and urine from patients with cystic fibrosis enabled to model BK virus infection and to examine drug responses of Wilms' tumor and cystic fibrosis cells (Calandrini *et al*, 2020; Schutgens *et al*, 2019). In a very recent follow-up study, Clevers and collaborators integrated their human tubuloids into a perfused microfluidic kidney-on-a-chip system (Gijzen *et al*, 2021). Knockout of the *PKD1* and *PKD2* genes in human iPSC-derived renal organoids mimicked the development of polycystic kidney disease (Freedman *et al*, 2015). Kidney organoids established from human ESCs were used to investigate infection with the SARS-CoV-2 coronavirus and blocking viral entry by recombinant soluble ACE2 (Monteil *et al*, 2020). So far, adult mouse kidney organoids have not been characterized to my satisfaction and their usefulness has not been shown.

Aims of my study

Organoids are emerging as essential tools for kidney research. Adult mouse kidney organoids have not been well characterized and their usefulness has not been shown. These organoids may help to understand tubular renewal and repair by assisting in the identification of stem or progenitor cells. In addition to genetic mouse models of ccRCC, mouse organoids may be valuable to study tumorigenesis in the kidney in a defined genetic background by simultaneous or sequential mutagenesis at multiple loci of putative driver genes. Similar to our patient-derived ccRCC organoids, cancer organoids from mice may be utilized to identify further driver-specific druggable targets and to examine drug-induced nephrotoxicity in matched healthy, non-transformed cells. Hence, the first part of my dissertation focused on the generation as well as structural and functional examination of a long-term 3D organoid (tubuloid) model of the adult mouse kidney as the platform for translational studies on normal stem cells and CSCs in the kidney.

Numerous efforts were made in the last 20 years to create genetic mouse models, which truly reflect cellular and molecular features of human ccRCC. However, few such disease-relevant systems exist so far. Wnt and Notch signaling are elevated in $CXCR4^{+}MET^{+}CD44^{+}$ CSCs from primary human ccRCCs and maintain self-renewal and tumorigenicity of these CSCs in relevant patient-derived systems. Answers to fundamental questions remain elusive on whether and how the functional interplay of Wnt and Notch with or without Vhl inactivation drives tumorigenesis in the kidney. To mimick the development of Wnt-high and Notch-high human ccRCC, the second aim of my dissertation was to establish and characterize inducible genetic mouse models with the overactivation of Wnt and Notch in adult kidney epithelial cells, also in the context of Vhl deficiency. These models could be used to identify new druggable oncogenic downstream effectors of Wnt and Notch. Adding to our results on inhibiting Wnt and Notch in patient-derived CSC-governed xenografts, organoids and non-adherent spheres, the models could thus serve for further preclinical validation of both signaling systems as targets for anti-CSC therapy for ccRCC, also in combination with standard treatment based on blocking VHL loss-driven angiogenesis.

Results

1. A long-term 3D tubuloid model of the adult mouse kidney

1.1. Growth of long-term 3D kidney tubuloid cultures

I isolated single epithelial cells from whole mouse kidneys and established 3D tubuloid cultures (n = 20) with high efficiency in Matrigel under defined, serum-free conditions. The protocol was adapted to specific needs of kidney epithelial cells (Table 1). Within 14 days of culture, single cells grew continuously and formed tubuloids with sizes up to 1.5 mm in diameter (Figure 6A). By haematoxylin-eosin (H&E) staining, I classified three tubuloid types: cystic tubuloids with one or more cell layers and a single big lumen (with few tubuloids containing one or two additional smaller lumina), solid filled tubuloids and alveolar tubuloids with multiple lumina, accounting for 65%, 25% and 10% (Figure 6B).

The efficiency of tubuloid formation was 5 times higher from single cells in the first passage in comparison to freshly seeded cultures (Figure 6C and D), indicating the self-renewal capacity of tubuloid-forming cells. For maintenance, the tubuloids were serially passaged starting from small cell clusters (Figure 6E), which allowed me to culture them for at least 3.5 months (passage 12) (Figure 7A). I expect that tubuloid culturing is possible for longer. For subsequent experiments, tubuloid cultures were established from mice with a mixed background, but they could also be generated from C57BL/6J mice with similar efficiencies (Figure 7B). Hence, I created long-term tubuloids from single adult mouse kidney epithelial cells, which predominantly exhibited cystic morphologies, consistent with organoid cultures derived from other adult organs (Schutgens & Clevers, 2020).

1.2. Kidney tubuloids resemble the adult mouse kidney epithelia, are stable over time and display enhanced proliferative capacity

In order to study whether the tubuloids represent the adult mouse kidney epithelia, we performed mass spectrometry-based high-throughput and high-resolution bulk proteomics and phosphoproteomics. We compared three independent biological replicates of adult kidney epithelial cells (control), early passage tubuloids (passage 2, 1-month culture) and long-term passage tubuloids (passage 12, 3.5-month culture). To prepare control samples, Epcam-positive kidney epithelial cells were MAC-sorted from freshly isolated single cell suspensions from whole mouse kidneys to ensure optimal normalization, similar to a protocol for single cell RNA sequencing of adult human kidney tubuloids (Schutgens *et al*, 2019). In all samples, we were able to detect around 9.000 proteins, which is so far the maximal coverage of the coding genome (Mertins *et al*,

2018), and around 16.000 corresponding phosphorylation sites. Based on the expression and phosphorylation levels of the proteins, we calculated Pearson correlations between all samples. We found high correlations, at least 0.8, between adult kidney epithelial cells (CK) and both early passage tubuloids (TEP) and long-term passage tubuloids (TLP) for both the proteome (Figure 8A) and phosphoproteome (Figure 8B), indicating that the tubuloids greatly resembled the kidney epithelia. In addition, long-term passage tubuloids recapitulated early passage tubuloids for both the proteome (Figure 8A) and phosphoproteome (Figure 8B), as shown by correlations of around 1, confirming that tubuloid cultures were stable over time.

I also examined the importance of differentially expressed proteins between the tubuloids and kidney epithelia. Using a bioinformatic tool for functional annotation clustering, DAVID, I discovered 10 biological processes, which were governed by the most upregulated proteins in the tubuloids in comparison to the kidney epithelia (Figure 8C). The top three enriched processes were cell cycle and ribosomal activity and DNA replication, which indicate the presence of proliferating cells. I confirmed this by BrdU incorporation in the nuclei (marked in magenta) (Figure 8D). In line with self-renewal, enhanced proliferative capacity suggests the enrichment in stem or progenitor cells in the tubuloids (Grassi *et al*, 2019; Kang *et al*, 2016; Schutgens *et al*, 2019; Uchimura *et al*, 2020), and thus the recapitulation of the potential for adult tissue turnover and repair, consistent with tubuloid cultures derived from other organs (Schutgens & Clevers, 2020). The DAVID analysis also revealed the enrichment in proteins of cell-cell adherens junctions and basement membranes, which characterize epithelial cell polarity. Thus, the tubuloids and adult mouse kidney epithelia greatly share the proteome and phosphoproteome, which remain unchanged over passages. Moreover, strong self-renewal and proliferative capacities of the tubuloids are the signs for the enrichment in stem or progenitor cells.

1.3. Kidney tubuloids contain differentiated, polarized and functional tubular epithelial cells

I examined the proteomics results by manual curation and characterized the tubuloids by immunofluorescence and real-time qPCR. Ubiquitous staining of Pax8 in the nuclei (marked in brown) confirmed that tubuloid cells were of kidney origin (Schutgens *et al*, 2019) (Figure 9A). The tubuloids contained differentiated kidney epithelial cells, as indicated by the presence of adherens junctions between the lateral membranes of neighboring cells, which were positive for E-cadherin (E-cad, marked in orange) (Figure 9B), as well as by the upregulation of Keratin 8 (Krt8), Claudin 4 (Cldn4) and Keratin 18

(Krt18) (Grassi *et al*, 2019; Liao *et al*, 2020; Takasato *et al*, 2015; Yu, 2015) (Figure 9C). In line with the results of the DAVID analysis, the cells displayed pronounced epithelial polarity, as shown by the location of Laminin in the basal laminae (marked in green) and of ZO-1-positive tight junctions at the apical sides (marked in red) (Figure 9D).

The cells were positive either for Lotus Tetragonolobus Lectin (LTL, marked in red), a marker of proximal tubular epithelial cells, or Peanut Agglutinin (PNA, marked in green), a marker of epithelial cells of the distal nephrons, i.e. distal tubules and collecting ducts (Kang *et al*, 2016; Rinkevich *et al*, 2014; Schumacher, 2003; Takasato *et al*, 2015), and both markers were usually detected within the same tubuloids (Figure 9E). The proteomic analysis revealed the enrichment in 48 membrane transporters in both early (TEP) and long-term (TLP) passage tubuloids (Figure 9F), including known transporters of proximal tubular cells such as the amino acid transporters Slc1a4 and Slc1a5 (Kanai *et al*, 2013), the glucose transporter Slc2a1 (Schutgens *et al*, 2019), the myo-inositol transporter Slc5a11 (Lahjouji *et al*, 2007), the ion transporters Slc12a6 (Mercado *et al*, 2005) and Slc26a2 (Chapman & Karniski, 2010), the zinc transporters Slc30a6 (Brunskill *et al*, 2014) and Slc39a10 (Kaler & Prasad, 2007) and the efflux transporters Abcb1b (Mdr1/P-gp), Abcc3 (Mrp3) and Abcc4 (Mrp4) (Masereeuw & Russel, 2012). In addition, known transporters of the distal nephrons were upregulated, including the glycine transporter of distal and connecting tubules, Slc6a9 (Stow & Gumz, 2011), and the ion transporters of collecting ducts, Slc4a1ap (Chen *et al*, 1998), Slc4a7 (Praetorius *et al*, 2004), Atp6ap2 (Trepiccione *et al*, 2016) and Trpv4 (Mamenko *et al*, 2017). The proton transporters Atp6v0a1 and Atp6v0a2, which are present in both proximal tubules and collecting ducts (Schulz *et al*, 2007), were also enriched. Apart from the overexpression of the transporters, the proteomic analysis of the tubuloids revealed the upregulation of the common cytoplasmic marker (a kinase) of distal and connecting tubules and of cortical collecting ducts, Wnk1 (Hoorn *et al*, 2011), and the nuclear marker (a transcription factor) of collecting ducts, Gata3 (Schutgens *et al*, 2019) (Figure 9G). In LTL/PNA-double-positive tubuloids, I confirmed at the apical side of a subset of LTL-positive cells the expression of Abcb1b (marked in cyan), another marker of proximal tubular cells, which did not overlap with PNA-positive cells of the distal nephrons (Figure 9H). In these tubuloids, I also detected on a subset of PNA-positive cells the expression of Aquaporin 3 (Aqp3, marked in magenta), a marker of principal cells of collecting ducts (Schutgens *et al*, 2019), which was mutually exclusive with LTL-positive cells (Figure 9I). I also observed the mutually exclusive expression of LTL and PNA in solid and alveolar tubuloids (Figure 10A). Whole mount confocal fluorescence microscopy confirmed the

expression patterns of LTL, PNA and E-cad in a 3D reconstructed cystic (Figure 10B and C) and solid (Figure 10D and E) tubuloid.

Even though tubuloid cells were isolated from whole kidneys, I did not find the expression of the markers of podocytes, Nephrin (Nphs1), Podocalyxin (Podxl) and Podocin (Nphs2) (Schutgens *et al*, 2019) (Figure 11A), the markers of parietal glomerular epithelial cells, Cldn1 and Vcam1 (Liao *et al*, 2020; Yu, 2015) (Figure 11B), and the markers of the Loop of Henle, Slc14a2, Uromodulin (Umod) and Slc12a1 (Lee *et al*, 2015; Schutgens *et al*, 2019) (Figure 11C). The markers of stromal cells, Cald1, Pdgfrb and Meis1 (Schutgens *et al*, 2019) (Figure 11D), and the markers of endothelial cells, Pecam1, Cdh5 and Flt1 (Schutgens *et al*, 2019) (Figure 11E), were also not present.

I rarely observed tubuloids, which were positive for only LTL or PNA (Figure 12A), indicating that the majority of the tubuloids grew from cells with differentiation potential into at least two lineages, i.e. multi-lineage differentiation. To test for the differentiation capacity of tubuloid-forming cells, I FAC-sorted single viable (SYTOX Orange-negative) cells (Figure 12B), seeded 500 sorted cells per well in Matrigel and tracked tubuloid growth for 11 days (Figure 12C). 87% of clonally grown tubuloids were double-positive for LTL and PNA, while tubuloids positive for only one marker were rare (Figure 12D). In the multi-lineage tubuloids, some LTL-positive proximal tubular cells at the apical side expressed Abcb1b (Figure 12E) and some PNA-positive cells of the distal nephrons expressed collecting duct-specific Aqp3 (Figure 12F).

Transmission electron microscopy confirmed epithelial cell polarity and complexity of the tubuloids. Cystic tubuloids developed microvilli (MV) at the apical membranes towards the lumen (L), a typical feature of proximal tubular cells (Figure 13A). At the basal side, microvilli-free basal laminae (arrowhead) and filopodia (F) were seen (Figure 13A). Junctional complexes (JC) between neighboring cells, which are involved in barrier formation, were present at the lateral membranes at the luminal side. JC included from the apical to basal side: tight junctions (zonula occludens, black asterisk), adherens junctions (belt desmosomes, zonula adhaerens, white asterisk), spot desmosomes (macula adhaerens, red asterisks) and closely aligned or nearly fused lateral membranes (white and black arrowheads, respectively) (Figure 13B). At the basal side, we observed spot desmosomes (red asterisk) and closely aligned or nearly fused lateral membranes (white and black arrowheads, respectively) (Figure 13C).

Endocytic events, i.e. clathrin-coated pits with diameters of around 100 nm, were observed at the apical and lateral membranes (marked by the arrowheads) (Figure 13D). Endocytosis is a crucial feature of proximal tubular cells, which is required to reabsorb proteins and other substances from glomerular filtrates (Nielsen *et al*, 2016). Functional endocytosis was detected in 32% of the tubuloids by uptake of Alexa488-conjugated dextran (marked in green) (Figure 13E).

Another functional assay for proximal tubular cells in kidney tubuloids is testing the response to cisplatin, a known nephrotoxic agent, which induces caspase-3-mediated apoptosis (Grassi *et al*, 2019; Takasato *et al*, 2015). Cisplatin treatment produced concentration-dependent inhibition of tubuloid growth (Figure 13F) and decreased cell viability (Figure 13G). I observed apoptosis induction in tubuloid cells by Cleaved Caspase-3 activation after 72 hrs at a 100 µM dose (Figure 13H). However, H&E staining of the tubuloids did not show changes in their morphologies upon treatment with cisplatin at the IC50 concentration (Figure 13I). Altogether, kidney tubuloids contain differentiated tubular epithelial cells with apical and basal polarity and complex intercellular junctions. I documented multi-lineage differentiation into proximal tubular cells and cells of the distal nephrons. The tubuloids display functional features of proximal tubular cells, including endocytosis and sensitivity to cisplatin.

1.4. Signaling systems, which control self-renewal, growth and differentiation of kidney tubuloids

Organoids require specific growth factor cocktails, which mimick their physiological microenvironment in the organ of origin (Sato & Clevers, 2015). To culture my tubuloids, I started with a basal serum-free medium containing DMEM/F12 with Glutamax, HEPES buffer, N-acetylcysteine, the growth supplements B27 and N2, nicotinamide, EGF, the TGFβ inhibitor A83-01 and the Wnt activator R-spondin-1 (Rinkevich *et al*, 2014; Sato *et al*, 2011) (Table 1). This resulted in low numbers of tubuloids per well (Figure 14A). To improve the efficiency, I combined the basal medium with additional growth factors, hydrocortisone (HC) (Huang *et al*, 2015), prostaglandin E2 (PGE2) (Drost *et al*, 2016) and fibroblast growth factor 10 (FGF10) (Sato & Clevers, 2015). HC and PGE2 have not been used before to establish kidney organoids. The combination of the basal medium with HC and PGE2 resulted in the highest average numbers of tubuloids per well (average 40, efficiency 0.04%), which was a read-out for the strongest self-renewal capacity of tubuloid-forming cells (Snippert *et al*, 2010) (Figure 14A). This combination also maintained the large tubuloid sizes, which I observed with the basal medium only (Figure 14B). Therefore, the mixture of the basal medium with HC and PGE2 was

chosen as culture medium for further experiments to characterize the tubuloids. The addition of Y-27632 dihydrochloride (Rho kinase/ROCK inhibitor) to prevent anoikis (Grassi *et al*, 2019; Schutgens *et al*, 2019) did not improve culture efficiency (Figure 15A and B).

The chosen culture conditions suggest the dependence of my tubuloids on the EGF receptor and Wnt signaling and the inhibition of TGFβ signaling. I confirmed this dependence by removing or adding single growth factors and by blocking these signaling systems with small-molecule inhibitors. EGF is a crucial component for most adult organoids (Sato & Clevers, 2015), indicating that the mitogenic activation of the EGF receptor signaling is indispensable for mouse kidney tubuloid cultures. In line with this, EGF removal strongly reduced tubuloid numbers, i.e. self-renewal, and sizes (Figure 15A and B). Withdrawal of the TGFβ inhibitor A83-01 also impaired tubuloid numbers, i.e. self-renewal, and sizes, and this effect was enhanced by the addition of TGFβ, which blocked tubuloid formation (Figure 15A and B). Treatments with the EGF receptor inhibitor gefitinib, the Mek inhibitor U0126 and the Pi3k inhibitor BYL719 (Figure 15C) resulted in concentration-dependent inhibition of tubuloid growth (Figure 15D/F/H) and decreased cell viability (Figure 15E/G/I). H&E staining did not reveal significant changes in the predominant cystic morphologies of the tubuloids upon removal of EGF or A83-01 or treatment with gefitinib at the IC50 concentration (Figure 15J).

The proteomic analysis revealed in both early (TEP) and long-term (TLP) passage tubuloids the upregulation of components of Wnt signaling, including the ligands Wnt4, Wnt7b and Wnt10a, the co-receptors Lrp5 and Lrp6, the destruction complex disassembly-mediating protein Dvl2 and the targets Axin2, Birc5, Cd44 and Cyclin D1 (Ccnd1) (Figure 16A). Withdrawal of the Wnt activator R-spondin-1 reduced tubuloid numbers, i.e. self-renewal, and sizes. The addition of the Wnt ligand Wnt3a (Sato *et al*, 2011) did not improve tubuloid yield (Figure 16B and C), possibly due to autocrine supply of Wnt4, Wnt7b or Wnt10a. Treatments with ICG-001, an inhibitor that blocks β-catenin-Tcf-mediated transcription, and with another β-catenin-Tcf inhibitor, LF3, developed in our laboratory (Fang *et al*, 2016) (Figure 16D), produced concentration-dependent inhibition of tubuloid growth (Figure 16E and G) and decreased cell viability (Figure 16F and H). By H&E staining, I observed upon R-spondin-1 removal a switch from predominant cystic to fully solid tubuloids, while treatment with ICG-001 at the IC50 concentration did not result in significant morphological changes (Figure 16I). The transition to the solid morphologies induced by R-spondin-1 withdrawal prompted me to study the importance of Wnt signaling for the control of tubuloid differentiation. By real-

time qPCR, I examined in the tubuloids upon R-spondin-1 removal or ICG-001 treatment the expression of selected genes, which are induced in differentiated kidney cells. I found increases in the abundance of Krt8, Krt18 and Cldn4 (Figure 16J). I also observed the upregulation of the proximal tubule genes Abcb1b, Slc3a1 and Slc40a1 (Figure 16K) as well as of the distal nephron genes Aqp3, Atp6ap2 and Wnk1 (Figure 16L). Immunofluorescence staining confirmed the upregulation of Aqp3 in these tubuloids on protein level (Figure 16M).

Besides Wnt, the proteomic analysis also revealed in both early (TEP) and long-term (TLP) passage tubuloids the upregulation of two other stem cell-associated signaling systems, Notch (Figure 17A) and Yap (Figure 17B), which are involved in kidney repair. Upregulated Notch components included the ligand Jag2, the receptors Notch1, Notch2 and Notch3, the S2 cleavage-mediating metalloproteinase Adam17, the S3 cleavage γ-secretase complex-related Aph1a and Ncstn as well as the coactivators Rbpj, Maml1, Maml2 and Kat2b. Upregulated Yap components were direct Yap targets. Similar to other organs, where Yap signaling is important for driving stem cell behavior and regeneration in response to mechanical stimuli (Panciera *et al*, 2017), deletion of Yap in the mouse kidney impairs tissue recovery upon injury (Chen *et al*, 2018). Yap is also instrumental for the coordination of self-renewal, differentiation and self-organization of distinct organoid cultures (Panciera *et al*, 2017). The significance of Notch and Yap signaling for the control of self-renewal, growth and differentiation of mouse kidney tubuloids requires further research, but this goes beyond the scope of my dissertation. Altogether, my mouse kidney tubuloid cultures require a specific growth factor cocktail, which promotes their self-renewal and growth through the activation of the EGF receptor and Wnt signaling and the inhibition of TGFβ signaling. Moreover, Wnt signaling controls tubuloid differentiation into proximal and distal nephron lineages. I presented my results on the tubuloids at the *Cell* Symposium Engineering Organoids and Organs in San Diego (Myszczyszyn *et al*, 2019a) and at The Notch Meeting XI in Athens (Myszczyszyn *et al*, 2019b).

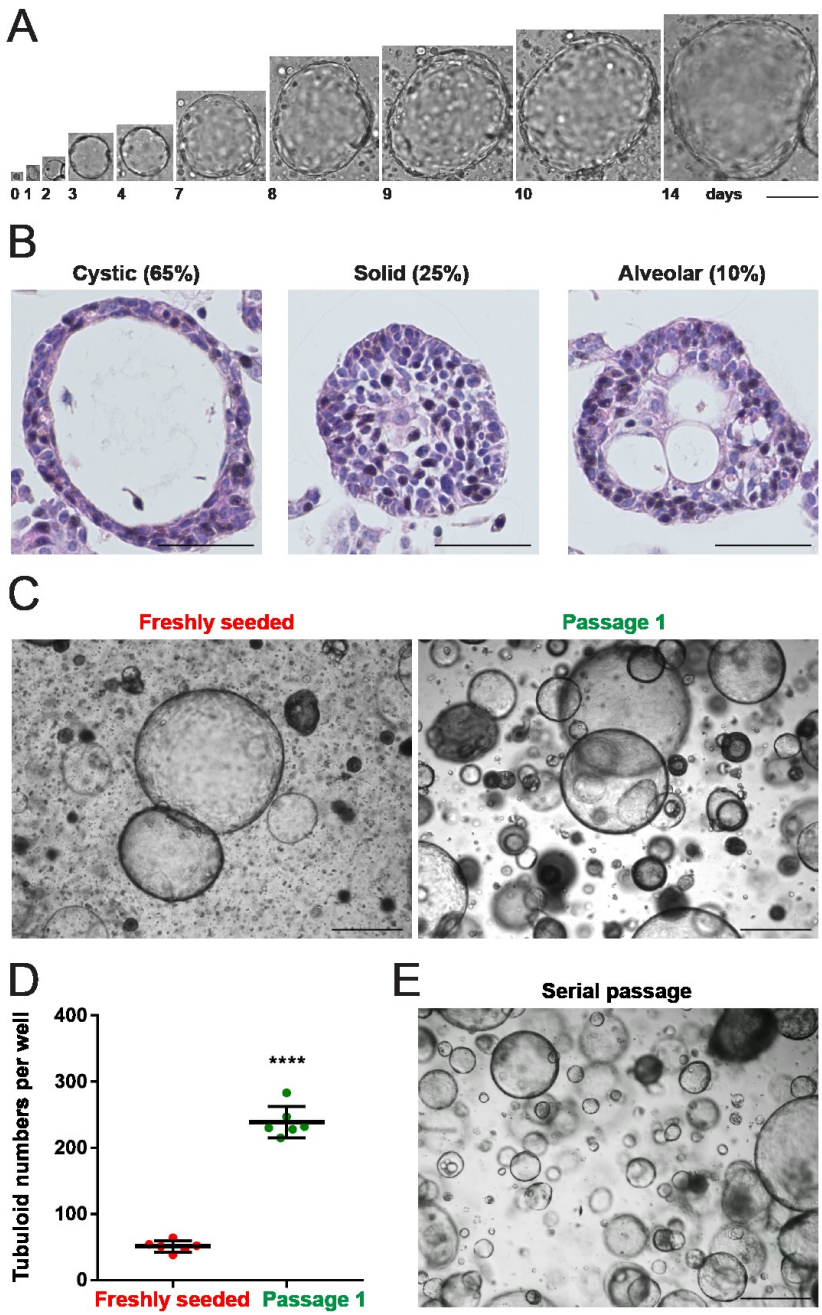

Figure 6

Growth of long-term 3D tubuloid cultures from adult mouse kidneys. (A) Brightfield images acquired on consecutive days of a representative tubuloid formed from a single freshly seeded cell. (B) Representative H&E staining showing freshly seeded tubuloids with cystic (left), solid (middle) and alveolar (right) morphology. (C) Representative brightfield images of a freshly seeded (left) and then once passaged (right) tubuloid culture grown from 10^5 single cells. (D) Quantification of tubuloid numbers in a freshly seeded and passage 1 culture. (E) A representative brightfield image of a serially passaged tubuloid culture after 5 passages. Data information: scale bars, 100 µm in A, 50 µm in B, 500 µm in C and E. 20 freshly seeded tubuloid cultures were established in total. In A, one independent biological replicate was examined. For quantification in B, 180 tubuloids were counted in total. One independent biological replicate was examined. For quantification in C and D, 10^5 cells were seeded and the tubuloids with diameters ≥ 100 µm were counted after 14 (freshly seeded cells) or 7 (passaged cells) days of culturing (6 wells, technical replicates).

One independent biological replicate was examined. In D, the graph depicts means ± SD (error bars). Data passed the Shapiro-Wilk normality test (α = 0.05). The unpaired, two-tailed Student's t-test was performed; P-value, < 0.0001, ****p < 0.0001. In E, 3 independent biological replicates were examined.

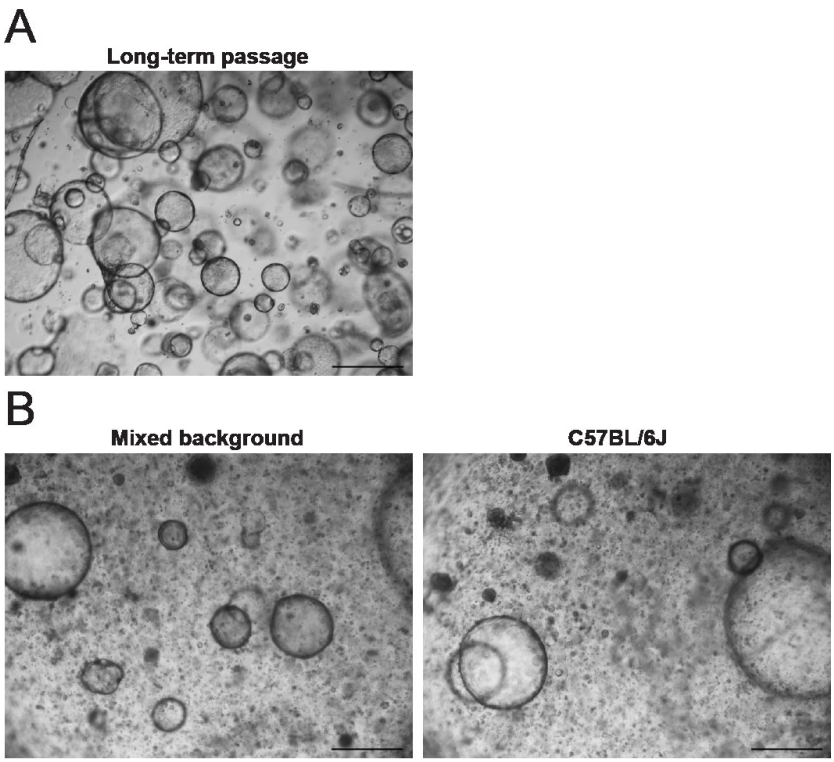

Figure 7

Long-term culture of the tubuloids and establishing the tubuloids from different mouse backgrounds. (A) A representative brightfield image of a tubuloid culture, which was serially passaged for 3.5 months. (B) A representative brightfield image of a freshly seeded tubuloid culture from mixed background (left) and B57BL/6J background (right) mice. Data information: scale bars, 500 μm. 3 independent biological replicates were examined.

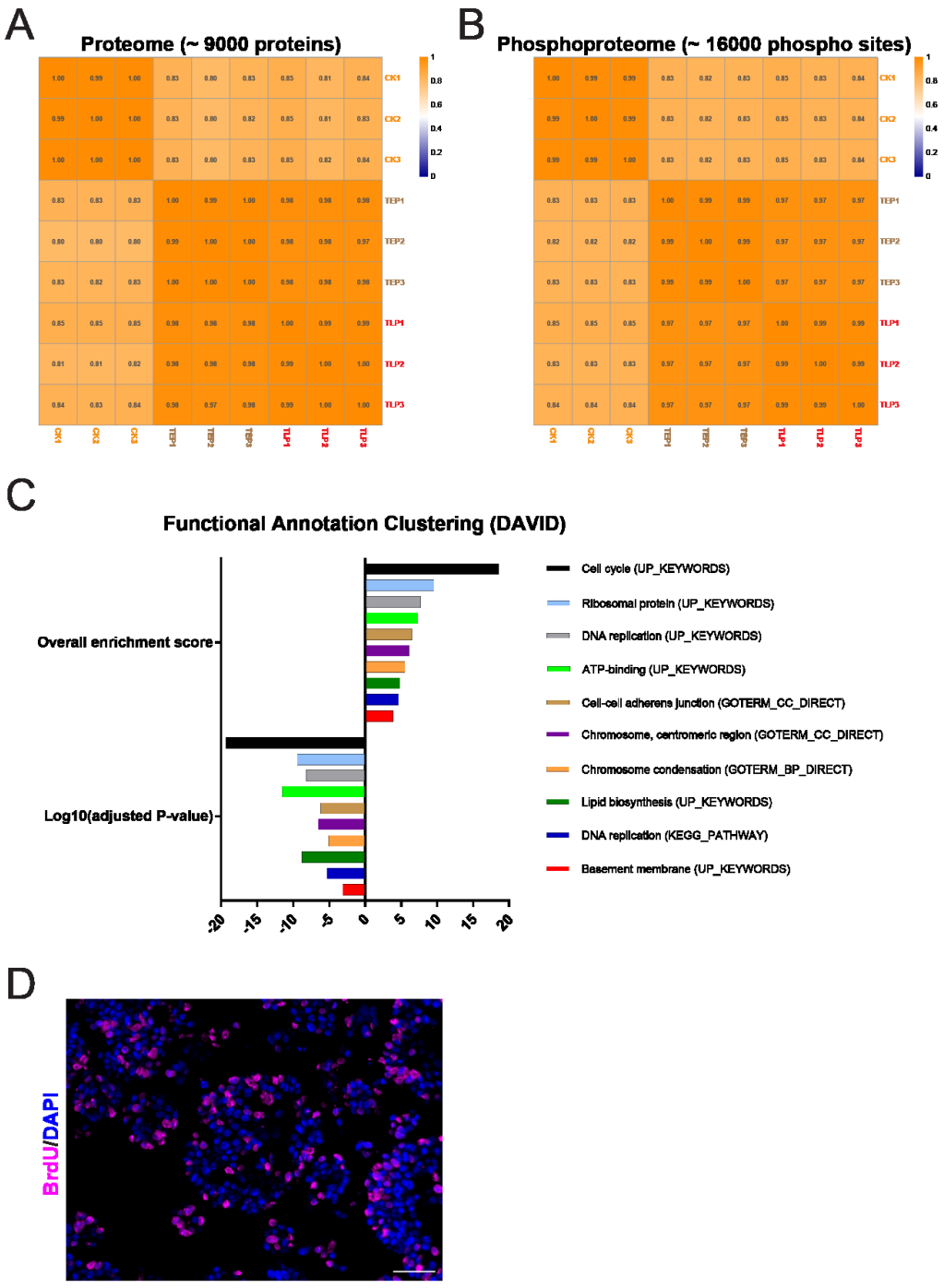

Figure 8

The tubuloids resemble the adult mouse kidney epithelia, are stable over time and display enhanced proliferative capacity. (A) A heatmap for the Pearson correlation matrix (coefficient) of the expression levels of overall ~ 9.000 detected proteins between all samples of the mouse kidney epithelia (CK), early passage tubuloids (TEP) and long-term passage tubuloids (TLP). All experimental columns were correlated against each other. (B) A heatmap for the Pearson correlation matrix (coefficient) of the phosphorylation levels of overall ~ 16.000 detected corresponding phosphorylation sites between all samples of the mouse kidney epithelia (CK), early passage tubuloids (TEP) and long-term passage tubuloids (TLP). All experimental columns were correlated against each other. (C) A functional annotation clustering of the most upregulated proteins in the tubuloids using the DAVID bioinformatic tool. Shown are 10 most enriched

clusters, based on the overall enrichment scores, with their representative terms (biological processes), based on the adjusted P-values. (D) Representative 2D immunofluorescence for BrdU (magenta) of a tubuloid culture. Data information: scale bars in D, 50 μm. Nuclei are counterstained with DAPI. 3 independent biological replicates were examined.

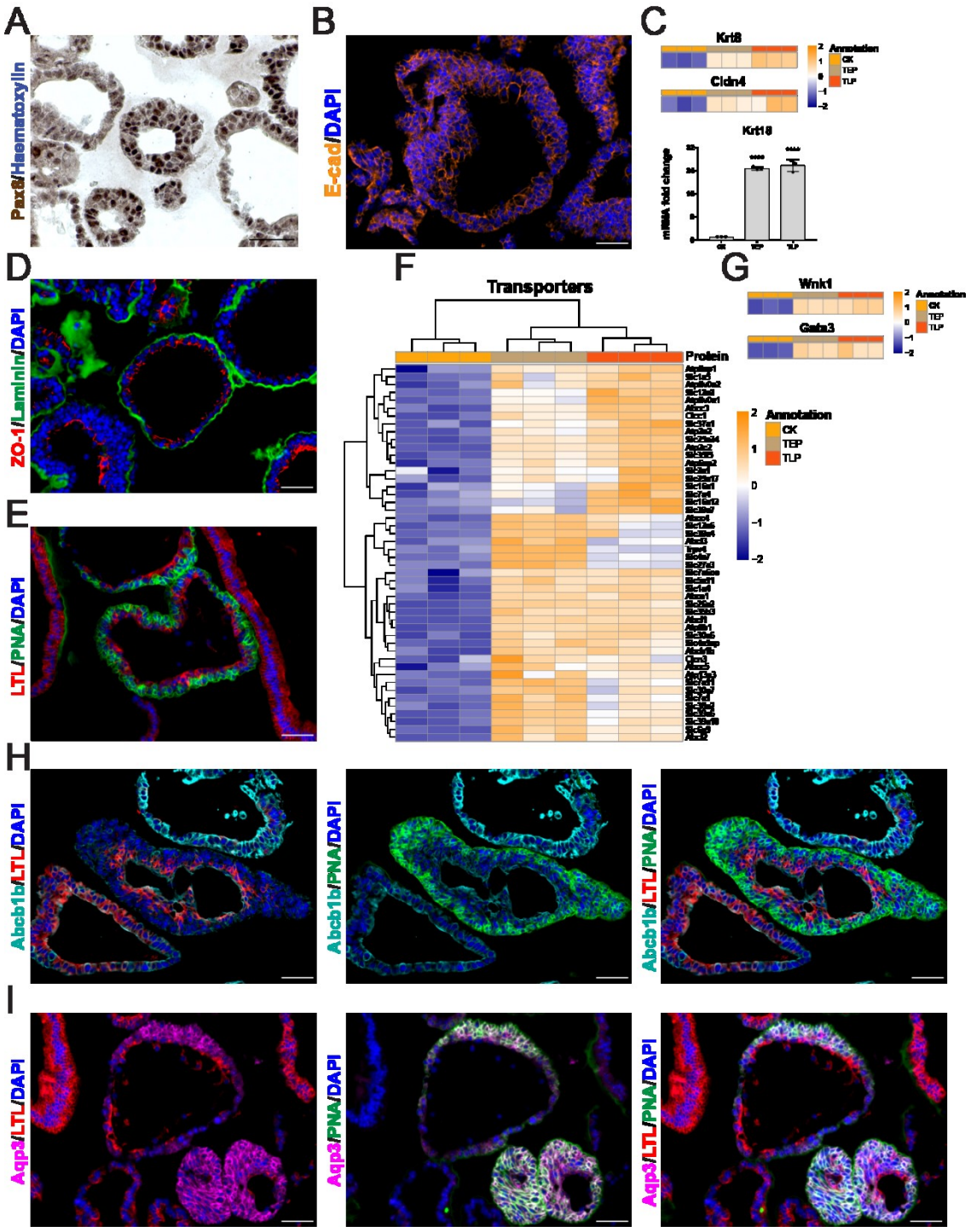

Figure 9

The tubuloids exhibit markers of differentiated and polarized tubular epithelial cells. (A) Representative immunohistochemistry for Pax8 (brown) of a tubuloid culture. (B) Representative 2D immunofluorescence for E-cad (orange) of a tubuloid culture. (C) Proteomic heatmaps for Krt8 and Cldn4 in both early (TEP) and long-term (TLP) passage tubuloids in comparison to the mouse kidney epithelia (CK) (upper part), and a real-time qPCR analysis of gene expression of Krt18 in both early (TEP) and long-term (TLP) passage tubuloids in comparison to whole mouse kidney cells (CK) (lower part). (D) Representative 2D immunofluorescence for Laminin (green) and ZO-1 (red) of a tubuloid culture. (E) Representative 2D immunofluorescence for LTL (red) and PNA (green) of a tubuloid culture. (F) A proteomic heatmap for 48

membrane transporters in both early (TEP) and long-term (TLP) passage tubuloids in comparison to the mouse kidney epithelia (CK). (G) Proteomic heatmaps for Wnk1 and Gata3 in both early (TEP) and long-term (TLP) passage tubuloids in comparison to the mouse kidney epithelia (CK). (H) Representative 2D immunofluorescence for Abcb1b (cyan), LTL (red) and PNA (green) of a tubuloid culture. (I) Representative 2D immunofluorescence for Aqp3 (magenta), LTL (red) and PNA (green) of a tubuloid culture. Data information: scale bars in A/B/D/E/H/I, 50 µm. In A, nuclei are counterstained with haematoxylin; in B/D/E/H/I, nuclei are counterstained with DAPI. In C, the graph depicts means ± SD (error bars). The ordinary one-way ANOVA followed by the Dunnett's multiple comparison to CK were performed; both P-values, 0.0001, ****p < 0.0001. In C/F/G, the heatmaps show normalized log2 intensity values for 3 independent biological replicates of CK, TEP and TLP. A 5% FDR (adjusted P-value < 0.05) cutoff and a log2 fold change cutoff of > 0 were applied for both TEP over CK and TLP over CK. The values were scaled (z-score by row) with breaks from ≤ -2 to ≥ 2. In A/B/D/E/H/I, 3 independent biological replicates were examined. For the real-time qPCR analysis of Krt18 in C, 3 independent biological replicates in technical triplicates were examined.

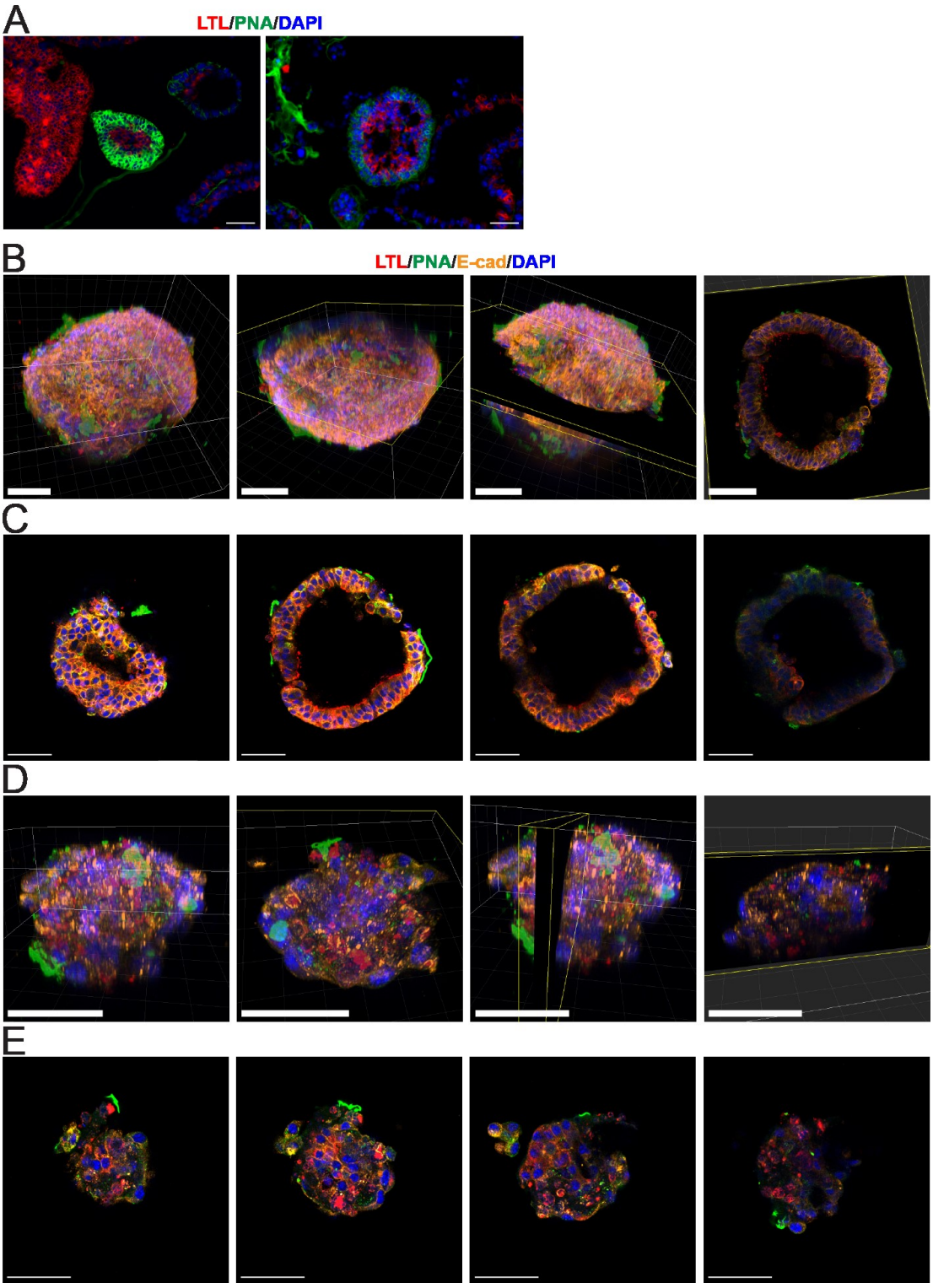

Figure 10

Markers of tubular epithelial cells are exhibited in 3D reconstructed tubuloids. (A) Representative 2D immunofluorescence of a solid (left) and an alveolar (right) tubuloid positive for both LTL (red) and PNA (green). (B-E) Whole mount 3D confocal microscopy of a representative cystic (B and C) and solid (D and E) tubuloid positive for LTL (red), PNA (green) and E-cad (orange). (B and D) 3D reconstructions of all z-stacks from a cystic (B) and solid (D) tubuloid. From the left to the right: a 3D reconstructed tubuloid seen from the top-side (coordinates given for orientation), a top-side view opened by a clipping plane, a top-side view with

a marked orthogonal slice (8 µm) and an extended orthogonal slice (8 µm) only. (C and E) Selected 2D images of z-stacks at different depths (top, middle, bottom) of a cystic (C) and solid (E) tubuloid. Data information: scale bars, 50 µm. Nuclei are counterstained with DAPI. In A, 3 independent biological replicates were examined; in B-E, one independent biological replicate was examined.

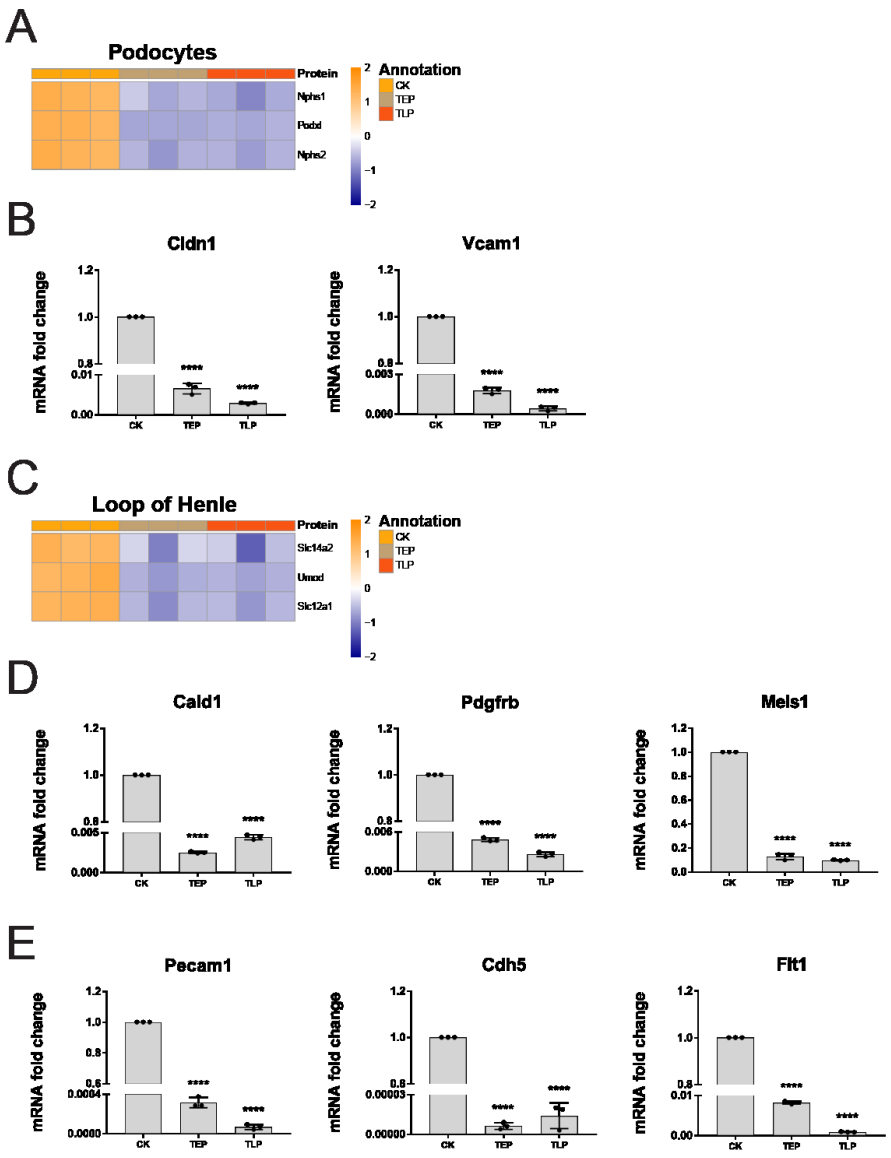

Figure 11

Markers of podocytes, parietal glomerular epithelial cells, Loop of Henle cells, stromal cells and endothelial cells are not present in the tubuloids. (A) A proteomic heatmap for the markers of podocytes, Nephrin (Nphs1), Podocalyxin (Podxl) and Podocin (Nphs2), in both early (TEP) and long-term (TLP) passage tubuloids in comparison to the mouse kidney epithelia (CK). (B) A real-time qPCR analysis of gene expression of the markers of parietal glomerular epithelial cells, Cldn1 and Vcam1, in both early (TEP) and long-term (TLP) passage tubuloids in comparison to whole mouse kidney cells (CK). (C) A proteomic heatmap for the markers of the Loop of Henle, Slc14a2, Uromodulin (Umod) and Slc12a1, in both early (TEP) and long-term (TLP) passage tubuloids in comparison to the mouse kidney epithelia (CK). (D) A real-time qPCR analysis of gene expression of the markers of stromal cells, Cald1, Pdgfrb and Meis1, in both early (TEP) and long-term (TLP) passage tubuloids in comparison to whole mouse kidney cells (CK). (E) A real-time qPCR analysis of gene expression of the markers of endothelial cells, Pecam1, Cdh5 and Flt1, in both early (TEP) and long-term (TLP) passage tubuloids in comparison to whole mouse kidney cells (CK). Data information: in A and C, the heatmaps show normalized log2 intensity values for 3 independent biological replicates of CK, TEP and TLP. A 5% FDR (adjusted P-value < 0.05) cutoff was applied for both

TEP over CK and TLP over CK. The values were scaled (z-score by row) with breaks from ≤ -2 to ≥ 2. In B/D/E, the graphs depict means ± SD (error bars). The ordinary one-way ANOVA followed by the Dunnett's multiple comparison to CK were performed; all P-values, 0.0001, ****p < 0.0001. 3 independent biological replicates in technical triplicates were examined.

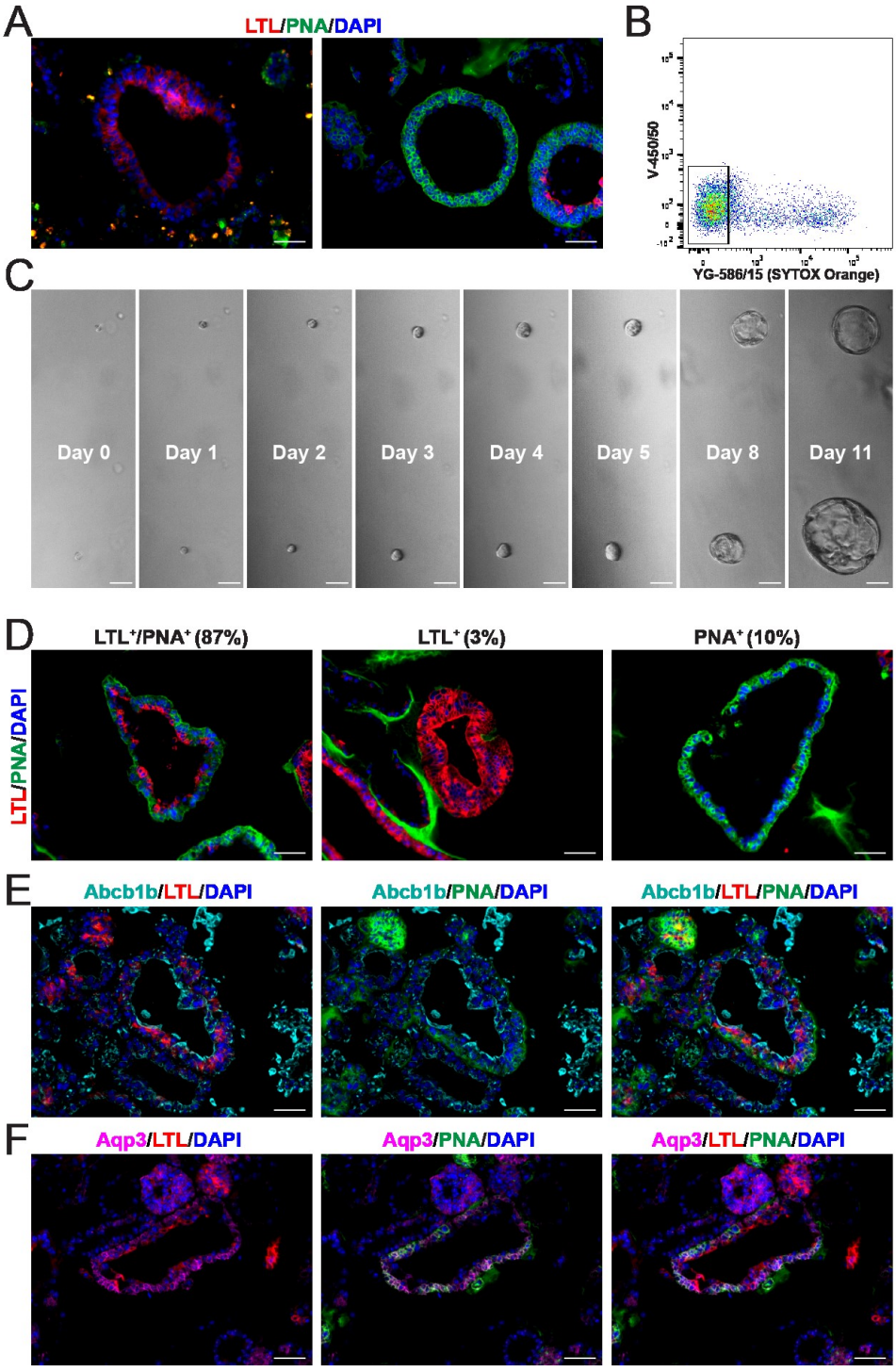

Figure 12

Tubuloid growth is driven by multipotent stem or progenitor cells. (A) Representative 2D immunofluorescence of tubuloids, which were positive for either LTL (red, left) or PNA (green, right). (B) A FACS histogram showing gating single viable cells from dissociated tubuloids, which were negative for SYTOX Orange (YG-586/15 fluorochrome). Signal measurement of a V-450/50 fluorochrome was performed to exclude autofluorescence of the cells. (C) Brightfield images acquired on consecutive days of two representative tubuloids formed independently from FAC-sorted cells. (D) Representative 2D immunofluorescence of the tubuloids grown from FAC-sorted cells, which were positive for either both LTL

(red) and PNA (green) (left) or LTL (middle) or PNA (right) only. (E) Representative 2D immunofluorescence of the tubuloids grown from FAC-sorted cells, which were positive for Abcb1b (cyan), LTL (red) and PNA (green). (F) Representative 2D immunofluorescence of the tubuloids grown from FAC-sorted cells, which were positive for Aqp3 (magenta), LTL (red) and PNA (green). Data information: scale bars in A/C/D/E/F, 50 μm. In A/D/E/F, nuclei are counterstained with DAPI. For quantification in D, 140 tubuloids were counted in total. In A, 3 independent biological replicates were examined; in B-F, one independent biological replicate was examined.

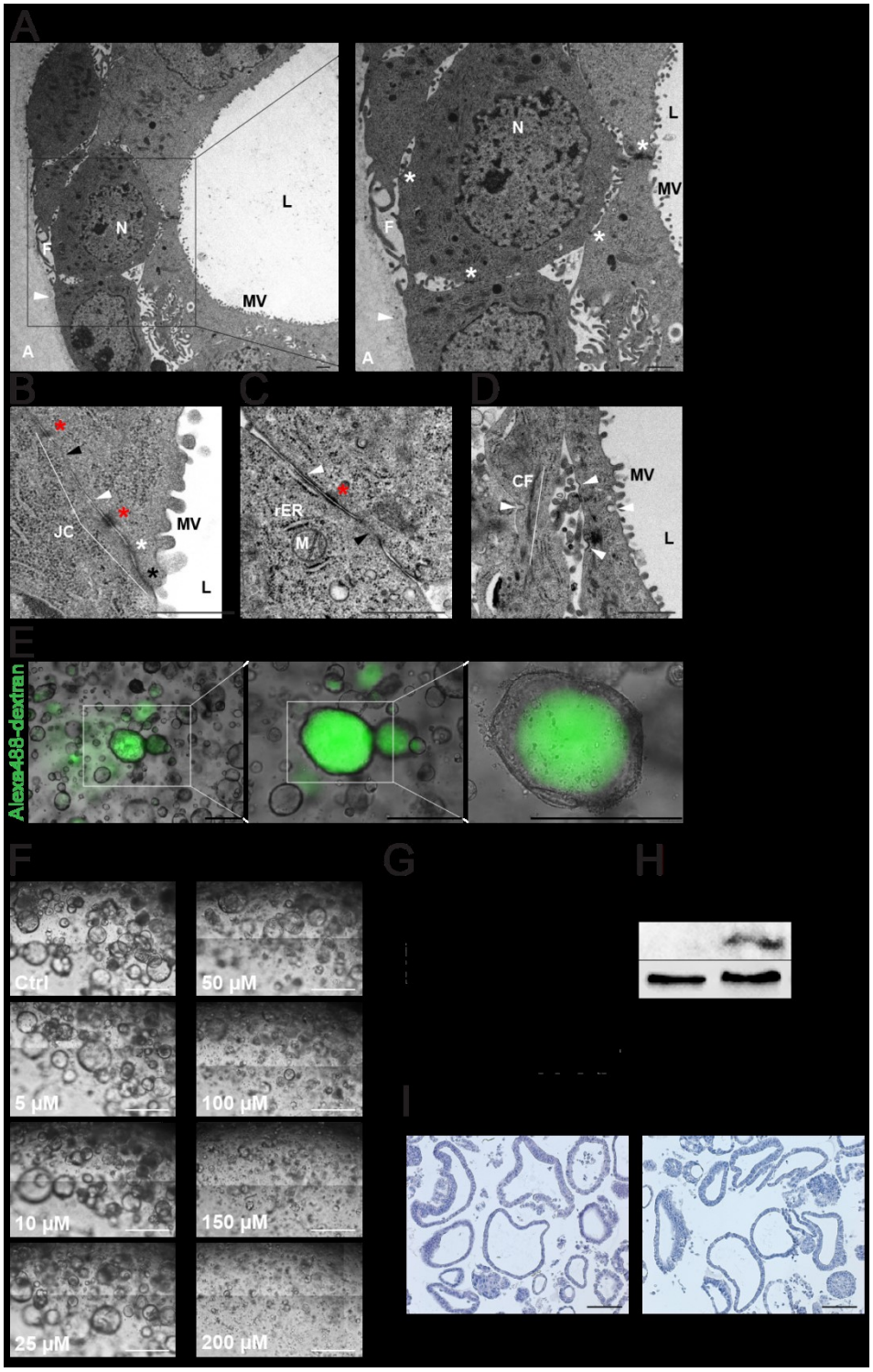

Figure 13

The tubuloids display tubular epithelial polarity, complexity and functionality. (A) Transmission electron microscopy of a representative cystic tubuloid with visible microvilli (MV) at the luminal side (L), a basal lamina without MV at the opposite basal side (arrowhead), filopodia (F), cell-cell contacts (asterisks) and a surrounding agarose (A). (B) A detailed view showing an epithelial junctional complex (JC) between the lateral membranes of neighboring cells. Shown are a tight junction (zonula occludens, black asterisk), an adherens junction (belt desmosome, zonula adhaerens, white asterisk), spot desmosomes (macula

adhaerens, red asterisks) and closely aligned or nearly fused lateral membranes (white and black arrowhead, respectively). (C) A detailed view of a cell at the basal side. Shown are a spot desmosome (red asterisk) and closely aligned or nearly fused lateral membranes (white and black arrowhead, respectively). (D) A detailed view of endocytic events at the apical and lateral membranes with visible clathrin-coated pits (diameter of around 100 nm, arrowheads). (E) Fluorescence of endocytosed Alexa488-conjugated dextran (green) in a representative cystic tubuloid. (F) Representative brightfield images of a tubuloid culture at indicated cisplatin concentrations (μM) on day 6 of treatment. (G) A curve showing the dependence of tubuloid viability (fold change ATP luminescence) on log10 cisplatin concentration (μM) on day 6 of treatment. (H) Representative immunoblotting for Cleaved Caspase-3 from lysates from the tubuloids treated with 100 μM cisplatin for 72 hrs. (I) Representative H&E staining of a tubuloid culture upon treatment with cisplatin at the IC50 concentration. Data information: scale bars, 1 μm in A-D, 500 μm in E and F, 100 μm in I. Abbreviations in A-E; N, nucleus; M, mitochondrion; rER, rough endoplasmatic reticulum (dark ordered dots); CF, cytoskeleton filaments (actin, dark structures along the white line). In A and E, insets are enlarged on the right. For quantification in E, percentages of the tubuloids positive for Alexa488-conjugated dextran with diameters ≥ 100 μm were calculated per well and averaged. 32% of the tubuloids were positive. Ctrl in F-I, the tubuloids treated with DMSO at respective concentrations. In G, the curve depicts means ± SD (error bars). Cisplatin exhibited the IC50 of 57.07 μM. In A/B/C/D/H/I, 3 independent biological replicates were examined. In E-G, 3 independent biological replicates in technical triplicates (wells) were examined.

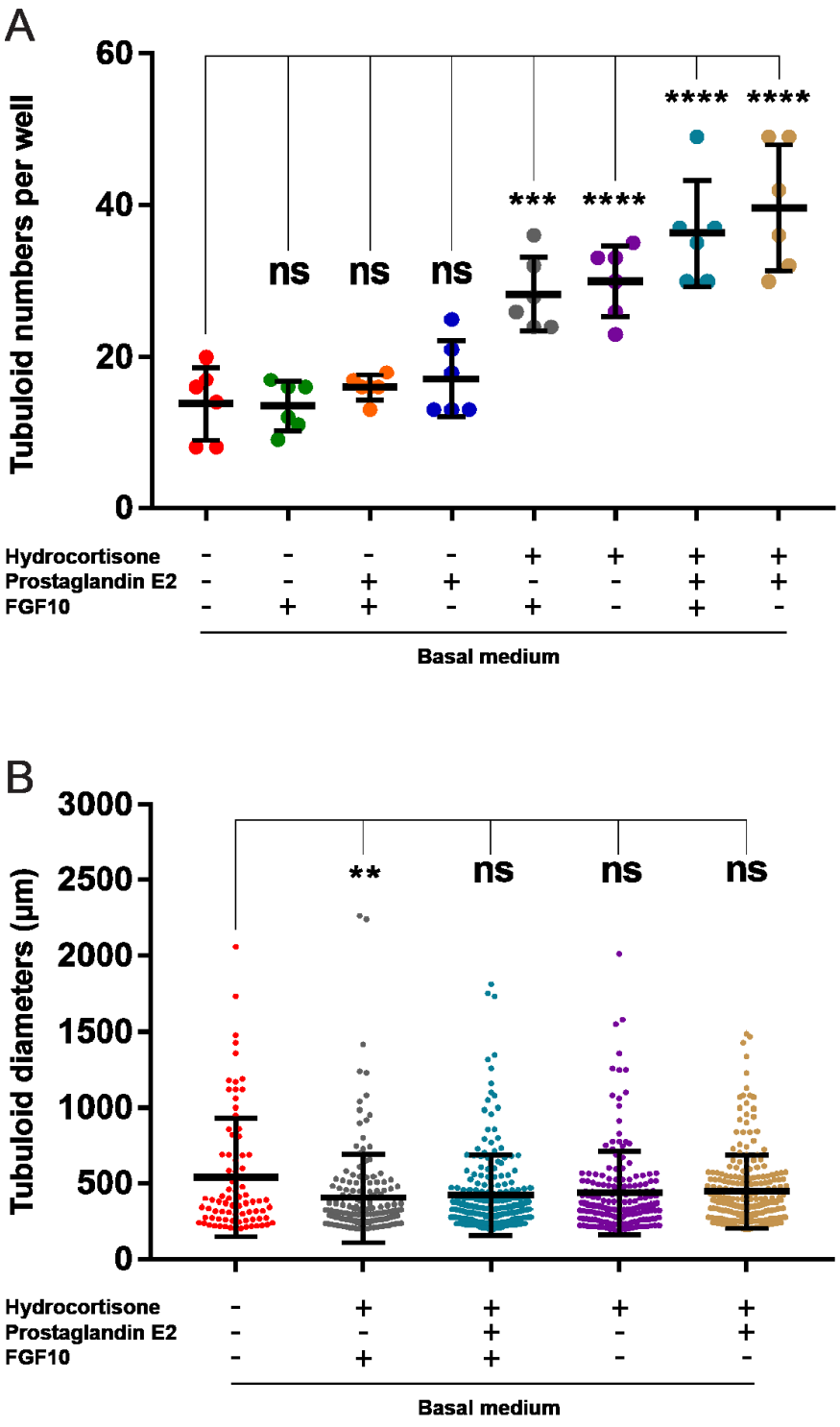

Figure 14

Hydrocortisone (HC) and prostaglandin E2 (PGE2) increase plating efficiency of tubuloid cultures. (A) Tubuloid numbers per well with indicated growth factor combinations. (B) Diameters (µm) of the tubuloids (single dots) from all wells with 4 selected growth factor combinations. Data information: a basal culture medium containing DMEM/F12 with GlutaMax, HEPES, N-acetylcysteine, B27, N2, nicotinamide, EGF, R-spondin-1 and the TGFβ inhibitor (TGFβi) A83-01 is common to all conditions. For quantification, 10^5 cells were freshly seeded and the tubuloids with diameters ≥ 200 µm were counted after 14 days of culturing. The graphs depict means ± SD (error bars). In A, data passed the Shapiro-Wilk normality test (α = 0.05). The

ordinary one-way ANOVA followed by the Dunnett's multiple comparison to the basal medium (first from the left) were performed; P-values from the left to the right, 0.9999, 0.9695, 0.8038, 0.0002, 0.0001, 0.0001, 0.0001; ****p < 0.0001, ***p < 0.001, ns: non-significant. In B, data did not pass the Shapiro-Wilk normality test (α = 0.05). The alternative non-parametric Kruskal-Wallis test followed by the Dunn's multiple comparison to the basal medium (first from the left) were performed; P-values from the left to the right, 0.0068, 0.2547, 0.8558, > 0.9999; **p < 0.01, ns: non-significant. One independent biological replicate with 6 technical replicates (wells) was examined.

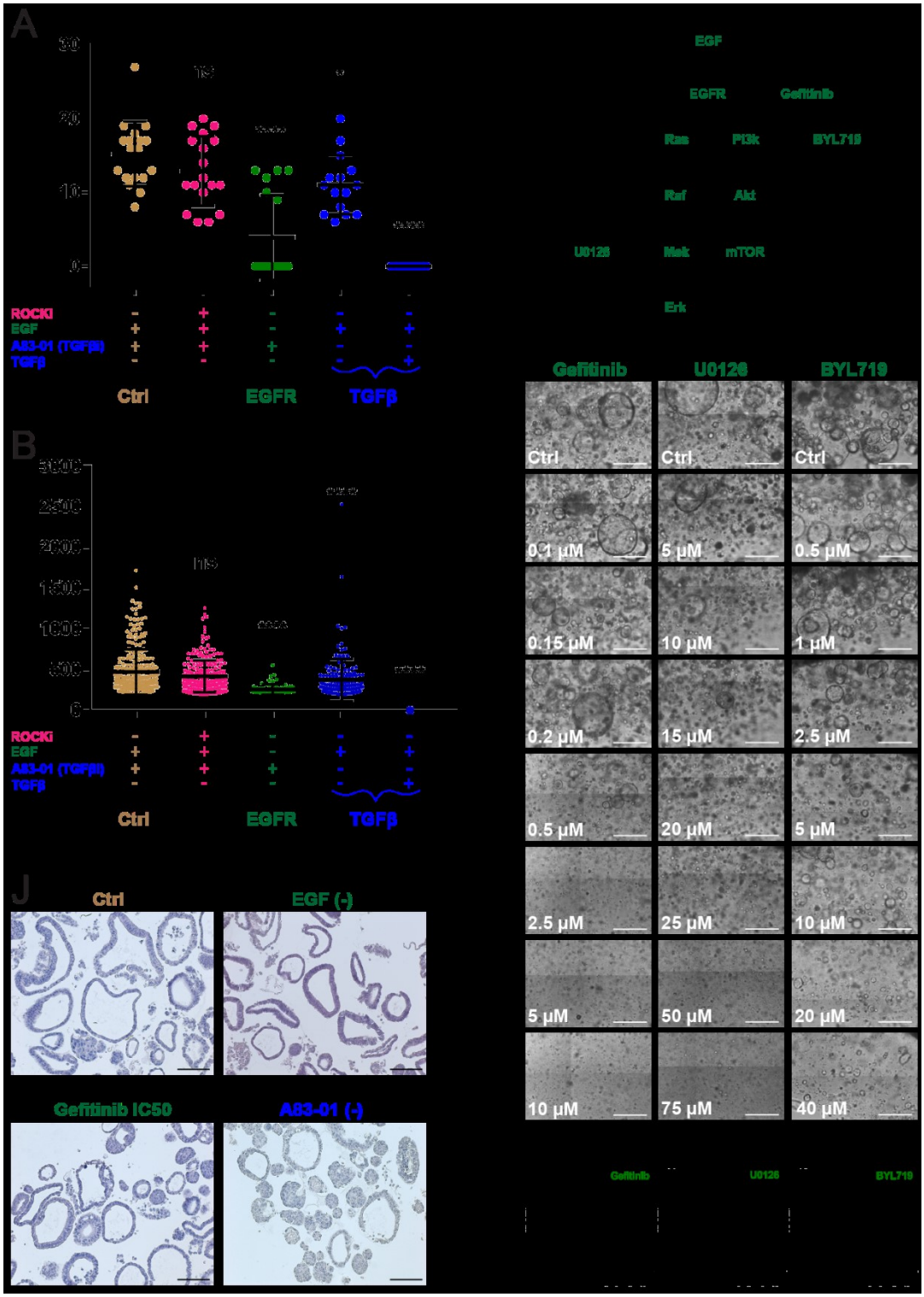

Figure 15

EGF receptor and TGFβ signaling drive tubuloid formation and growth. (A) Tubuloid numbers per well with indicated growth factor combinations (withdrawal and/or addition). (B) Diameters (µm) of the tubuloids (single dots) from all wells with indicated growth factor combinations (withdrawal and/or addition). (C) Scheme of the EGF receptor signaling with marked targets for the small-molecule inhibitors gefitinib, U0126 and BYL719. (D/F/H) Representative brightfield images of tubuloid cultures at indicated gefitinib (D), U0126 (F) and BYL719 (H) concentrations (µM) on day 6 of treatment. (E/G/I) Curves showing the dependence of

tubuloid viability (fold change ATP luminescence) on log10 gefitinib (E), U0126 (G) and BYL719 (I) concentration (μM) on day 6 of treatment. (J) Representative H&E staining of tubuloid cultures upon removal of EGF or A83-01 or treatment with gefitinib at the IC50 concentration. Data information: in A and B, a culture medium containing DMEM/F12 with GlutaMax, HEPES, N-acetylcysteine, B27, N2, nicotinamide, hydrocortisone (HC) and prostaglandin E2 (PGE2) is common to all conditions. Abbreviations; ROCKi, ROCK inhibitor; TGFβi, TGFβ inhibitor; EGFR, EGF receptor. For quantification, 10^5 cells were freshly seeded and the tubuloids with diameters ≥ 200 μm were counted after 14 days of culturing. The graphs depict means ± SD (error bars). In A, data passed the Shapiro-Wilk normality test (α = 0.05). The ordinary one-way ANOVA followed by the Dunnett's multiple comparison to the complete tubuloid medium (Ctrl, first from the left) were performed; P-values from the left to the right, 0.2974, 0.0001, 0.0234, 0.0001; ****p < 0.0001, *p < 0.05, ns: non-significant. In B, data did not pass the Shapiro-Wilk normality test (α = 0.05). The alternative non-parametric Kruskal-Wallis test followed by the Dunn's multiple comparison to the complete tubuloid medium (Ctrl, first from the left) were performed; P-values from the left to the right, > 0.9999, < 0.0001, < 0.0001, < 0.0001; ****p < 0.0001, ns: non-significant. In A and B, 3 independent biological replicates with 6 technical replicates (wells) were examined and collectively shown. Ctrl in D-I, the tubuloids cultured in the complete medium and treated with DMSO at respective concentrations. Scale bars in D/F/H, 500 μm. In E/G/I, the curves depict means ± SD (error bars). In E, gefitinib exhibited the IC50 of 0.43 μM; in G, U0126 exhibited the IC50 of 23.49 μM; in I, BYL719 exhibited the IC50 of 17.83 μM. In D-I, 3 independent biological replicates in technical triplicates (wells) were examined. Ctrl in J, the tubuloids cultured in the complete medium and treated or not with DMSO at a respective concentration. Scale bars, 100 μm. 3 independent biological replicates were examined.

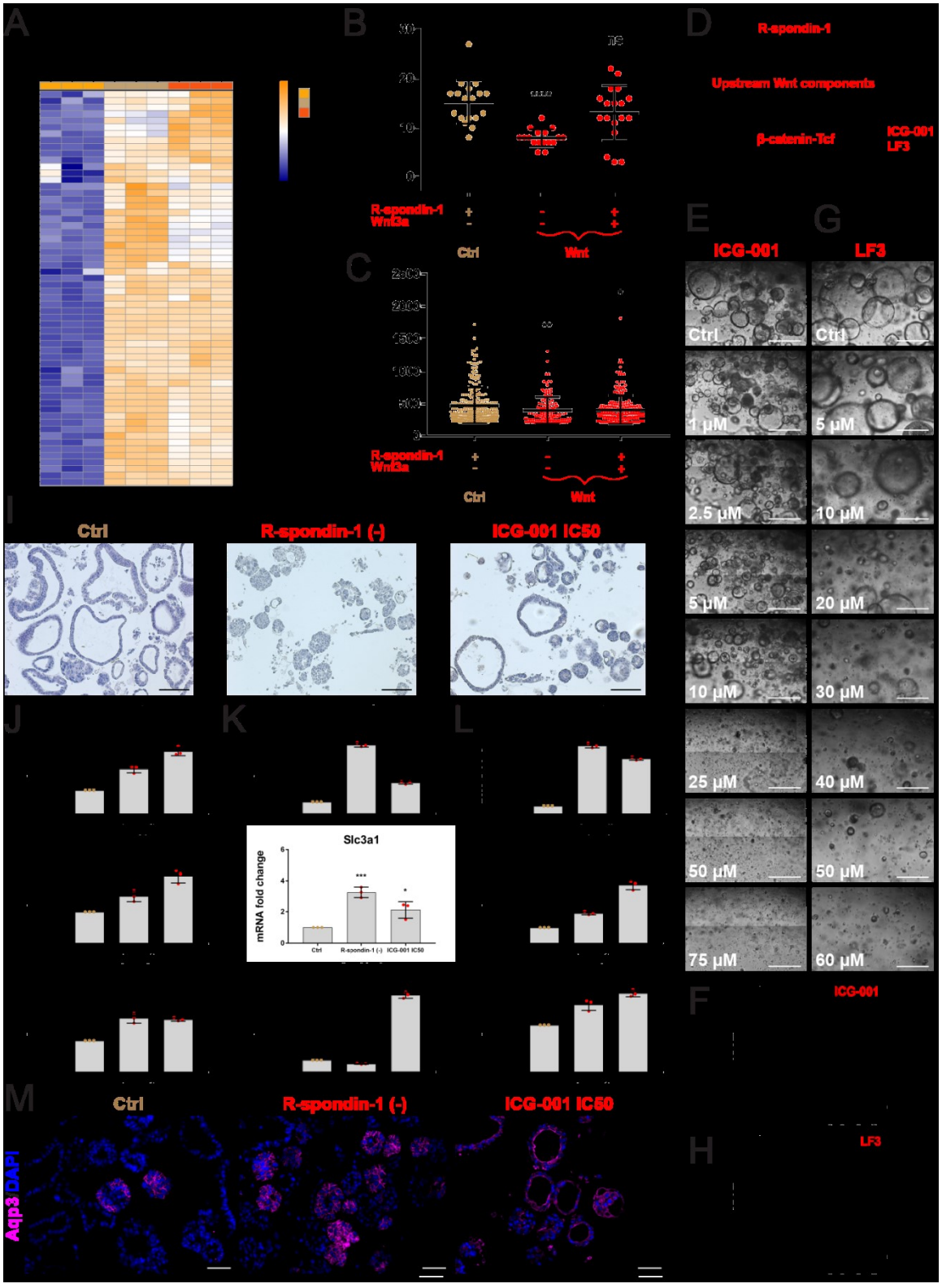

Figure 16

Wnt signaling controls tubuloid formation, growth and differentiation. (A) A proteomic heatmap for components of Wnt signaling in both early (TEP) and long-term (TLP) passage tubuloids in comparison to the mouse kidney epithelia (CK). (B) Tubuloid numbers per well with indicated growth factor combinations (withdrawal or addition). (C) Diameters (µm) of the tubuloids (single dots) from all wells with indicated growth

factor combinations (withdrawal or addition). (D) Scheme of Wnt signaling with a marked common target for the small-molecule inhibitors ICG-001 and LF3. (E and G) Representative brightfield images of tubuloid cultures at indicated ICG-001 (E) and LF3 (G) concentrations (μM) on day 6 of treatment. (F and H) Curves showing the dependence of tubuloid viability (fold change ATP luminescence) on log10 ICG-001 (F) and LF3 (H) concentration (μM) on day 6 of treatment. (I) Representative H&E staining of tubuloid cultures upon R-spondin-1 removal or treatment with ICG-001 at the IC50 concentration. (J) A real-time qPCR analysis of gene expression of the differentiation markers Krt8, Krt18 and Cldn4 in the tubuloids upon R-spondin-1 removal or treatment with ICG-001 at the IC50 concentration. (K) A real-time qPCR analysis of gene expression of the markers of proximal tubular cells, Abcb1b, Slc3a1 and Slc40a1, in the tubuloids upon R-spondin-1 removal or treatment with ICG-001 at the IC50 concentration. (L) A real-time qPCR analysis of gene expression of the markers of the distal nephrons, Aqp3, Atp6ap2 and Wnk1, in the tubuloids upon R-spondin-1 removal or treatment with ICG-001 at the IC50 concentration. (M) Representative 2D immunofluorescence for Aqp3 (magenta) in the tubuloids upon R-spondin-1 removal or treatment with ICG-001 at the IC50 concentration. Data information: in A, the heatmap shows normalized log2 intensity values for 3 independent biological replicates of CK, TEP and TLP. A 5% FDR (adjusted P-value < 0.05) cutoff and a log2 fold change cutoff of > 0 were applied for both TEP over CK and TLP over CK. The values were scaled (z-score by row) with breaks from ≤ -2 to ≥ 2. In B and C, a culture medium containing DMEM/F12 with GlutaMax, HEPES, N-acetylcysteine, B27, N2, nicotinamide, hydrocortisone (HC) and prostaglandin E2 (PGE2) is common to all conditions. For quantification, 10^5 cells were freshly seeded and the tubuloids with diameters ≥ 200 μm were counted after 14 days of culturing. The graphs depict means ± SD (error bars). In B, data passed the Shapiro-Wilk normality test (α = 0.05). The ordinary one-way ANOVA followed by the Dunnett's multiple comparison to the complete tubuloid medium (Ctrl, first from the left) were performed; P-values from the left to the right, 0.0001, 0.2132; ****p < 0.0001, ns: non-significant. In C, data did not pass the Shapiro-Wilk normality test (α = 0.05). The alternative non-parametric Kruskal-Wallis test followed by the Dunn's multiple comparison to the complete tubuloid medium (Ctrl, first from the left) were performed; P-values from the left to the right, 0.0090, 0.0129; **p < 0.01, *p < 0.05. In B and C, 3 independent biological replicates with 6 technical replicates (wells) were examined and collectively shown. Ctrl in E-H, the tubuloids cultured in the complete medium and treated with DMSO at respective concentrations. Scale bars in E and G, 500 μm. In F and H, the curves depict means ± SD (error bars). In F, ICG-001 exhibited the IC50 of 14.66 μM; in H, LF3 exhibited the IC50 of 15.72 μM. In E-H, 3 independent biological replicates in in technical triplicates (wells) were examined. Ctrl in I-M, the tubuloids cultured in the complete medium and treated or not with DMSO at a respective concentration. Scale bars in I, 100 μm. 3 independent biological replicates were examined. In J-L, the graphs depict means ± SD (error bars). The ordinary one-way ANOVA followed by the Dunnett's multiple comparison to Ctrl were performed; P-values from the left to the right in J; 0.0004, 0.0001 for Krt8; 0.0153, 0.0002 for Krt18; 0.0002, 0.0003 for Cldn4; in K: 0.0001, 0.0001 for Abcb1b; 0.0005, 0.0164 for Slc3a1; 0.0910, 0.0001 for Slc40a1; in L: 0.0001, 0.0001 for Aqp3; 0.0014, 0.0001 for Atp6ap2; 0.001, 0.0001 for Wnk1; ****p < 0.0001, ***p < 0.001, **p < 0.01, *p < 0.05, ns: non-significant. 3 independent biological replicates in technical triplicates were examined. Scale bars in M, 50 μm. 3 independent biological replicates were examined.

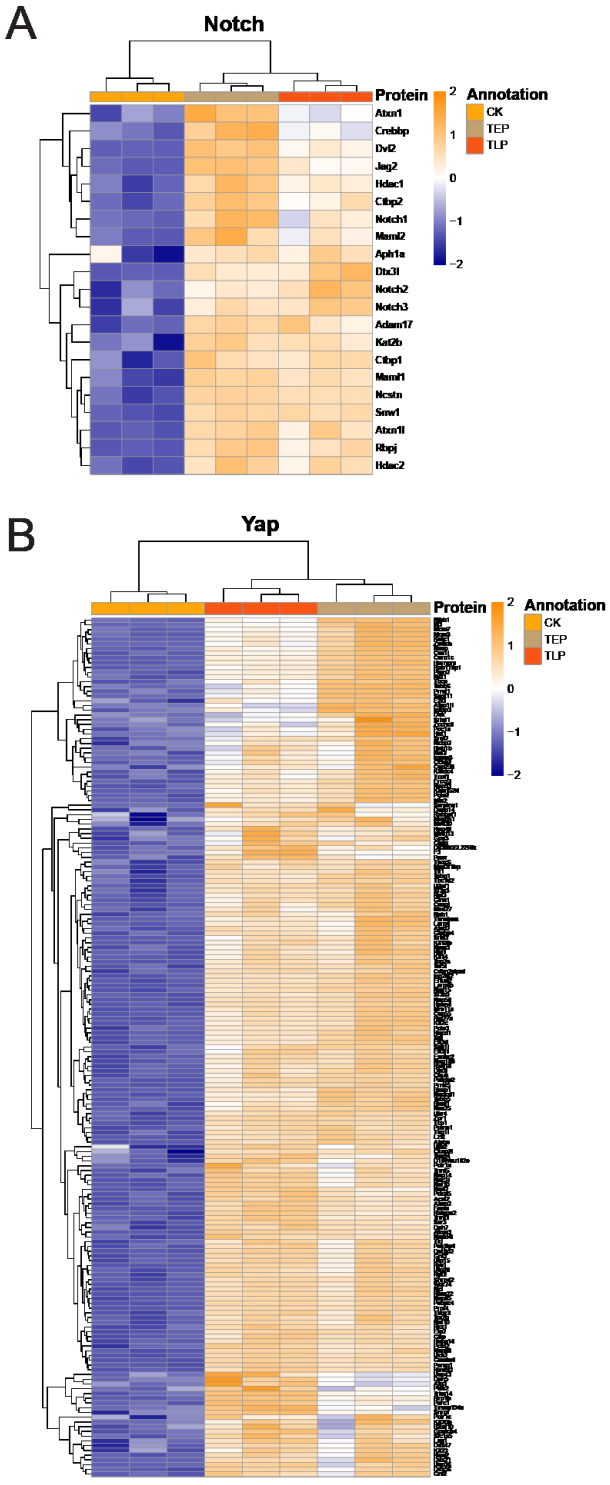

Figure 17

Notch and Yap signaling systems are upregulated in the tubuloids. (A) A proteomic heatmap for components of Notch signaling in both early (TEP) and long-term (TLP) passage tubuloids in comparison to the mouse kidney epithelia (CK). (B) A proteomic heatmap for direct Yap targets in both early (TEP) and long-term (TLP) passage tubuloids in comparison to the mouse kidney epithelia (CK). Data information: the heatmaps show normalized log2 intensity values for 3 independent biological replicates of CK, TEP and TLP. A 5% FDR (adjusted P-value < 0.05) cutoff and a log2 fold change cutoff of > 0 were applied for both TEP over CK and TLP over CK. The values were scaled (z-score by row) with breaks from ≤ -2 to ≥ 2.

2. Genetic mouse models with β-catenin-GOF, Notch-GOF and Vhl-LOF to study kidney tumorigenesis

Our laboratory identified and characterized the $CXCR4^{+}MET^{+}CD44^{+}$ CSCs from primary human ccRCCs, which exhibit the activation of Wnt and Notch signaling. Treatments with small-molecule inhibitors of Wnt and Notch revealed that both signaling systems are crucial for self-renewal of the CSCs in Matrigel-based 3D organoids and non-adherent spheres in culture and for subcutaneous and orthotopic tumor growth in PDXs. This work was published in *Nature Communications* with my co-authorship (Fendler, Myszczyszyn *et al*, 2020).

2.1. Generation of the mutant mice

To functionally test the importance of Wnt and Notch signaling for ccRCC development *in vivo*, also in the context of Vhl deficiency, I aimed at generating genetic mouse models with the overactivation of β-catenin and Notch1 intracellular domain (Notch1 icd, N1icd) with or without Vhl deletion in adult kidney epithelial cells based on Cre-loxP-mediated recombination. For this purpose, I took advantage of the doxycycline-inducible Tet-on Pax8-reverse tetracycline-controlled transactivator (rtTA)-LC1-Cre transgenic system, which consists of the Pax8-rtTA and LC1-Cre constructs (Figure 18). The Pax8-rtTA construct is integrated in an exogenous Pax8 locus (Traykova-Brauch *et al*, 2008), while the LC1-Cre transcription unit is located in the LC1 locus (Schönig *et al*, 2002). The Pax8-rtTA construct drives high expression of rtTA to proximal and distal tubular epithelial cells as well as to collecting duct cells of both embryonic and adult kidneys under control of the upstream regulatory region of the Pax8 promoter. Pax8-rtTA is not active in parietal and visceral glomerular epithelial cells and in podocytes. No extrarenal Pax8-rtTA activity occurs in any other major adult tissue, including heart, lung, brain, spleen, thyroid and colon, apart from only a small subset of hepatocytes (Traykova-Brauch *et al*, 2008). The LC1-Cre construct, generated 20 years ago with a significant contribution of Klaus Rajewsky, currently group leader at the MDC, enables the expression of the Cre recombinase under control of the tetracycline-responsive P_{tet} promoter, which is activated through the binding of rtTA in the presence of doxycycline (Schönig *et al*, 2002). Therefore, the Pax8-rtTA-LC1-Cre system provides tight control over the location, i.e. tissue specificity, and timing of Cre-loxP recombination upon doxycycline induction (Schönig *et al*, 2002; Traykova-Brauch *et al*, 2008).

I began with generating double mutant mice with constitutive heterozygous overactivation (gain of function, GOF) of *β-catenin* and *N1icd*; β-catenin-GOF; Notch-

GOF; and with homozygous deletion (loss of function, LOF) of *Vhl* and heterozygous GOF of *β-catenin*; Vhl-LOF; β-catenin-GOF. Vhl-LOF; Notch-GOF mutant mice had already been established using different Cre systems (Bhagat *et al*, 2017; Johansson *et al*, 2016). To prepare the mutant mice, I crossed Pax8-rtTA; LC1-Cre mice with transgenic mice, in which exon 3 of *β-catenin* that carried phosphorylation sites for Gsk3β was flanked by loxP fragments in the endogenous locus (Harada *et al*, 1999). Then, I crossed the resulting mice either with transgenic mice, in which loxP sites flanked the *Vhl* promoter and the first exon in the endogenous locus (Haase *et al*, 2001), or with mice that contained a sequence encoding the C-terminally truncated form of *N1icd* (amino acids 1749-2293) under control of the ubiquitously expressed *Rosa26* locus. The expression of *N1icd* was blocked by a loxP-flanked stop fragment placed between the *Rosa26* promoter and the coding sequence (Murtaugh *et al*, 2003). As a result, I obtained Pax8-rtTA(+); LC1-Cre(+); β-catenin-loxP/wt; Notch-loxP/wt and Pax8-rtTA(+); LC1-Cre(+); Vhl-loxP/loxP; β-catenin-loxP/wt mice. Cre-loxP-mediated recombination upon doxycycline administration led to deletion of exon 3 of *β-catenin*, and thus to β-catenin-GOF by its stabilization and cytoplasmic accumulation (Harada *et al*, 1999). Recombination in the *Vhl* construct resulted in Vhl-LOF by deletion of its promoter and exon 1 (Haase *et al*, 2001). Recombination in the *N1icd* construct led to excision of the stop cassette, followed by Notch-GOF (Murtaugh *et al*, 2003).

2.2. Doxycycline-induced recombination

According to the original studies of the Pax8-rtTA-LC1-Cre system (Schönig *et al*, 2002; Traykova-Brauch *et al*, 2008), preliminary doxycycline treatments using three concentrations (0.2, 1 or 2 mg/ml) and times (2, 5 or 10 days) were performed to determine the most appropriate parameters for recombination in the kidney (data not shown). For this purpose, I used the adult one-month-old Pax8-rtTA(+); LC1-Cre(+); LacZ(+) mice, which carried in the *Rosa26* locus a loxP-flanked stop cassette upstream of the lacZ sequence encoding β-galactosidase. Removal of the cassette upon recombination resulted in β-galactosidase expression (Soriano, 1999). The active enzyme could be detected upon hydrolysis of the artificial chromogenic substrate X-gal, which led to the formation of a blue product. I analyzed cellular patterns of Cre activity and found that 0.2 mg/ml doxycycline administered for 5 days was the optimum to induce recombination efficiently and repetitively (Figure 19A). Immunohistochemistry demonstrated that Cre was present in the nuclei of the majority of kidney epithelial cells in both the cortex and medulla, including proximal tubular cells (marked by red lines), most likely the cells of ccRCC origin. Glomeruli (marked by black lines) remained negative. This pattern was covered by cytoplasmic LacZ staining (Figure 19B). I did not

observe Cre- and LacZ-positive cells in the doxycycline-treated Pax8-rtTA(-); LC1-Cre(+); LacZ(+) control kidneys, confirming that the genetic system was not leaky. To induce recombination in the Pax8-rtTA(+); LC1-Cre(+); β-catenin-loxP/wt; Notch-loxP/wt and Pax8-rtTA(+); LC1-Cre(+); Vhl-loxP/loxP; β-catenin-loxP/wt mice (n = 20 per line), I treated them with doxycycline. In parallel, I treated control mice carrying β-catenin- and Notch- or β-catenin- and Vhl-loxP alleles, but no Pax8-rtTA or LC1-Cre (n = 20).

2.3. Macroscopic phenotypes of the mutant mice

All induced mice from both mutant lines developed severe illness symptoms between 1st and 8th month after doxycycline induction and were therefore withdrawn from the study according to the score sheet. In average, both mutant mice developed the symptoms after around 4 months from treatment. None of control mice appeared sick after 8 months from induction. Average body weight of the mutant mice was reduced (Figure 20A). The kidneys from the mutant mice were smaller, while the spleens were enlarged (splenomegaly), comparing to control mice. Both the kidneys and spleens from the mutant mice were pale, suggesting disorder of erythrocytes. I did not observe tumors in the mutant kidneys (Figure 20B). The mutant mice displayed the decrease in average weight of the kidneys (Figure 20C) and the increase in average weight of the spleens (Figure 20D), consistent with the macroscopic observation of their sizes.

2.4. β-catenin, Notch and Vhl mutagenesis

I analyzed recombination of the β-catenin-, Notch- and Vhl-loxP alleles in the mutant kidneys on genomic DNA, protein and mRNA target gene levels. To quantitatively assess the abundance of the recombined *β-catenin* allele in relation to the wild-type (wt) allele on DNA level, I performed two-primer-based PCR amplification of a fragment of the *β-catenin* gene, which carried loxP-flanked exon 3. However, simultaneous amplification of the unrecombined loxP allele in one reaction was impossible due to its size. Bands of the amplified recombined (700 bp) and wt (900 bp) *β-catenin* allele from both kidney mutants were visible on agarose gel, as compared to respective control kidneys with only the wt allele (Figure 21A). For quantitative analysis of the recombined *Vhl* allele in relation to the loxP allele, I conducted three-primer-based PCR amplification of a fragment of the *Vhl* gene, which carried the loxP-flanked promoter and exon 1. I detected bands of the amplified recombined (260 bp) and unrecombined loxP (460 bp) *Vhl* allele from the Vhl-LOF; β-catenin-GOF kidney mutant, as opposed to respective control kidneys with only the loxP allele (Figure 21B). I did not manage to amplify the recombined *N1icd* allele. Using immunoblotting, I evaluated recombination by the presence of the mutant β-catenin protein without the fragment encoded by exon 3. The

recombined β-catenin protein accumulated in both kidney mutants, which was visualized as 72-kDa band, as compared to control kidneys with only the wt protein observed as 95-kDa band (Figure 21C). Then, I tested for quantitative expression of selected classical β-catenin, Notch and HIF-1α/2α (stabilized upon Vhl loss) target genes by real-time qPCR. The expression of the β-catenin target genes *Dkk1*, *Axin2*, *Cyclin D1* and *Myc* in the β-catenin-GOF; Notch-GOF and Vhl-LOF; β-catenin-GOF kidney mutants was strongly upregulated, as opposed to control mice (Figure 21D and E). The expression of the Notch target genes *Hey1*, *Hes1* and *Hey3 (Heyl)* in the β-catenin-GOF; Notch-GOF kidney mutant (Figure 21F) and the expression of the HIF-1α/2α target genes *Ca9*, *Hk2*, *Pdk1*, *Myc*, *Ldha*, *Cyclin D1*, *Glut1* and *Vegfa* in the Vhl-LOF; β-catenin-GOF kidney mutant (Figure 21G) also significantly increased, as compared to control mice. Altogether, my data show that targeted mutagenesis in the mouse kidneys was successful and mutant cells were not cleared with time.

2.5. No tumorigenesis was observed in the mutant kidneys

For histological examination of the mutant kidneys, I performed PAS staining, which detected kidney tissue structures containing high proportions of sugar macromolecules such as tubular and glomerular basement membranes and the brush border of proximal tubules. Microscopical examination by a pathologist from the Charité did not reveal any signs of tumors or precancerous lesions in any of the mutant mice, even after 8 months upon doxycycline induction. Any typical non-neoplastic pathological changes of the kidney tissue, like cysts, hypertrophy, necrosis, dilation and atrophy (degeneration) of the tubules as well as tubulointerstitial fibrosis, were also not present (Figure 22A). The pathologist observed a so-called nuclear crowding in some tubules in the outer part of the cortex in all β-catenin-GOF; Notch-GOF, but not in the Vhl-LOF; β-catenin-GOF mutant kidneys (Figure 22B). However, the significance of this phenomenon in the β-catenin-GOF; Notch-GOF mutant kidneys is unknown.

To analyze carcinogenesis in the mutant kidneys on cellular level, I conducted Ki67 staining to test for the increase in proliferating cells at the G1, S, G2 and M phases. None of the mutant kidneys, even after 8 months upon doxycycline treatment, displayed higher cell proliferation rates, as shown by similar numbers of Ki67-positive nuclei to control kidneys (Figure 23A and B), despite the upregulation of *Cyclin D1* and *Myc* involved in cell cycle progression (Figure 21D and E).

In the kidney, Vhl loss or Wnt signaling overactivation alone are known to cause DNA damage and/or p21-dependent growth arrest or senescence, which constrain cell

transformation (Cole *et al*, 2010; Espana-Agusti *et al*, 2017). To test for these phenomena in the mutant kidneys, I analyzed the upregulation of the DNA damage marker phospho-γH2AX and of the growth arrest or senescence marker p21 and its transcriptional activator p53. However, immunohistochemistry neither demonstrated accumulation of phospho-γH2AX (Figure 24, left panel) nor p53 stabilization (Figure 24, middle panel) and p21 activation (Figure 24, right panel) in the nuclei of the mutant kidney cells. To exclude the alternative way of growth arrest or senescence stimulation via p16 in the mutant kidneys, I measured mRNA levels of p16 using real-time qPCR, but it was undetectable (data not shown). I also tested for induction of apoptosis in the mutant kidneys. For this, I performed TUNEL assay, which enables to detect blunt ends of double-stranded DNA breaks in late-apoptotic cells that undergo extensive DNA degradation. I did not observe the increase in the numbers of apoptotic cells in the mutant kidneys (Figure 25). Altogether, I found no signs of cell transformation in the mutant kidneys. Moreover, mutant cells did not undergo DNA damage, growth arrest, senescence or apoptosis.

2.6. The mutant mice displayed hallmarks of chronic kidney disease

The macroscopic view of the organs of the mutant mice suggested disorder of erythrocytes (Figure 20B). I performed blood test to measure the volume percentages of erythrocytes, the hematocrit. I found that erythrocyte percentages in the mutant mice decreased (Figure 26A), indicating anemia. Anemia is a clinical hallmark of chronic kidney disease (CKD) (Koury & Haase, 2015; Romagnani *et al*, 2017). CKD is a multi-stage syndrome defined as sustained alterations in kidney structure and function, which affect the health of individuals (Edeling *et al*, 2016; Ferenbach & Bonventre, 2015; Liu, 2011; Romagnani *et al*, 2017). In CKD, anemia can be a result of disturbed production of erythropoietin (EPO) in kidney interstitial cells (Koury & Haase, 2015). To test for this, I measured the concentration of EPO in the mouse blood plasma. Unexpectedly, the concentration of plasma EPO rose dramatically in the mutant mice, 314 times in the β-catenin-GOF; Notch-GOF mice and 930 times in the Vhl-LOF; β-catenin-GOF mice (Figure 26B). This suggests both a different mechanism of anemia downstream of EPO supply and a strong compensative positive feedback on EPO production in the mutant mice.

CKD development starts from sustained tubular injury, followed by prolonged tubulointerstitial inflammation. Inflammatory cells that infiltrate injured sites, mostly monocytes and/or macrophages, further enhance tubular damage, leading to kidney dysfunction (Edeling *et al*, 2016; Ferenbach & Bonventre, 2015; Liu, 2011). I analyzed

selected markers of kidney injury, failure and inflammation in the mutant mice. Gene expression analysis by real-time qPCR in whole kidneys revealed the upregulation of the tubular injury markers *Ngal*, *Kim-1* and *Gsta1* in the β-catenin-GOF; Notch-GOF (Figure 27A) and Vhl-LOF; β-catenin-GOF (Figure 27B) mutants, with strongly increased expression of the *Ngal* gene in both mutants. In the mouse blood, I measured the concentration of blood urea nitrogen (BUN), a typical marker of kidney failure. In the mutant mice, BUN concentration went up (Figure 27C). I evaluated kidney inflammation by gene expression analysis by real-time qPCR of the inflammatory cytokine *Il1b* and of the panel of the myeloid lineage immune cell markers, *Cd11b*, *Ly6c*, *Ccr2 (Cd192)* and *Cd68*, as well as of *Icam1 (Cd54)*, the ligand for Cd11b. Cd11b is expressed on all myeloid immune cells, i.e. monocytes, macrophages, granulocytes: basophils, neutrophils, eosinophils, and mast cells. Ly6c and Ccr2 are enriched on monocytes and Cd68 is present on all macrophages. The expression of *Il1b* and *Cd11b* was strongly upregulated in both mutant kidneys, while the expression of *Ly6c*, *Ccr2 (Cd192)*, *Cd68* and *Icam1 (Cd54)* was pronouncedly increased in the Vhl-LOF; β-catenin-GOF mutant, but not in the β-catenin-GOF; Notch-GOF mutant (Figure 28A and B). Inflammation can be another driver of anemia in CKD, either directly through inhibition of erythropoiesis or indirectly via disrupted iron regulation, which limits hemoglobin synthesis in erythroid cells in the bone marrow (Koury & Haase, 2015).

Splenomegaly in the mutant mice (Figure 20B) prompted me to analyze their spleens on the microscopical level. PAS staining demonstrated a disorganized cellular mass in the spleens from all mutant mice, instead of white pulp islands (marked by a white line) clearly separated from surrounding red pulp islands in control spleens (Mebius & Kraal, 2005) (Figure 29, upper panel). Detailed examination by a pathologist from the Charité revealed the presence of megakaryocytes (marked by the arrowheads) in the spleens from the mutant mice (Figure 29, middle and lower panel), which are characteristic for extramedullary hematopoiesis (EMH). EMH is a process in which erythroid, myeloid and platelet precursors expand and differentiate into effector cells outside the bone marrow in response to hematopoietic emergencies, including anemia. The spleen is a major site for EMH, with splenomegaly as a typical clinical manifestation (Chiu *et al*, 2015).

The most common pathological manifestation of end-stage CKD is tubulointerstitial fibrosis (Edeling *et al*, 2016; Ferenbach & Bonventre, 2015; Liu, 2011; Romagnani *et al*, 2017), which is the result of impaired tubular repair. Despite lack of fibrotic lesions in the mutant kidneys (Figure 22A), I tested in whole kidneys for the upregulation of classical fibrotic markers on mRNA target gene level by real-time qPCR. The expression of the

markers of activated myofibroblasts, *a-sma* and *Vim*, and of the markers of the accumulated extracellular matrix, *Fn1*, *Col1a1* and *Col3a1*, was not enhanced in the mutant kidneys (Figure 30A and B). Altogether, I conclude that the mutant mice exhibited features of CKD such as anemia as well as kidney injury, failure and inflammation, but no fibrosis. These pathologies underlay the moribund state of the mutant mice. I decided not to generate Vhl-LOF; β-catenin-GOF; Notch-GOF triple mutant mice. I presented my results on the double mutant mice at The Notch Meeting XI in Athens (Myszczyszyn *et al*, 2019c).

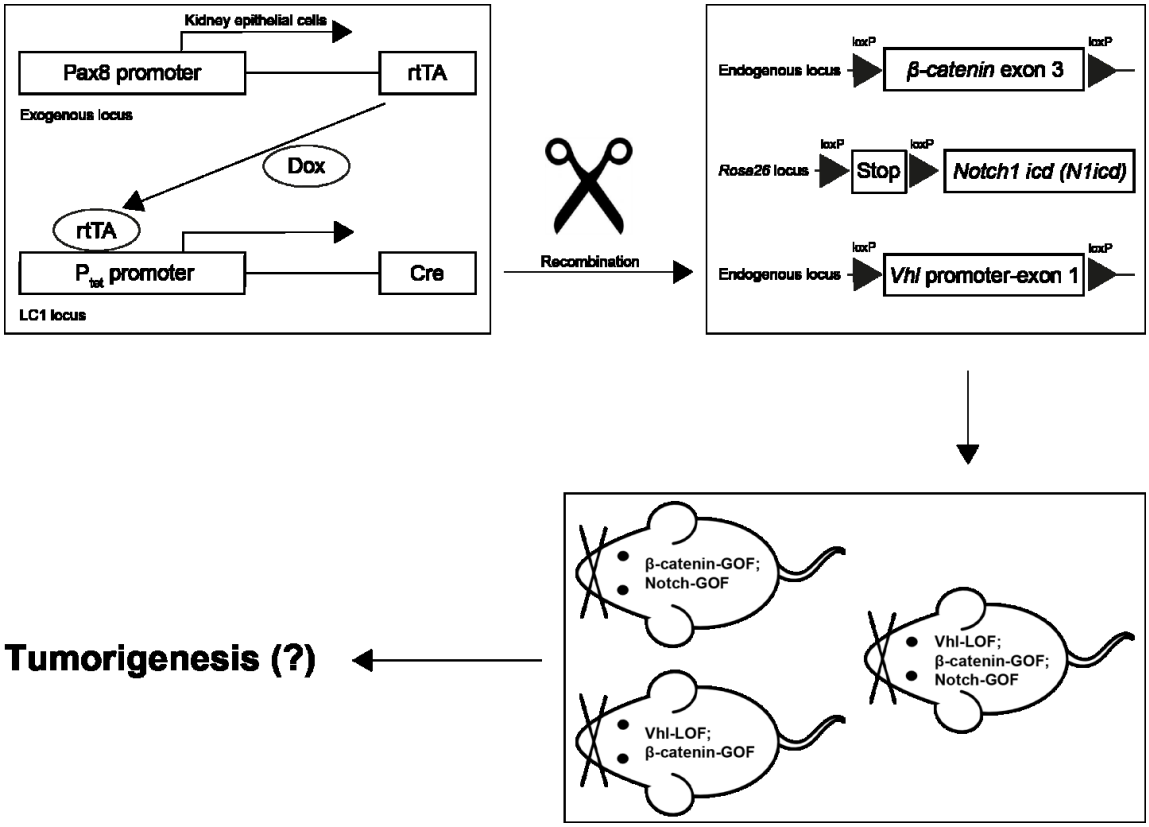

Figure 18

A scheme of the genetic approach to study ccRCC tumorigenesis in mice. Generation of β-catenin-GOF; Notch-GOF; Vhl-LOF; β-catenin-GOF and Vhl-LOF; β-catenin-GOF; Notch-GOF genetic mouse mutants based on the loxP-mediated recombination using the transgenic doxycycline-inducible Tet-on kidney epithelial cell-specific Pax8-rtTA-LC1-Cre system. Figure information: dox, doxycycline.

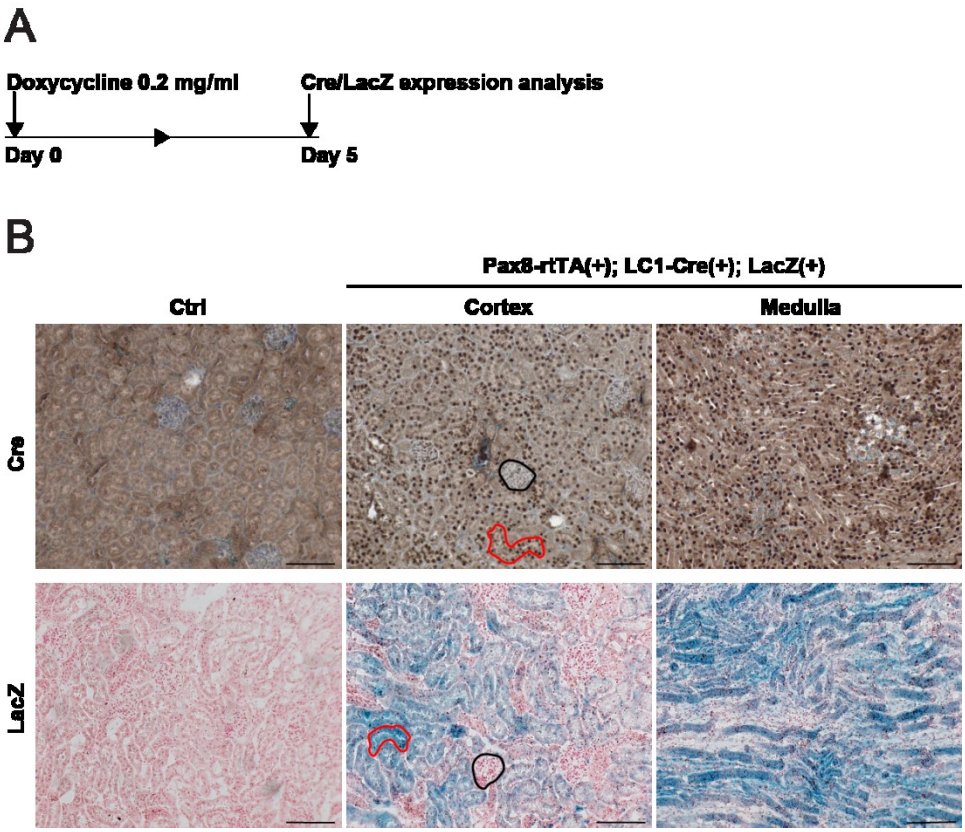

Figure 19

A pattern of recombination in the Pax8-rtTA(+); LC1-Cre(+); LacZ(+) mice. (A) A methodological scheme of doxycycline-mediated recombination. (B) Representative nuclear Cre (upper panel) and cytoplasmic LacZ (lower panel) expression in the kidney cortex and medulla upon doxycycline induction. Data information: scale bars, 100 μm. In B in the upper panel, nuclei are counterstained with haematoxylin; in the lower panel, nuclei are counterstained with nuclear fast red. Proximal tubules and glomeruli are marked by red and black lines, respectively. 2 independent biological replicates (mice) of the Pax8-rtTA(+); LC1-Cre(+); LacZ(+) line and one Pax8-rtTA(-); LC1-Cre(+); LacZ(+) control mouse were examined.

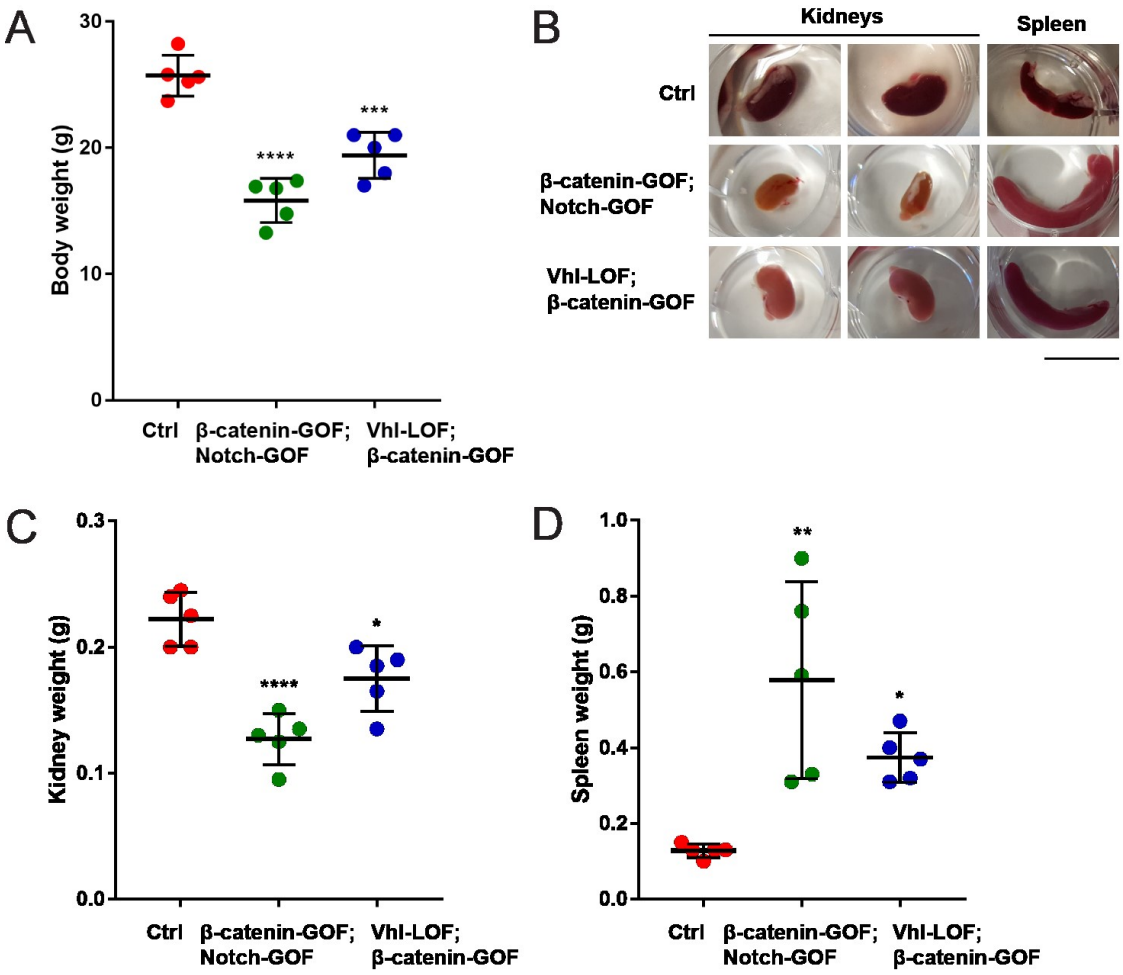

Figure 20

Macroscopic phenotypes of the β-catenin-GOF; Notch-GOF and Vhl-LOF; β-catenin-GOF mutant mice. (A) Body weight of the mutant mice versus control mice. (B) Representative kidneys and spleens from the mutant mice versus control mice. (C) The weight of the kidneys from the mutant mice versus control mice. (D) The weight of the spleens from the mutant mice versus control mice. Data information: scale bar in B, 1 cm. In A, 5 independent biological replicates (mice, dots) per line were examined; in B, 20 independent biological replicates (mice) per line were examined; in C, 5 independent biological replicates (mice, dots) in technical duplicates (kidneys) per line were examined; in D, 5 independent biological replicates (mice, dots) per line were examined. In A/C/D, graphs depict means ± SD (error bars). Data passed the Shapiro-Wilk normality test (α = 0.05). The ordinary one-way ANOVA followed by the Dunnett's multiple comparison to control mice was performed; P-values from the left to the right in A; 0.0001, 0.0002; ****$p < 0.0001$, ***$p < 0.001$; in C, 0.0001, 0.0119; ****$p < 0.0001$, *$p < 0.05$; in D, 0.0012, 0.0495; *$p < 0.01$, *$p < 0.05$.

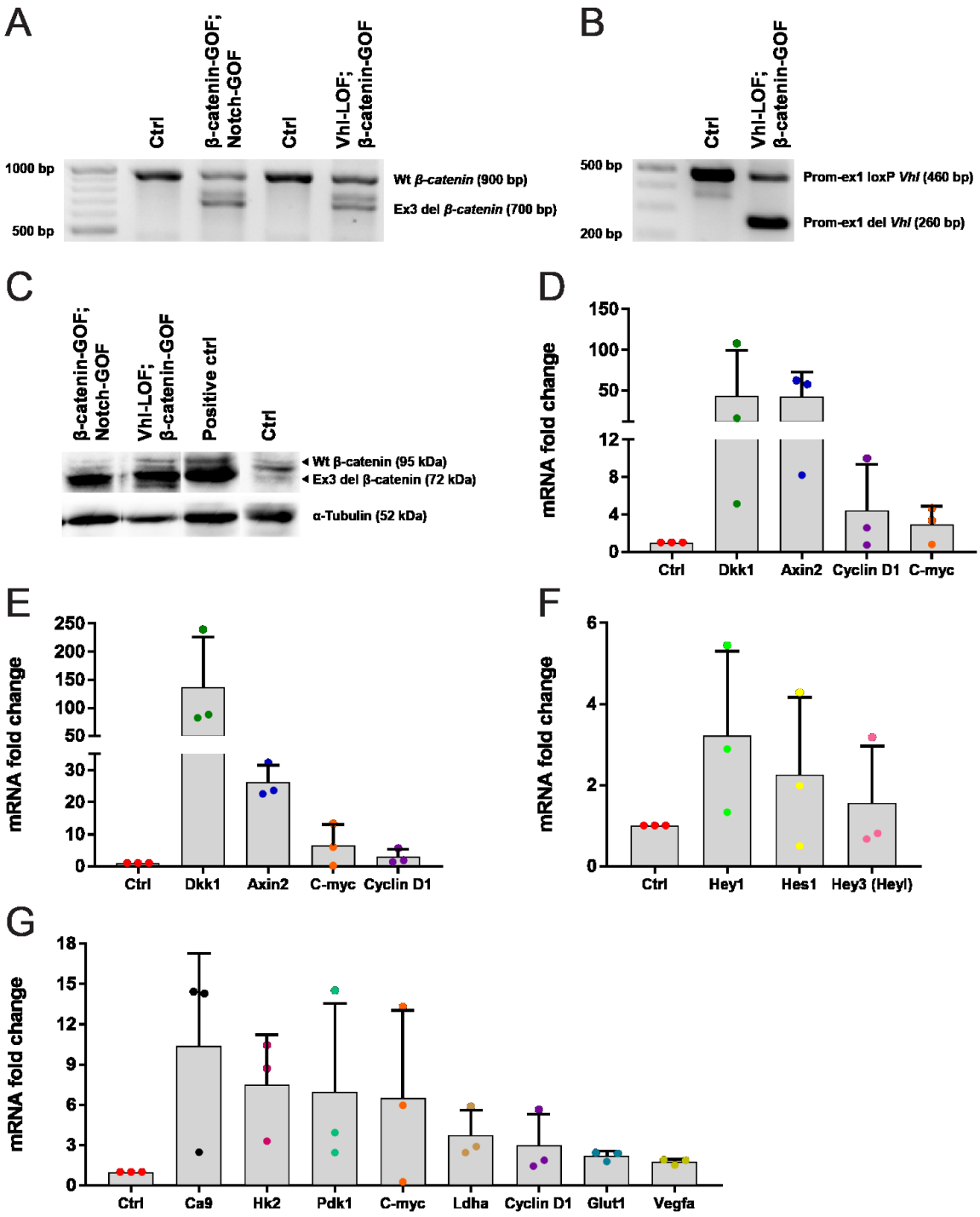

Figure 21

β-catenin, Notch and Vhl mutagenesis in the β-catenin-GOF; Notch-GOF and Vhl-LOF; β-catenin-GOF kidneys. (A) PCR-amplified fragment of the *β-catenin* gene with loxP-flanked exon 3. Two products were visible in the representative mutant kidneys: the recombined (700 bp) and wild-type (wt) (900 bp) allele. Amplification of the unrecombined loxP allele in one reaction was impossible. (B) PCR-amplified fragment of the *Vhl* gene with the loxP-flanked promoter-exon 1 sequence. Two products were visible in the representative mutant kidney: the recombined (260 bp) and unrecombined loxP (460 bp) allele. (C) Immunoblotting for the recombined (72 kDa) and wt (95 kDa) β-catenin protein in the representative mutant kidneys. (D) Fold change in normalized relative expression of selected classical β-catenin target genes in the

β-catenin-GOF; Notch-GOF mutant kidneys versus control kidneys. (E) Fold change in normalized relative expression of selected classical β-catenin target genes in the Vhl-LOF; β-catenin-GOF mutant kidneys versus control kidneys. (F) Fold change in normalized relative expression of selected classical Notch target genes in the β-catenin-GOF; Notch-GOF mutant kidneys versus control kidneys. (G) Fold change in normalized relative expression of selected classical HIF-1α/2α target genes in the Vhl-LOF; β-catenin-GOF mutant kidneys versus control kidneys. Data information: abbreviations in A-C; wt, wild-type; ex3 del, exon 3 deletion; prom-ex1 loxP/del, promoter-exon 1 loxP/deletion. The positive control used in C, a protein lysate from mouse mammary gland tumors with the mutant ex3 del β-catenin. In A-C, 3 independent biological replicates (mice) per line were examined; in D-G, 3 independent biological replicates (mice, dots) in technical triplicates were examined. In D-G, graphs depict means + SD (error bars). No statistical test was performed because of the high inter-mouse variance. However, clear increase trends were seen.

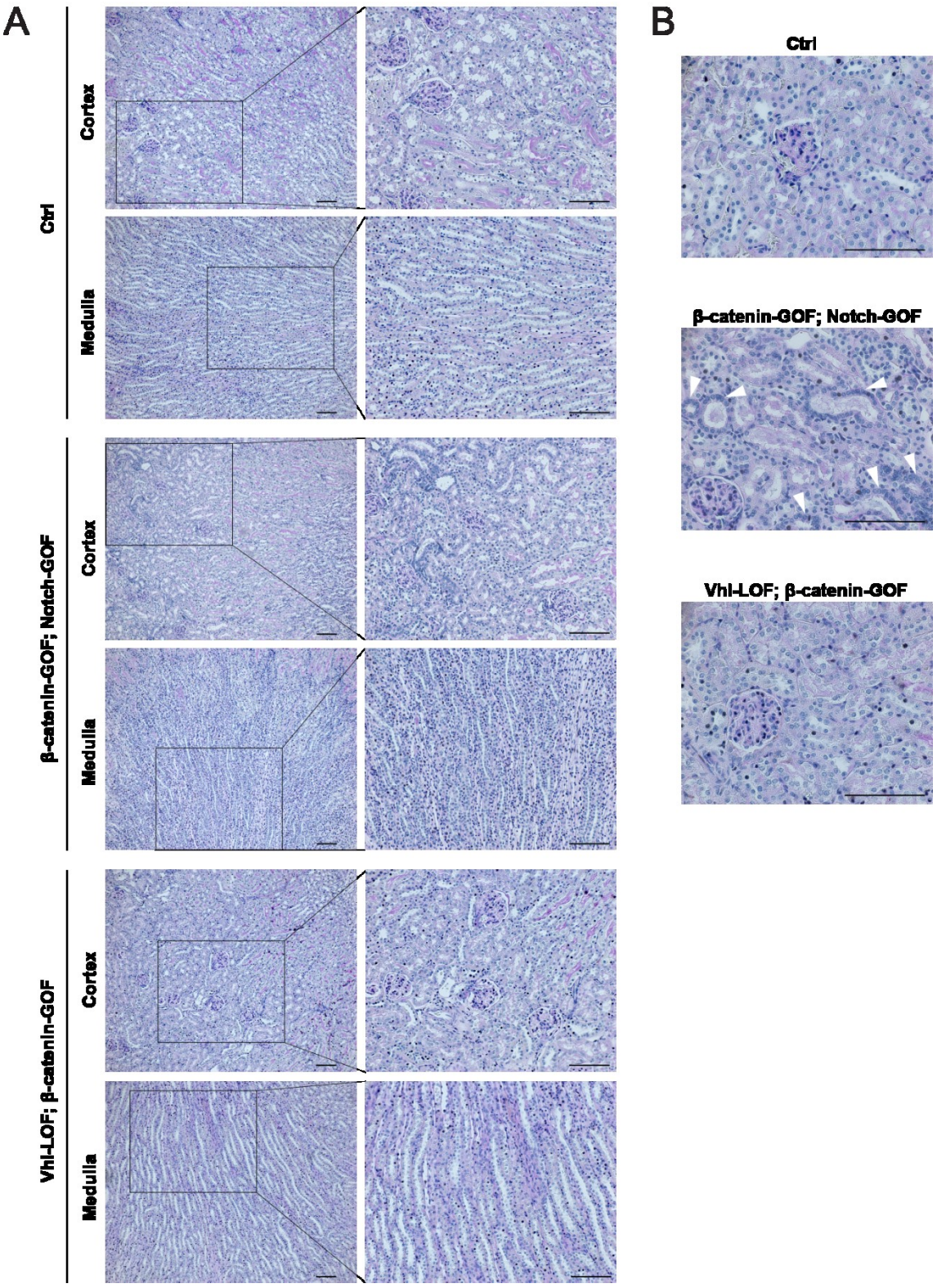

Figure 22

No tumorigenesis in the β-catenin-GOF; Notch-GOF and Vhl-LOF; β-catenin-GOF mutant kidneys. (A) Representative PAS staining in the β-catenin-GOF; Notch-GOF and Vhl-LOF; β-catenin-GOF mutant kidneys (cortex and medulla) versus control kidneys (cortex and medulla). (B) Representative PAS-stained outer part of the cortex in the mutant and control kidneys with a nuclear crowding (arrowheads) in some tubules in the β-catenin-GOF; Notch-GOF, but not in the Vhl-LOF; β-catenin-GOF mutants. Data information:

mutant kidneys after 8 months from doxycycline induction are shown. Scale bars, 100 μm. Nuclei are counterstained with haematoxylin. In A, insets are enlarged on the right. 20 independent biological replicates (all mice induced) per line were examined.

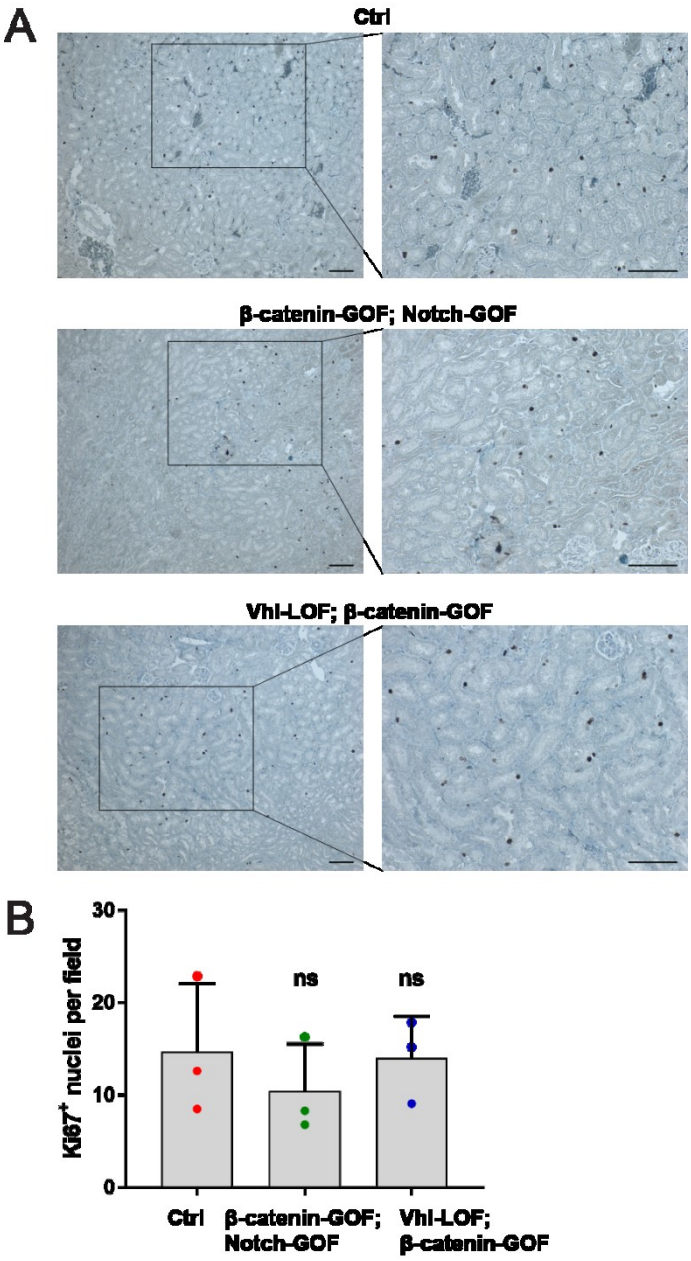

Figure 23

No higher cell proliferation rates in the β-catenin-GOF; Notch-GOF and Vhl-LOF; β-catenin-GOF mutant kidneys. (A) Representative immunohistochemistry for nuclear Ki67 in the β-catenin-GOF; Notch-GOF and Vhl-LOF; β-catenin-GOF mutant cortical kidneys versus control cortical kidneys. (B) Quantification of Ki67-positive nuclei in the β-catenin-GOF; Notch-GOF and Vhl-LOF; β-catenin-GOF mutant cortical kidneys versus control cortical kidneys. Data information: in A, mutant kidneys after 8 months from doxycycline induction are shown. Scale bars, 100 μm. Nuclei are counterstained with haematoxylin. Insets are enlarged on the right. In A, 20 independent biological replicates (all mice induced) per line were examined; in B, 3 independent biological replicates (mice, dots) with 10 technical replicates (fields per kidney) each per line were examined. In B, graphs depict means + SD (error bars). Data passed the Shapiro-Wilk normality test (α = 0.05). The ordinary one-way ANOVA followed by the Dunnett's multiple comparison to control mice was performed; P-values from the left to the right, 0.6019, 0.9871; ns: non-significant.

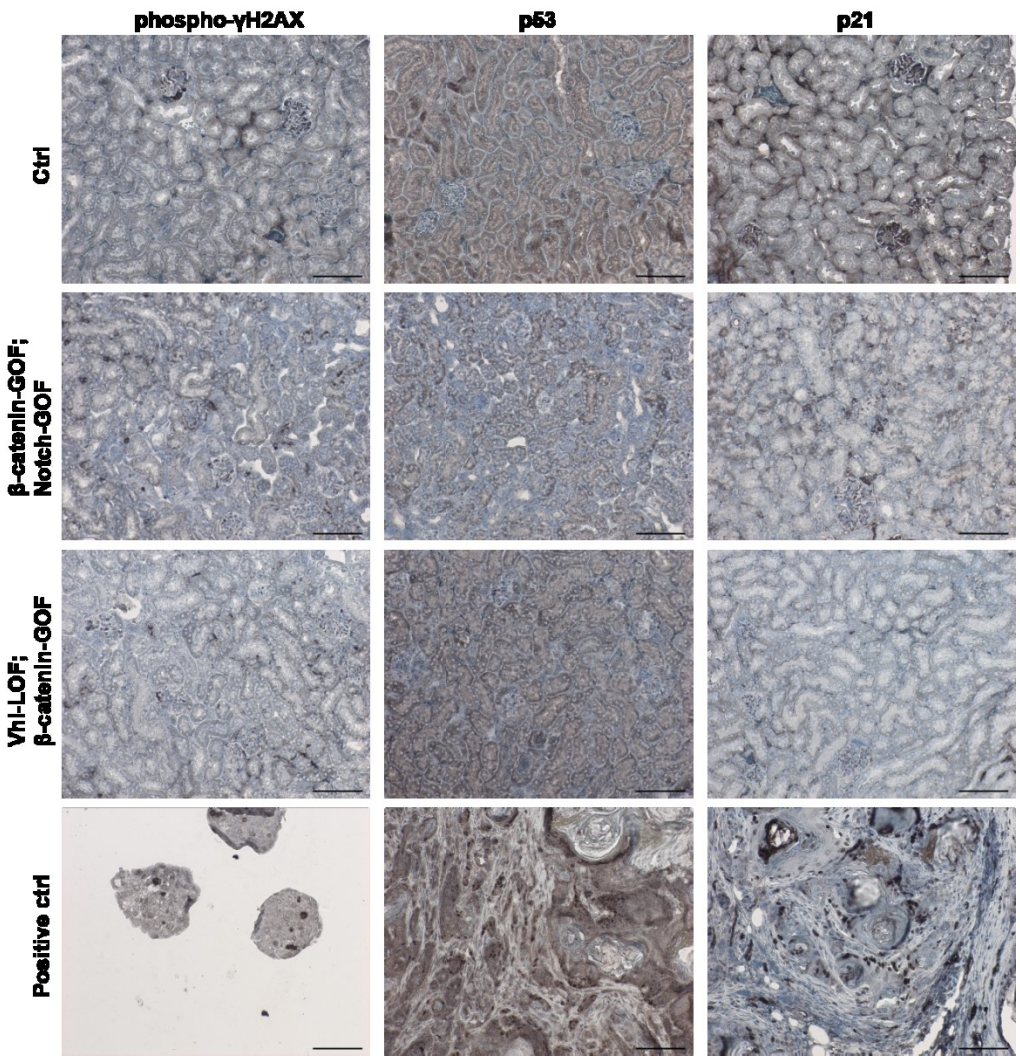

Figure 24

No DNA damage and p53- or p21-dependent growth arrest or senescence in the β-catenin-GOF; Notch-GOF and Vhl-LOF; β-catenin-GOF mutant kidneys. Representative immunohistochemistry for nuclear phospho-γH2AX (left panel), p53 (middle panel) and p21 (right panel) in the β-catenin-GOF; Notch-GOF and Vhl-LOF; β-catenin-GOF mutant cortical kidneys versus control cortical kidneys. Data information: the positive controls used; in the left panel, non-adherent spheres derived from the human colorectal carcinoma cell line LS174T with doxycycline-induced shRNA-mediated knockdown of *MLL1*; in the middle and right panel, mouse Pi3k-GOF; β-catenin-GOF; p53-GOF mammary gland tumors. Scale bars, 100 μm. Nuclei are counterstained with haematoxylin. 3 independent biological replicates (mice) per line were examined.

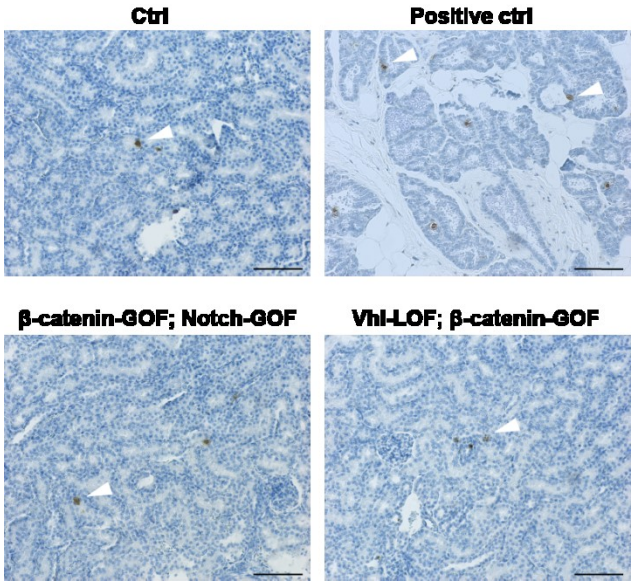

Figure 25

No increased apoptosis in the β-catenin-GOF; Notch-GOF and Vhl-LOF; β-catenin-GOF mutant kidneys. Representative immunohistochemistry for the blunt ends of double-stranded DNA breaks in apoptotic cells (TUNEL assay) in the β-catenin-GOF; Notch-GOF and Vhl-LOF; β-catenin-GOF mutant cortical kidneys versus control cortical kidneys. Positive nuclei are marked by the arrowheads. Data information: the positive control used (included in the kit), a normal rat mammary gland 3-5 days after weaning of pups. Scale bars, 100 μm. Nuclei are counterstained with haematoxylin. 3 independent biological replicates (mice) per line were examined.

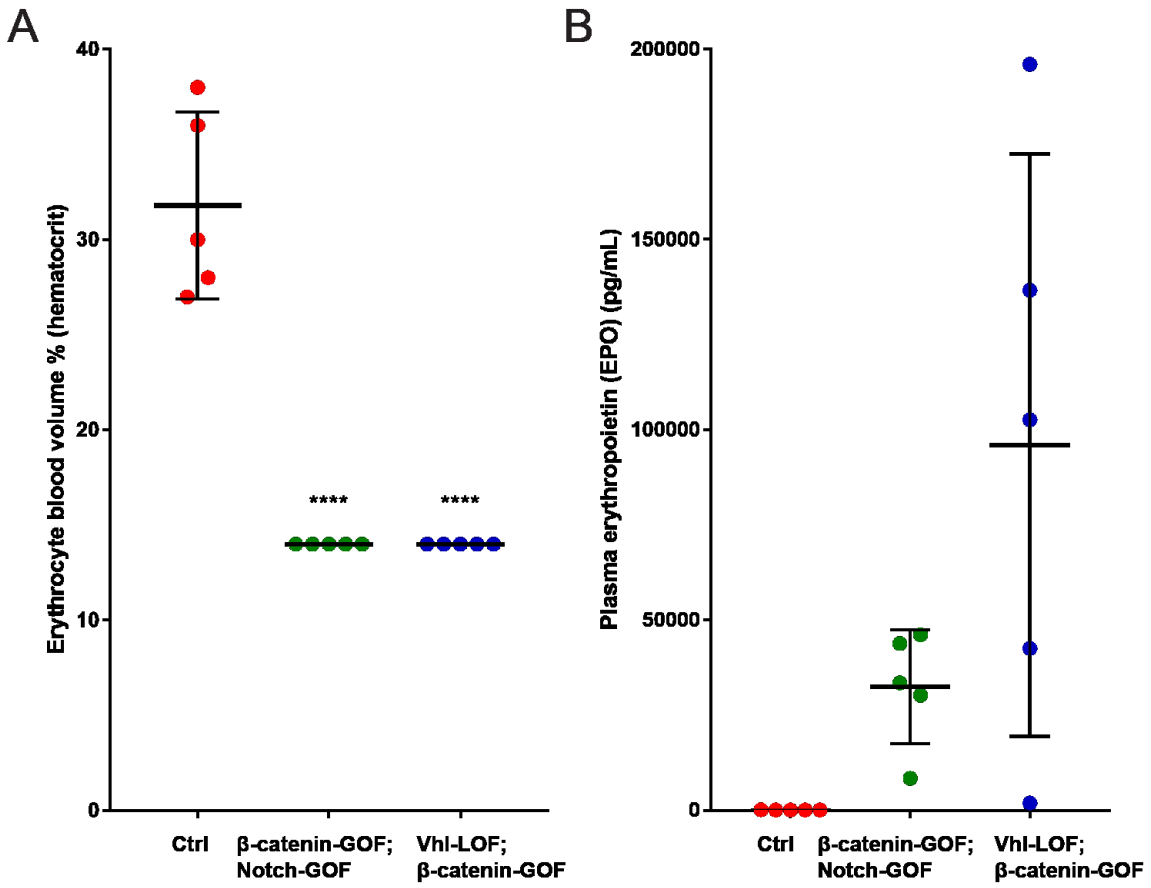

Figure 26

Anemia in the β-catenin-GOF; Notch-GOF and Vhl-LOF; β-catenin-GOF mutant mice not associated with impaired erythropoietin (EPO) production. (A) Blood volume percentages of erythrocytes (hematocrit) in the mutant mice versus control mice. (B) Concentrations of plasma EPO in the mutant mice versus control mice. Data information: in A, 5 independent biological replicates (mice, dots) with one technical replicate each per line were examined; in B, 5 independent biological replicates (mice, dots) in technical triplicates per line were examined. In A and B, graphs depict means ± SD (error bars). In A, data passed the Shapiro-Wilk normality test (α = 0.05). The ordinary one-way ANOVA followed by the Dunnett's multiple comparison to control mice was performed; P-values from the left to the right, 0.0001, 0.0001; ****$p < 0.0001$. In B, no statistical test was performed because of the high inter-mouse variance. However, dramatic increase trends were seen.

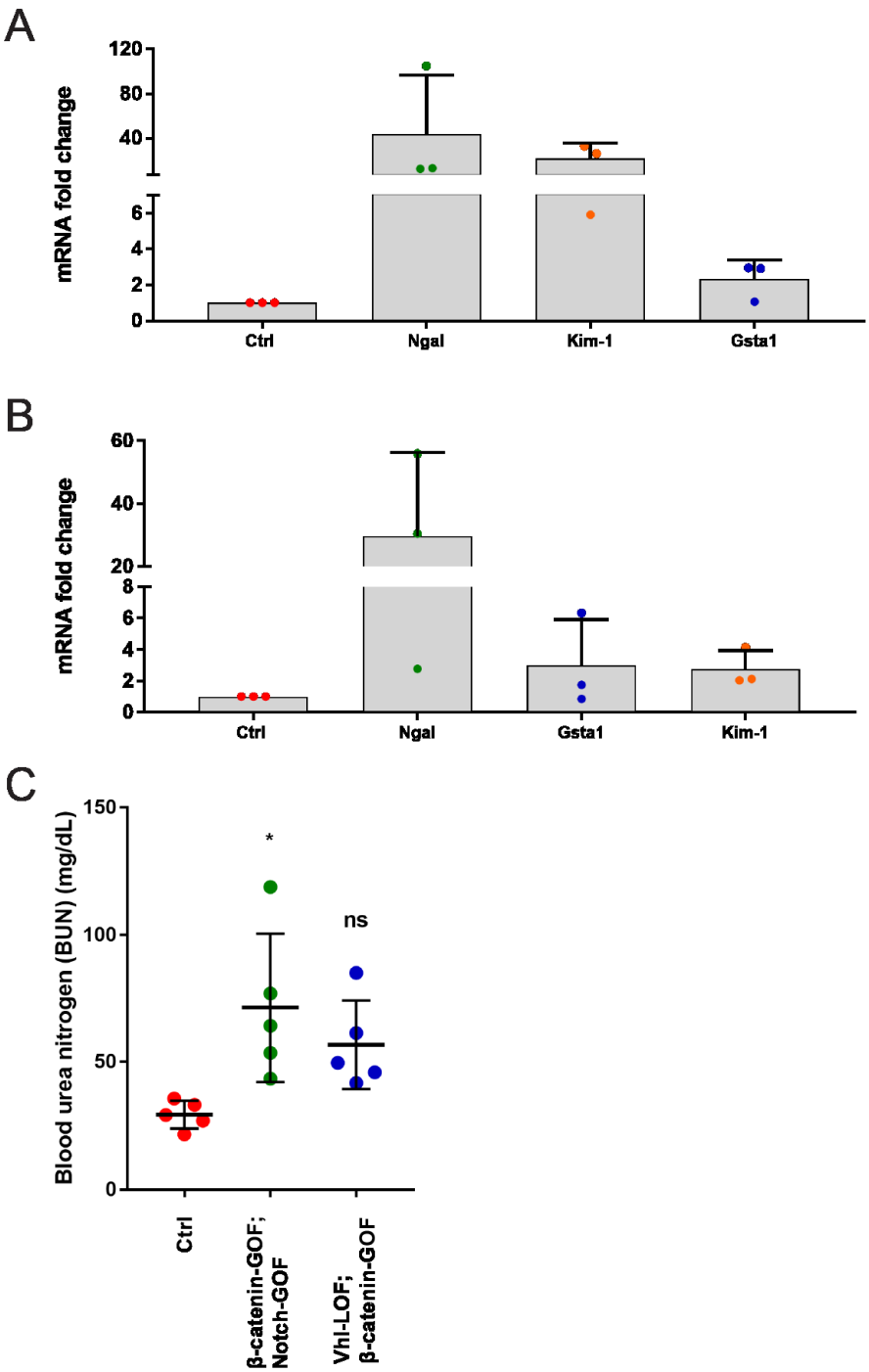

Figure 27

Kidney injury and failure in the β-catenin-GOF; Notch-GOF and Vhl-LOF; β-catenin-GOF mutant mice. (A) Fold change in normalized relative gene expression of selected kidney injury markers in the β-catenin-GOF; Notch-GOF mutant kidneys versus control kidneys. (B) Fold change in normalized relative gene expression of selected kidney injury markers in the Vhl-LOF; β-catenin-GOF mutant kidneys versus control kidneys. (C) Concentrations of blood urea nitrogen (BUN) in the mutant mice versus control mice. Data information: in A and B, 3 independent biological replicates (mice, dots) in technical triplicates were examined; in C, 5 independent biological replicates (mice, dots) with one technical replicate each per line were examined. In A and B, graphs depict means + SD (error bars); in C, graphs depict means ± SD (error bars). In A and B, no statistical test was performed because of the high inter-mouse variance. However,

clear increase trends were seen. In C, data passed the Shapiro-Wilk normality test ($\alpha = 0.05$). The ordinary one-way ANOVA followed by the Dunnett's multiple comparison to control mice was performed; P-values from the left to the right, 0.0109, 0.0888; *$p < 0.05$, ns: non-significant. Although the difference in average concentration of BUN between the Vhl-LOF; β-catenin-GOF mutant mice and control mice was non-significant ($p < 0.05$), a clear increase trend was seen. The increase in n might be an option to increase statistical significance.

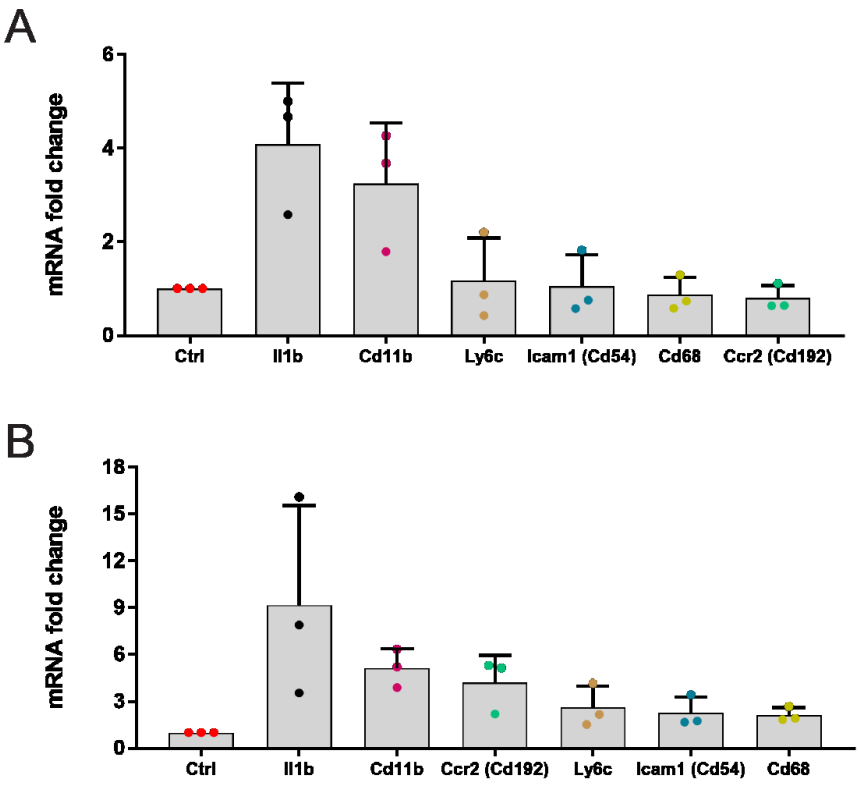

Figure 28

Kidney inflammation in the β-catenin-GOF; Notch-GOF and Vhl-LOF; β-catenin-GOF mutant mice. (A) Fold change in normalized relative gene expression of selected inflammation markers in the β-catenin-GOF; Notch-GOF mutant kidneys versus control kidneys. (B) Fold change in normalized relative gene expression of selected inflammation markers in the Vhl-LOF; β-catenin-GOF mutant kidneys versus control kidneys. Data information: 3 independent biological replicates (mice, dots) in technical triplicates were examined. Graphs depict means + SD (error bars). No statistical test was performed because of the high inter-mouse variance. However, clear increase trends were seen for all genes in B and for *Il1b* and *Cd11b* in A.

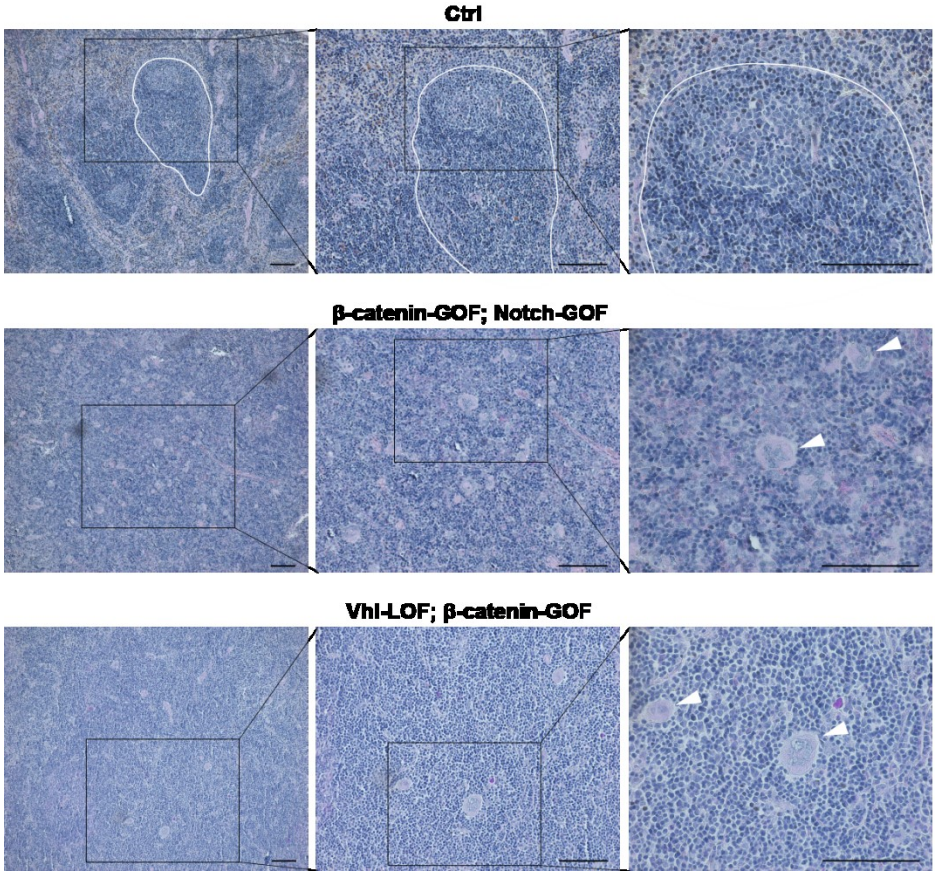

Figure 29

Extramedullary hematopoiesis in the spleens from the β-catenin-GOF; Notch-GOF and Vhl-LOF; β-catenin-GOF mutant mice. Representative PAS staining showing extramedullary hematopoiesis in the spleens from the β-catenin-GOF; Notch-GOF and Vhl-LOF; β-catenin-GOF mutant mice versus control mice. Megakaryocytes are marked by the arrowheads. Data information: scale bars, 100 μm. Nuclei are counterstained with haematoxylin. An undisrupted follicular B-cell compartment in the white pulp in control mice is marked by white lines. Insets are enlarged on the right. 3 independent biological replicates (mice) per line were examined.

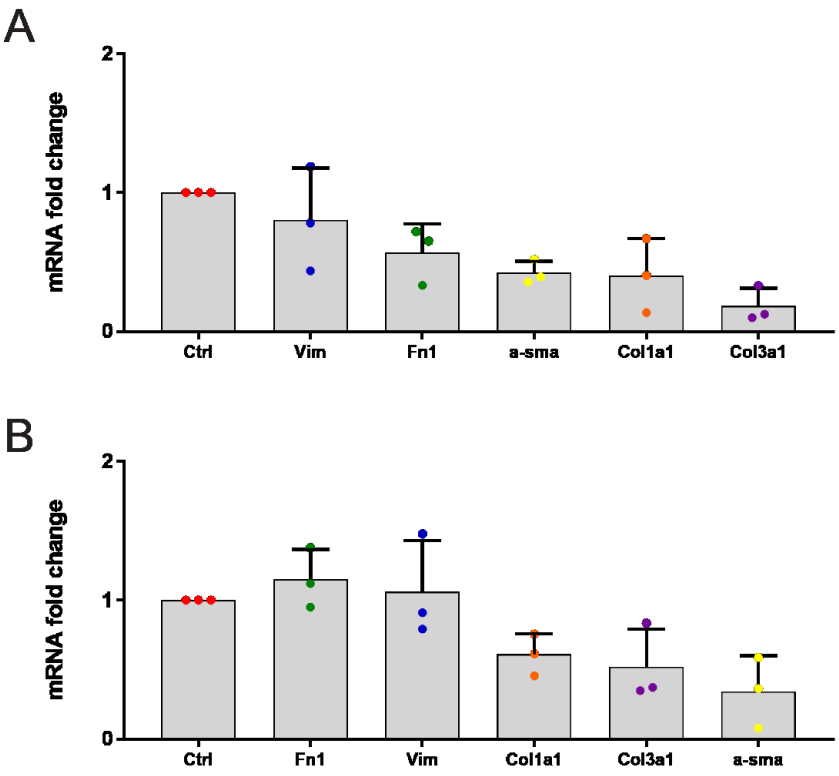

Figure 30

No fibrosis in the β-catenin-GOF; Notch-GOF and Vhl-LOF; β-catenin-GOF mutant kidneys. (A) Fold change in normalized relative gene expression of selected fibrotic markers of myofibroblasts and extracellular matrix in the β-catenin-GOF; Notch-GOF mutant kidneys versus control kidneys. (B) Fold change in normalized relative gene expression of selected fibrotic markers of myofibroblasts and extracellular matrix in the Vhl-LOF; β-catenin-GOF mutant kidneys versus control kidneys. Data information: 3 independent biological replicates (mice, dots) in technical triplicates were examined. Graphs depict means + SD (error bars). No statistical test was performed because of the high inter-mouse variance. However, no increase trends were seen.

Discussion

During my Ph.D. research phase, I completed two projects, which aimed to study i) properties of normal stem or progenitor cells in renewal and repair of the adult tubular epithelia and ii) malignant stem cells that produce kidney tumors. In the first project, I have generated and characterized a long-term 3D tubuloid model from adult mouse kidney cells. In the second project, I have established genetic mouse models to investigate the role of CSC-associated Wnt and Notch signaling in ccRCC development.

A long-term 3D tubuloid model of the adult mouse kidney

Adequate characterizations of adult mouse kidney tubuloids have not been achieved to my satisfaction. To study components and signaling systems of the tubuloids, I therefore performed bulk proteomic and phosphoproteomic analyses in collaboration with experts, Philipp Mertins, group leader at the MDC and Berlin Institute of Health (BIH), and his colleagues. For the first time in kidney organoid research, we examined the tubuloids in comparison to the adult kidney epithelia by global gene expression at the functional levels, as opposed to RNA sequencing. In line with the discovery that the tubuloids contain self-renewing cells and can be expanded in long-terms, the phospho-proteome revealed the coexistence of stem or progenitor cells and of differentiated cells of several nephron segments. As the protein and phosphorylation levels could be maintained over long-term passages, I conclude that my protocol produces stable tubuloids, which are driven by the balance of stem or progenitor cells and of differentiated cells. However, despite a high coverage of the coding genome, we were not able to detect important proteins such as collecting duct-specific Aquaporin 3, which are present in the tubuloids. To characterize the tubuloids more thoroughly, single cell RNA sequencing should be performed, which so far was carried out only on human adult tubuloids (Schutgens *et al*, 2019) and iPSC-derived organoids (Uchimura *et al*, 2020; Wu *et al*, 2018). In the future, single cell proteomics will improve the global analyses of the protein levels in individual tubuloid cells (Marx, 2019).

My findings address important questions on the presence and nature of cells with stemness characteristics in the adult kidney. The data suggest the existence in clonally grown tubuloids of stem or progenitor cells with the capacity for multi-lineage differentiation into proximal tubule and distal nephron cells. One previous study identified a population of multipotent progenitor cells in the adult mouse kidney (Kang *et al*, 2016), while others argued for the functional importance of unipotent progenitors (Kumar *et al*, 2015; Rinkevich *et al*, 2014; Schutgens *et al*, 2017) or for the concept of plastic

dedifferentiation upon injury (Kusaba *et al*, 2014). Studies in adult human kidney organoids and tubuloids were not conclusive regarding these issues (Grassi *et al*, 2019; Schutgens *et al*, 2019). The upregulation of stem cell-associated Wnt, Notch and Yap signaling further indicates the recapitulation of kidney repair response in the tubuloids, similar to mice upon kidney injury (Chen *et al*, 2013, 2018; Kang *et al*, 2016; Lin *et al*, 2010; Rinkevich *et al*, 2014; Zhou *et al*, 2012). However, the controversial presence of resident stem or progenitor cell populations involved in homeostatic maintenance and repair of the adult kidney and the complex architecture of the organ complicate further development and characterization of my tubuloids. Lack of defined markers of kidney stem or progenitor cells limits the efficiency of tubuloid formation from single cells, as seen by relatively low numbers of the tubuloids in comparison to the numbers of seeded cells.

I established the tubuloids from single epithelial cells from whole adult mouse kidneys. Other groups also used single cells isolated from whole human and mouse kidneys to generate organoid and tubuloid cultures (Grassi *et al*, 2019; Rinkevich *et al*, 2014). Studying self-renewal, differentiation and self-organization of stem or progenitor cells on the 3D level appears reasonable, when it starts from single cells (Lancaster & Knoblich, 2014; Sato *et al*, 2009). In addition, it is crucial to use whole kidney cells for the unbiased representation of the renal epithelia in organoid cultures, because clear distinction of organoids derived from either cortical or medullary parts of the human kidney was seen by bulk RNA sequencing (Grassi *et al*, 2019). In contrast, another group took whole kidney fragments for preparing mouse tubuloids and cortical kidney fragments for preparing human tubuloids (Schutgens *et al*, 2019).

In the tubuloids, I detected differentiated proximal tubular cells and cells of the distal nephrons, while podocytes, parietal glomerular cells and Loop of Henle cells were missing. Other mouse tubuloids exhibited markers of the same nephron segments (Rinkevich *et al*, 2014). Human tubuloid cultures contained proximal tubule and collecting duct cells. Upon growth factor withdrawal, small proportions of distal tubule and Loop of Henle cells were generated (Schutgens *et al*, 2019). The occurrence of podocytes, proximal tubule cells and collecting duct cells was reported in other human organoids using different culturing conditions (Grassi *et al*, 2019). My tubuloids displayed the exclusive presence of epithelial cells, similar to other mouse and human tubuloids (Rinkevich *et al*, 2014; Schutgens *et al*, 2019) and consistent with organoids derived from various adult organs (Schutgens & Clevers, 2020).

I used the tubuloids to study crucial signaling systems, which are involved in self-renewal and differentiation of the adult tubular epithelia. In future studies, my tubuloids will assist in the identification and enrichment of kidney stem or progenitor cells and in the functional analysis of their maintenance and differentiation, and thus will serve as models to investigate mechanisms of homeostasis and regeneration of the adult tubular epithelia. This knowledge will enable to develop improved protocols for creating tubuloid cultures, which represent the full cellular diversity of the adult tubular epithelia. In addition, co-cultures with endothelial, stromal and immune cells will further advance the quality of tubuloid cultures (Schutgens & Clevers, 2020).

My mouse-derived tubuloids also exhibit substantial advantages for translational kidney cancer research. The tubuloids are enriched in proximal tubular cells, which are the cells of ccRCC origin. Therefore, these systems may be used to model ccRCC tumorigenesis. Establishing genetic mouse models allows to introduce a limited number of mutational events at once. The tubuloids may enable to study simultaneous or sequential genetic interferences at multiple loci and their functional effects on *in vitro* dynamics and malignant transformation of proximal tubular epithelial cells in a defined genetic background using the CRISPR/Cas9-based knockout and knockin techniques (Hendriks *et al*, 2021). Therefore, mutant mouse tubuloid systems may become a valuable *in vitro* complement to genetic mouse models of ccRCC (Bailey *et al*, 2017; Espana-Agusti *et al*, 2017; Harlander *et al*, 2017) and to patient-derived tumor organoids (Bolck *et al*, 2021; Calandrini *et al*, 2020; Fendler, Myszczyszyn *et al*, 2020; Grassi *et al*, 2019; Schutgens *et al*, 2019). Genetic cancer systems of the tubuloids may be utilized to identify further driver-specific druggable targets. Nephrotoxicity is the main dose-limiting side effect of cisplatin and other chemotherapeutics in cancer patients (Malyszko *et al*, 2020). Thus, predicting nephrotoxicity during preclinical development of further drugs is essential, and the data support the usefulness of my tubuloids as a platform for nephrotoxicity testing. Generating genetic cancer models from normal mouse tubuloids provides the opportunity to develop less nephrotoxic drugs by screening for compounds, which selectively remove transformed cells, while sparing matched healthy cells.

Genetic mouse models with β-catenin-GOF, Notch-GOF and Vhl-LOF to study kidney tumorigenesis

Using genetic mouse models, I aimed to mimick kidney tumorigenesis by the interplay of the upregulation of Wnt and Notch signaling or by the interaction of Wnt hyperactivation and Vhl deficiency. Despite the rational hypothesis on the involvement of Wnt-high and Notch-high CSCs in ccRCC development as well as targeting adult tubular epithelial cells using a well-designed genetic system, the mouse mutants did not produce kidney tumors. Unexpectedly, the mice displayed fatal phenotypes, which partly resembled CKD.

To establish genetic mouse models of ccRCC, I took advantage of an inducible stringent Cre system, which enabled targeted mutagenesis only in adult kidney epithelial cells, and thus circumvented the occurrence of cysts and other embryonic or postnatal defects. Several groups utilized the same approach (Bailey *et al*, 2017; Espana-Agusti *et al*, 2016, 2017; Harlander *et al*, 2017; Mathia *et al*, 2013). The Pax8-rtTA-based system drives Cre-mediated recombination specifically and efficiently in Pax8-expressing adult kidney epithelial cells, including proximal tubular cells. These cells are the presumable cells of ccRCC origin, according to histopathological (Lindgren *et al*, 2018) and transcriptomic data (Büttner *et al*, 2015; Chen *et al*, 2016a; Lindgren *et al*, 2017; Young *et al*, 2018) and to results on mice (Harlander *et al*, 2017). However, one study provided several lines of controversial evidence, which suggest that Pax8-positive parietal glomerular epithelial cells are the cells of ccRCC origin. In this study, Cre was expressed under direct control of the Pax8 promoter also in parietal glomerular epithelial cells (Gu *et al*, 2017; Leung & Kim, 2017), which was not the case in my Pax8-rtTA-driven model and in another model using the Pax8-CreERT2 system (Espana-Agusti *et al*, 2016, 2017). Though, the latter group succeeded in establishing kidney tumors from Pax8-expressing cells outside of the Bowman's capsule (Espana-Agusti *et al*, 2017). Moreover, even if kidney tumors that share the same driver mutations develop under different Cre systems, they may not exhibit the same penetrance and molecular features due to non-overlapping cells of origin. For instance, combined inactivation of Vhl and Pbrm1 resulted in low-penetrant tumors with hyperactive mTOR in one study (Nargund *et al*, 2017) and in tumors with higher penetrance and lower mTOR levels in another one (Gu *et al*, 2017). It should be noted that transcriptional context of a self-renewing cell of origin, i.e. a precursor of a CSC, is a strong determinant of tumorigenesis (Lindgren *et al*, 2018; Lytle *et al*, 2018). Human kidney CSCs display the activation of Wnt and Notch, similar to normal tubular progenitor cells in mice (Kang *et al*, 2016; Rinkevich *et al*, 2014)

and to the mouse-derived tubuloids described here. This suggests that Wnt-high and Notch-high cells with stemness characteristics in the proximal tubular segment might be susceptible to tumorigenesis upon the dysregulation of both signaling systems. I detected neither p53-, p21- or p16-positive senescent cells nor apoptotic cells in the mutant kidneys. Senescence is a potent tumor-suppressive mechanism, which prevents transformation and expansion of cells with oncogene activation or tumor suppressor gene loss and must be overcome in a given tissue context by a proper combination of driver genomic hits to induce tumorigenesis (Sturmlechner *et al*, 2017). For example, Apc inactivation in mouse kidneys led to spontaneous non-apoptotic deletion of the majority of mutant cells and senescence of surviving Apc-deficient cells in a p53- or p21-dependent manner, despite high efficiency of recombination. Deletion of Apc together with p53 or p21 bypassed senescence and initiated tumor development (Cole *et al*, 2010; Sansom *et al*, 2005). In line with this, oncogenic K-ras accelerated tumor growth primed by Apc deficiency in mouse kidneys (Sansom *et al*, 2006). Furthermore, concomitant inactivation of Pbrm1 was sufficient to escape from Vhl loss-driven p21-mediated senescence in mouse kidneys (Espana-Agusti *et al*, 2017). Two other models of cooperative Vhl-Pbrm1 deletion were also established (Gu *et al*, 2017; Nargund *et al*, 2017). In addition, transformation of Vhl-defective cells in three other systems was boosted by either the inactivation of Bap1 (Gu *et al*, 2017), combined loss of p53 and Rb1 (Harlander *et al*, 2017) or cooperative alterations of Cdkn2a (p16) and Myc (Bailey *et al*, 2017). Alternatively, p53-independent p27/Rb-driven senescence upon p400 reduction might be the mechanism behind inhibition of kidney oncogenesis in my models (Young *et al*, 2008).

The mutant mice exhibited hallmarks of CKD. The functional role of Notch signaling in the development of CKD in the adult kidney was revealed in a mouse model. For this purpose, the authors utilized a different Pax-rtTA system, which directly overactivates N1icd without Cre induction. Mutant kidneys displayed pronounced tubular degeneration and dilation as well as tubulointerstitial inflammation and fibrosis (Bielesz *et al*, 2010). Lack of fibrosis in my models might suggest that the mutant mice have not yet progressed to end-stage CKD, but this issue remains unresolved. However, adult mice with combined upregulation of Notch signaling and Vhl inactivation in two other studies developed tumor precursor lesions without the signs of CKD (Bhagat *et al*, 2017; Johansson *et al*, 2016). In concordance with my study, exon 3 deletion-mediated β-catenin-GOF in the tubules of adult mouse kidneys using a different Cre system in another model contributed to renal failure, tubular and glomerular damage and tubulointerstitial inflammation, but not to fibrosis (Wong *et al*, 2018).

Doxycycline induction resulted in high levels of recombination in the mutant kidneys. In one study, genetic upregulation of Yap signaling in proximal tubular cells in adult mice using high doses of tamoxifen led to death of animals by kidney dysfunction and tubulointerstitial inflammation and fibrosis. Remarkably, low mosaic injection of tamoxifen prevented the CKD phenotypes and enabled tumor development (McNeill *et al*, 2019, unpublished data, AACR Conference *The Hippo Pathway: Signaling, Cancer, and Beyond*, San Diego). These findings suggest that focal, instead of broad, recombination in adult kidney epithelial cells through decreased doses of doxycycline might support tumor development in my models by overcoming severe non-neoplastic phenotypes.

Materials and methods

Mice

The Landesamt für Gesundheit und Soziales (LaGeSo) in Berlin approved my mouse studies (G0342/13). Mice were housed and bred in the IVC cages type II at 21°C ambient temperature, at 50-60% humidity, in a 12-h dark/light cycle and in pathogen-free conditions. LC1-Cre mice (Schönig *et al*, 2002) were a kind gift from Klaus Rajewsky (MDC). β-catenin-loxP (Harada *et al*, 1999), Notch-loxP (Murtaugh *et al*, 2003) and LacZ-loxP (Soriano, 1999) mice came from our in-house colonies. Pax8-rtTA B6.Cg-Tg(Pax8-rtTA2S*M2)1Koes/J (Traykova-Brauch *et al*, 2008) and Vhl-loxP B6.129S4(C)-Vhltm1Jae/J (Haase *et al*, 2001) mice were purchased from the Jackson Laboratory. The studies in the tubuloids and genetic mouse models were performed using both male and female mice of a mixed C57BL/6J and FVB/NJ background, unless otherwise stated. To establish the genetic mouse models, adult one-month-old Pax8-rtTA-LC1-Cre-loxP mice and control mice carrying loxP alleles, but no Pax8-rtTA or LC1-Cre (both males and females) were exposed for 5 days to doxycycline (Sigma-Aldrich) at the concentration of 0.2 mg/ml in drinking water supplemented with 5% sucrose. According to the score sheet, mice were checked at least twice per week until illness symptoms were observed. Sick mice were immediately sacrificed and biological material was collected. In the subsequent experiments, material from mice withdrawn after 4 months from doxycycline induction was used, unless otherwise stated.

Preparation of kidney cell suspensions

Kidneys were harvested and transferred to MEM with Earle's Salts (with 2.2 g/l $NaHCO_3$, without L-Glutamine) medium (Biochrom) supplemented with 10% FCS (Life Technologies), 1x Non-Essential Amino Acids (NEAA) (Thermo Fisher Scientific), 2 mM L-Glutamine (Biochrom), 1x Penicillin-Streptomycin (Life Technologies) and 125 µg/ml Amphotericin B (Biomol). Whole kidneys were minced into pieces smaller than 1 mm^3, digested in 2 mg/ml Collagenase P (Roche) for 45 min and filtered through sieves with 70 and 40 µm pore size. Erythrocytes were lysed in RBC lysis buffer and lymphocytes were depleted by MACS using CD45 microbeads (Miltenyi Biotec) according to the manufacturer's instructions.

Tubuloid cultures

Freshly isolated cell suspensions were seeded at 10^5 cells per well in 25 µl Matrigel (75%, Corning) lenses in 48-well plates. Matrigel drops were overlayed with 250 µl tubuloid medium (Table 1). Medium was changed every other day. The tubuloids were

passaged for the first time after 14 days and subsequently once per week. Matrigel lenses were mechanically broken and the tubuloids were collected and dissociated to small cell clusters using TrypLE Select (Life Technologies) for 10 min. In the first two passages, collected tubuloids were additionally filtered through a sieve with 40 µm pore size. Cultures were passaged in 1:3 ratios. If single cell suspensions were needed, the tubuloids were dissociated in TrypLE for 1 hr. Cell clusters from the tubuloids were cryopreserved at an early passage in 1 ml Recovery Cell Culture Freezing Medium (Thermo Fisher Scientific) according to the manufacturer's instructions. For experiments, 100 ng/ml human FGF10 (Peprotech), 10 µM Y-27632 dihydrochloride (Rho kinase/ROCK inhibitor) (Selleckchem), 100 ng/ml human Wnt3a (R&D Systems) or 10 ng/ml human TGFβ (Peprotech) were added. Brightfield and fluorescence images were acquired with a Leica DMI 6000 B microscope using the Leica LAS X software.

Table 1

Medium components for tubuloid culture.

Component	Function	Concentration	Supplier
Advanced DMEM/F12 with GlutaMax	Basal medium	–	Life Technologies
Penicillin-Streptomycin	Antibiotics	1x	Life Technologies
Amphotericin B	Antifungal	125 µg/ml	Biomol
HEPES	Buffer	10 mM	Life Technologies
N-acetylcysteine	Antioxidant	1.25 mM	Sigma-Aldrich
B27	Serum-free growth supplement	1x	Life Technologies
N2	Serum-free growth supplement	1x	Life Technologies
Nicotinamide	Increasing tubuloid formation and lifespan via inhibiting sirtuin activity involved in apoptosis and differentiation (Holmberg *et al*, 2017; Sato *et al*, 2011)	10 mM	Sigma-Aldrich
Human EGF	Stimulating proliferation, inhibiting apoptosis (Holmberg *et al*, 2017; Sato *et al*, 2011)	50 ng/ml	Peprotech

A83-01	Blocking differentiation and promoting long-term culture of stem cells via inhibiting TGFβ signaling (Holmberg *et al*, 2017; Sato *et al*, 2011)	500 nM	Sigma-Aldrich
Human R-spondin-1	Maintaining stem cells via agonizing Wnt signaling (Holmberg *et al*, 2017; Sato *et al*, 2011)	500 ng/ml	Peprotech
Hydrocortisone (HC)	Acting anti-inflammatory via repressing activity of NF-κB and AP-1 (Cato *et al*, 2002), inducing Yap signaling (Sorrentino *et al*, 2017)	0.5 µg/ml	Sigma-Aldrich
Prostaglandin E2 (PGE2)	Preventing anoikis and promoting stem cell survival via enhancing Wnt signaling (Holmberg *et al*, 2017)	1 µM	Sigma-Aldrich

Functional tests

BrdU (Thermo Fisher Scientific) treatment (10 µM) was performed for 4 hrs prior to tubuloid collection for staining. Endocytosis was tested by uptake of 10 µg/ml Alexa488-conjugated dextran (Thermo Fisher Scientific) for 48 hrs. Cisplatin (Cayman Chemical) treatment (100 µM) was conducted for 72 hrs prior to protein collection for immunoblotting. For FAC-sorting, dissociated tubuloid cells were stained with SYTOX Orange (1:1000, Thermo Fisher Scientific) in FACS buffer with DNase (1:100) for 20 min to label dead cells. A BD FACSAria IIu sorter and the FACSDiva 8.0.1 software (BD Biosciences) were used. A yellow-green laser (561 nm) was used for SYTOX Orange excitation. Emission was measured using a 586/15 BP filter. A UV laser (355 nm) and a 450/50 BP filter were used to exclude autofluorescence of the cells. To better visualize the cells, a bidirectional X/Y-axis scale was used. 500 sorted viable single cells (negative for SYTOX Orange) were seeded per well in 9 µl Matrigel (75%, Corning) lenses in 96-well plates and overlayed with 100 µl tubuloid medium. Medium was changed once. After 11 days, the tubuloids were collected and processed for staining. For the examination of structural changes of the tubuloids upon growth factor withdrawal or inhibitor or cisplatin treatment, single cells were seeded at 45000 cells in 48-well plates and cultured 7 days in tubuloid medium without EGF, A83-01 or R-spondin-1 or cultured 24h in normal medium and 6 days in medium containing gefitinib (Selleckchem), ICG-001 (Biochempartner) or cisplatin (Cayman Chemical) at the IC50 concentration.

Proteomics and phosphoproteomics

Three independent biological replicates of early (TEP) and long-term (TLP) passage tubuloids were released from Matrigel by mechanical disruption, collected in a conical tube and incubated with the non-enzymatic Cell Recovery Solution (Corning) according to the manufacturer's instructions to remove Matrigel residues. Three independent biological replicates of Epcam-positive kidney epithelial cells (CK) were MAC-sorted from freshly isolated single cell suspensions from whole mouse kidneys. Global proteomic and phosphoproteomic characterization of the samples was achieved by the tandem mass tag (TMT)-based quantitation using the TMT 10-plex reagents (Thermo Fisher Scientific), as previously described (Mertins *et al*, 2018). Briefly, samples were lysed in urea lysis buffer containing protease and phosphatase inhibitors, subjected to tryptic in-solution digest and labeled with the TMT 10-plex reagents. After pooling, samples were separated into 24 fractions for the proteomic and 12 fractions for the phosphoproteomic analysis using basic reversed-phase HPLC. Phosphopeptides were enriched from each fraction using robot-assisted iron-based IMAC on an AssayMap Bravo system (Agilent). Proteomic and phosphoproteomic samples were measured on a Q Exactive HF-X orbitrap mass spectrometer (Thermo Fisher Scientific) connected to an EASY-nLC system (Thermo Fisher Scientific) applying a 110-min online HPLC gradient. MS acquisition was performed at a resolution of 60000 in a scan range from 350 to 1500 Th. Data-dependent MS2 scans were carried out at a resolution of 45000 with an isolation window of 0.7 Th and a maximum injection time of 86 ms using the top 20 peaks from each precursor scan for HCD fragmentation. For the data analysis, the MaxQuant software package version 1.6.10.43 (Cox & Mann, 2008) was used. A FDR cutoff of 0.01 was applied for peptides and proteins and database search was performed using the mouse Uniprot database (July 2018), including isoforms. Variable modifications included phosphorylation on serine, threonine and tyrosine, methionine-oxidation, acetylated N-termini and deamidation of asparagine and glutamine, while the TMT10-plex reporter ion quantitation was turned on using a PIF setting of 0.5. Log2-transformed and median-MAD centered corrected reporter ion intensities were used for quantitation. Protein groups were filtered for proteins, which were identified by at least one unique peptide and at least two peptides in total and had valid values across all samples. Phosphorylation site tables were filtered for valid values across all samples. For significance calling, a two-sample moderated t-testing (limma R package) (Ritchie *et al*, 2015) was applied. A multiple comparison correction was done using the Benjamini-Hochberg method (adjusted P-values). The KEGG PATHWAY (mmu04310) and a previously published list (Herbst *et al*, 2014) served as a combined reference protein list for the Wnt signaling heatmap. The KEGG PATHWAY (mmu04330) served as a

reference protein list for the Notch signaling heatmap. A previously published list (Zanconato *et al*, 2015) served as a reference protein list for the Yap signaling heatmap.

Section staining

The tubuloids were released from Matrigel by mechanical disruption, collected in a conical tube and fixed in 10% (v/v) Neutral-buffered Formalin overnight. The tubuloids were transferred to a 2 ml tube and overlayed with 1.5% agarose. The resulting agarose beads were dehydrated and embedded in paraffin. All stainings were performed on 5 µm sections. For haematoxylin-eosin (H&E) staining, sections were rehydrated and stained with haematoxylin (Fluka) for 4 min and with eosin (Merck) for 2 min. For immunofluorescence, sections were rehydrated, and antigen retrieval in TRIS-EDTA and blocking with 10% donkey serum (Bio-Rad) were performed. Sections were incubated overnight with the primary antibodies: rat anti-BrdU (1:100, Abcam, ab6326), mouse anti-E-CAD (1:300, BD Biosciences, 610181), rabbit anti-Laminin (1:500, Abcam, ab11575), rat anti-ZO-1 (1:200, Santa Cruz, sc-33725), mouse anti-MDR1 (1:50, Santa Cruz, sc-55510) and mouse anti-AQP3 (1:50, Santa Cruz, sc-518001) or with the lectins: Biotinylated LTL (1:300, Vector Laboratories, B-1325) and Rhodamine-conjugated PNA (1:300, Vector Laboratories, RL-1072), followed by incubation with the donkey fluorescent dye-conjugated secondary antibodies: Alexa488 anti-mouse, Alexa488 anti-rabbit, Alexa488 anti-rat and Cy3 anti-rat (1:250, Jackson) or with Alexa647-conjugated Streptavidin (1:200, Thermo Fisher Scientific), and by counterstaining with DAPI (0.2 µg/ml, Thermo Fisher Scientific) for 1 hr. For immunohistochemistry, sections were rehydrated, antigen retrieval in TRIS-EDTA was performed, endogenous peroxidase activity was blocked in 3.5% (v/v) hydrogen peroxide and blocking with 10% donkey serum (Bio-Rad) was performed. Sections were incubated overnight with the primary rabbit anti-Pax8 antibody (1:2000, Proteintech, 10336-1-AP), followed by incubation with the peroxidase-conjugated donkey anti-rabbit secondary antibody from a kit (Dako) for 1 hr. Sections were developed using the substrate-chromogen system (Dako) and counterstained with haematoxylin (Fluka) for 2 min. Kidneys and spleens were fixed in 10% (v/v) Neutral-buffered Formalin overnight, dehydrated and embedded in paraffin. All stainings were performed on 5 µm sections. For immunohistochemistry, sections were rehydrated, antigen retrieval in TRIS-EDTA was performed, endogenous peroxidase activity was blocked in 3.5% (v/v) hydrogen peroxide and blocking with 10% donkey serum (Bio-Rad) was performed. Sections were incubated overnight with the primary antibodies: rabbit anti-Ki67 (1:200, Thermo Fisher Scientific, RM-9106-S), mouse anti-phospho-γH2AX (1:500, Merck Millipore, 05-636), mouse anti-p53 (1:100, Santa Cruz, sc-126) and mouse anti-p21 (1:100, Santa Cruz, sc-6246), followed by incubation with

the peroxidase-conjugated donkey anti-rabbit and anti-mouse secondary antibodies from a kit (Dako) for 1 hr. Sections were developed using the substrate-chromogen system (Dako) and counterstained with haematoxylin (Fluka) for 2 min. For PAS staining, sections were rehydrated, stained using the Periodic Acid-Schiff (PAS) Kit (Sigma-Aldrich) according to the manufacturer's instructions and counterstained with haematoxylin (Fluka) for 2 min. For LacZ staining, cryosections were prepared. Kidneys were placed in 30% sucrose in PBS overnight and embedded in OCT compound (Sakura Finetek). 10 µm sections were fixed in 0.2% (v/v) glutaraldehyde for 10 min, washed three times in washing solution (PBS, 2 mM $MgCl_2$, 0.01% sodium deoxycholate and 0.02% NP-40), incubated overnight in staining solution (PBS, 2 mM $MgCl_2$, 0.01% sodium deoxycholate, 0.02% NP-40, 5 mM $K_3Fe(CN)_6$, 5 mM $K_4Fe(CN)_6$ and 1 mg/ml X-gal (Roth)) and counterstained with nuclear fast red (Merck) for 5 min. Images were taken with an AxioImager Z1 microscope (for immunofluorescence) or an Axio Scope.A1 microscope (for H&E staining, PAS staining, LacZ staining and immunohistochemistry) using the Zen software (all Zeiss). Selected immunofluorescence images were processed with Fiji ImageJ.

Whole mount staining

The tubuloids were released from Matrigel by mechanical disruption, collected, transferred to a 2 ml tube, fixed in 10% (v/v) Neutral-buffered Formalin for 1.5 hrs and blocked in 10% donkey serum (Bio-Rad) for 2 hrs. The tubuloids were incubated overnight with the mouse anti-E-CAD antibody (1:300, BD Biosciences, 610181), the Biotinylated LTL lectin (1:300, Vector Laboratories, B-1325) and the Rhodamine-conjugated PNA lectin (1:300, Vector Laboratories, RL-1072), and then were incubated overnight with the donkey Alexa488 anti-mouse antibody (1:250, Jackson), Alexa647-conjugated Streptavidin (1:200, Thermo Fisher Scientific) and DAPI (0.2 µg/ml, Thermo Fisher Scientific). The tubuloids were taken up in 1.5% low-melting agarose and transferred to chamber slides. Confocal z-stacks were acquired with a LSM700 or LSM710 microscope (Zeiss) using a long working distance C-Achroplan 32x/0.85 water immersion objective and Immersol W (Zeiss). DAPI, Alexa488, Cy3 and Alexa647 fluorophores were excited with a 405 nm, 488 nm, 561 nm and 633 nm laser, respectively, and detected by sequential scanning using BP filters 410-460 nm, 500-540 nm, 565-620 nm and 640-720 nm, respectively. Images were acquired with a pixel size of 0.116 or 0.142 µm (lateral) and 1.11 or 1.16 µm (axial) with 12-bit and line average 2. If necessary, detector gain and laser power were slightly adjusted with z-depth to keep a constant signal. Restoration of confocal z-stacks was performed with the Huygens Deconvolution software (SVI) running on a dedicated data processing workstation

(Acquifer) using a CMLE algorithm with 60 iterations and a SNR of 12. After deconvolution, confocal z-stacks were 3D reconstructed using the Imaris 9.1 software (Bitplane/Oxford Instruments) and either the volume reconstruction and clipping planes or orthogonal sections were used to visualize and explore the 3D structure of the tubuloids.

Transmission electron microscopy

The tubuloids were released from Matrigel by mechanical disruption, collected in a conical tube and fixed in 2% (w/v) formaldehyde and 2.5% (v/v) glutaraldehyde in 0.1 M phosphate buffer for 2 hrs. After embedding in 10% agarose in a 2 ml tube, samples were post-fixed with 1% (v/v) osmium tetroxide (Sigma-Aldrich), dehydrated in a graded series of EtOH and embedded in PolyBed® 812 resin (Polysciences). Ultrathin sections (60-80 nm) were stained with uranyl acetate (Polysciences) and lead citrate (Sigma-Aldrich) and examined at 80 kV with an EM 910 electron microscope (Zeiss). Acquisition was performed with a Quemesa CCD camera and the iTEM software (Emsis).

TUNEL assay

Kidneys were fixed in 10% (v/v) Neutral-buffered Formalin overnight, dehydrated and embedded in paraffin. 5 µm sections were rehydrated, stained using the ApopTag Plus Peroxidase *In Situ* Apoptosis Detection Kit (Merck Millipore) according to the manufacturer's instructions and counterstained with haematoxylin (Fluka) for 2 min. Images were taken with an Axio Scope.A1 microscope using the Zen software (Zeiss).

Immunoblotting

Tubuloid pellets were lysed in RIPA buffer supplemented with protease inhibitors (Roche) for 10 min. 10 µg of protein was separated by SDS-PAGE using a 15% separating and a 4.5% stacking gel and transferred to a PVDF membrane with 0.2 µm pore size (Roth) via a semidry transfer. The membrane was blocked with 5% skim milk in TBS-T, cut in half and probed with the rabbit anti-Cleaved Caspase-3 (1:1000, Cell Signaling, 9661) or mouse anti-α-Tubulin (1:10000, Sigma-Aldrich, T9026) antibody overnight and with the peroxidase-conjugated donkey anti-rabbit (1:10000) or anti-mouse (1:5000) antibody (Jackson) for 1 hr. The antibodies were diluted in 5% BSA in TBS-T. Bands were visualized using the Western Lightning Plus-ECL substrate (PerkinElmer) for 5 min and a Fusion SL imaging system (Vilber). Whole kidneys were homogenized and protein was extracted from 20 mg of tissue in 1 ml RIPA buffer supplemented with protease inhibitors (Roche) for 2 hrs. 10 µg of protein was separated by SDS-PAGE using a 10% separating and a 4.5% stacking gel and transferred to a PVDF membrane

with 0.2 µm pore size (Roth) via a semidry transfer. The membrane was blocked with 5% skim milk in TBS-T, cut in half and probed with the mouse anti-β-catenin (1:1000, BD Transduction Laboratories, 610153) or mouse anti-α-Tubulin (1:10000, Sigma-Aldrich, T9026) antibody overnight and with the peroxidase-conjugated donkey anti-mouse antibody (1:5000, Jackson) for 1 hr. The antibodies were diluted in 5% BSA in TBS-T. Bands were visualized using the Western Lightning Plus-ECL substrate (PerkinElmer) for 5 min and a Fusion SL imaging system (Vilber).

Real-time qPCR

Total RNA from the tubuloids and whole mouse kidneys was isolated using TRIzol (Invitrogen) and 1 µg/20 µl of RNA was reversely transcribed to cDNA using MMLV reverse transcriptase (Promega) according to the manufacturer's instructions. Real-time qPCR reactions were performed in a CFX96-C1000 thermal cycler (Bio-Rad) with the PowerUp SYBR Green Master Mix (Applied Biosystems) and 10 µM exon-exon junction-spanning primers, using a standard protocol with 44 cycles according to the manufacturer's instructions. Primer sequences are listed in the Table 2. Primer specificity was tested by melting curve analyses and running reactions with a negative control (without cDNA). Relative mRNA expression values were normalized to the endogenous control Gapdh using the $2^{-\Delta\Delta Ct}$ method.

Table 2

Primer sequences for real-time qPCR.

Gene	Forward primer 5'-3'	Reverse primer 5'-3'
Krt8	CTCAAAGGCCAGAGGGCATC	TTAATGGCCATCTCCCCACG
Krt18	ACTGGTCTCAGCAGATTGAGG	CCGAGGCTGTTCTCCAAGTT
Cldn4	CTTCATCGGCAGCAACATCG	GATGACCATAAGGGCTCGGG
Abcb1b	AGTGGCTCTTGAAGCCGTAA	AAACTCCATCACCACCTCACG
Slc3a1	AAAATGCCTTGACTGGTGGCA	CCTCAACAGCGTATCTGAAGTCT
Slc40a1	GAGCCAGTGTCCCCAACTAC	CTTGCAGCAACTGTGTCACC
Aqp3	ATCGTTGTGGGGAGATGCTT	ACCAAGATGCCAAGGGTGAC
Atp6ap2	GGCAAAACAAGAGAACACCCA	CCAAGGCCAAGCCGATCATA

Wnk1	CCTCAAGTATGGCACAGGGG	GCTGTATTCCCTGCTGCTGA
Cldn1	TGGGGCTGATCGCAATCTTT	CACTAATGTCGCCAGACCTGA
Vcam1	CTTTATGTCAACGTTGCCCCC	GAGGCTGCAGTTCCCCATTA
Cald1	GTTGCTGCCCTAGAGATAGTCA	CCTGAGTTCTCTGCGACGTT
Pdgfrb	ACTATGTCCCATCTGCCCCT	ATCTTGACCAGCTTGCCCTC
Meis1	ATTCACACTGCTGGAGACGC	TAGGTCGTCGTACCTTTGCG
Pecam1	GAGCCTCACCAAGAGAACGG	ATTGGATGGCTTGGCCTGAA
Cdh5	GCTCACGGACAAGATCAGCTC	GGGGGTGTCTATCTGGGGAA
Flt1	CACCCCTGTCACCACAATCA	CACCAATGTGCTAACCGTCTTA

Dkk1	CGGGGGATGGATATCCCAGA	ACGGAGCCTTCTTGTCCTTTG
Axin2	GCGCTTTGATAAGGTCCTGG	TCATGTGAGCCTCCTCTCTTTT
Cyclin D1	CTGGATGCTGGAGGTCTGTGA	AGGGGGTCCTTGTTTAGCCAG
Myc	TTGGAAACCCCGCAGACAG	GCTGTACGGAGTCGTAGTCG
Hey1	GAGCGTGAGTGGGATCAGTG	GCTTAGCAGATCCCTGCTTCT
Hes1	CTGGTGCTGATAACAGCGGA	GGAATGCCGGGAGCTATCTT
Hey3 (Heyl)	GTCTTGCAGATGACCGTGGA	CGGGCATCAAAGAACCCTGT
Ca9	GTCATTGGAGCTATGGAGG	CTCATAACCCAGAAGTTCCAG
Hk2	GTGACAGACAATGGTCTCCAGAG	GCCAGGCATTCGGCAATG
Pdk1	GCAGTTCCTGGACTTCG	CAATCTAACAGGCAACTCTTG
Ldha	GATGGATCTCCAGCATGGCAG	GTGATAATGACCAGCTTGGAGTTCG
Glut1	GCTATAACACTGGTGTCATCAACG	CGTGGTGAGTGTGGTGGATG
Vegfa	CAGGCTGCTGTAACGATGAA	TTTCTTGCGCTTTCGTTTTT

Ngal	ACAACCAGTTCGCCATGGTA	AAGCGGGTGAAACGTTCCTT
Kim-1	CAGGGTCTCCTTCACAGCAG	CCACCACCCCCTTTACTTCC
Gsta1	AGCCCGTGCTTCACTACTTC	CAATCTCCACCATGGGCACT
Il1b	TTCAGGCAGGCAGTATCA	CCAGCAGGTTATCATCATCA
Cd11b	CCACACTAGCATCAAGGGCA	GCTTCACACTGCCACCGT
Ly6c	GCAGTGCTACGAGTGCTATGG	ACTGACGGGTCTTTAGTTTCCTT
Icam1 (Cd54)	GTCCGCTGTGCTTTGAGAAC	GAGGTCCTTGCCTACTTGCT
Cd68	ACTTCGGGCCATGTTTCTCT	GCTGGTAGGTTGATTGTCGT
Ccr2 (Cd192)	GCCATCATAAAGGAGCCATACC	ATGCCGTGGATGAACTGAGG
Vim	TGGATCAGCTCACCAACGAC	AAGGTCAAGACGTGCCAGAG
Fn1	ATGAGAAGCCTGGATCCCCT	GGAAGGGTAACCAGTTGGGG
a-sma	ACATCAAGGAGAAGCTGTGCT	TTTCGTGGATGCCCGCTG
Col1a1	CATGAGCCGAAGCTAACCCC	GGGTTTCCACGTCTCACCAT
Col3a1	AGTGGGCATCCAGGTCCTAT	GGGTGAAAAGCCACCAGACT

Genomic DNA PCR

Genomic DNA was isolated from whole kidneys using the GeneJET Genomic DNA Purification Kit (Thermo Fisher Scientific) according to the manufacturer's instructions. *β-catenin* and *Vhl* alleles were amplified using 100 ng of DNA, 10 µM primers and a standard protocol with 50 and 40 cycles and annealing temperature of 65°C and 56°C, respectively. A forward primer 5'-3': GGTACCTGAAGCTCAGCGCACAGCTG and a reverse primer 5'-3': ACGTGTGGCAAGTTCCGCGTCATCC were used to amplify the *β-catenin* allele (Harada *et al*, 1999). A forward primer 1 5'-3': CTGGTACCCACGAAACTGTC, a forward primer 2 5'-3': CTAGGCACCGAGCTTAGAGGTTTGCG and a reverse primer 5'-3': CTGACTTCCACTGATGCTTGTCACAG were used to amplify the *Vhl* allele (Rankin *et al*, 2006).

Drug response assay

Single cells were seeded at 15000 cells per well in 9 µl Matrigel (75%, Corning) lenses in 96-well plates and overlayed with 100 µl tubuloid medium. After 24 hrs, medium was replaced with fresh medium containing gefitinib (Selleckchem), U0126 (Selleckchem), BYL719 (Selleckchem), ICG-001 (Biochempartner), LF3 (Selleckchem) or cisplatin (Cayman Chemical). Medium was changed every other day. CellTiterGlo assay (Promega) was performed after 6 days according to the manufacturer's instructions.

Blood assays

Blood was collected from hearts of freshly sacrificed mice to tubes coated with 0.5 M EDTA pH 8 (Invitrogen) to prevent clotting. BUN concentrations were measured using the i-STAT 1 System with the CHEM8+ cartridges for patient testing (Abbott) according to the manufacturer's instructions. For plasma collection, cells and platelets were pelleted from the blood by centrifugation for 15 min at 2000 g. EPO concentrations in supernatants (plasma) were measured using the Quantikine Mouse Erythropoietin Immunoassay (R&D Systems) according to the manufacturer's instructions.

Descriptive statistics and significance testing

The Pearson correlation matrix (coefficient) was calculated by the cor function of the base R package between all samples of the mouse kidney epithelia (CK), early passage tubuloids (TEP) and long-term passage tubuloids (TLP) based on normalized log2 intensity values for all ~ 9000 proteins and ~ 16000 phosphorylation sites detected in the mass spectrometry analysis. The matrix was plotted using the pheatmap R package. For the functional annotation clustering of the most upregulated proteins using the DAVID bioinformatic tool (DAVID Bioinformatics Resources 6.8, NIAID/NIH), all ~ 9000 proteins detected in the proteomic analysis were subjected to both the 0.1% FDR cutoff (adjusted P-value < 0.001) and log2 fold change cutoff of > 0.5 for both TEP over CK and TLP over CK. 722 proteins were selected. Using the entire mouse (Mus musculus) proteome as a background for the UNIPROT_ACCESSION identifier, 671 proteins (DAVID IDs) were identified and analyzed. Defined DAVID defaults were used and the Enrichment Thresholds (EASE Scores, modified Fisher-exact P-values) and adjusted P-values (Benjamini-Hochberg correction) for all terms in each cluster were subjected to the cutoff of < 0.001. 10 clusters were determined. The overall enrichment score for each cluster was calculated based on the Enrichment Thresholds for all terms. The most enriched term was selected to represent each cluster based on the lowest adjusted P-value. All other statistical analyses were performed in GraphPad Prism (GraphPad). All data are presented as means ± SD (error bars), unless otherwise stated. To assess the normal

distribution of the data, the Shapiro-Wilk test (α = 0.05) was performed. The unpaired, two-tailed Student's t-test and the ordinary one-way ANOVA followed by the Dunnett's multiple comparison were used to analyze data, which passed the normality test. To compare groups, which did not pass the normality test, the alternative non-parametric Kruskal-Wallis test followed by the Dunn's multiple comparison were performed. The ordinary one-way ANOVA followed by the Dunnett's multiple comparison were used to analyze the real-time qPCR data on the tubuloids. A P-value < 0.05 was considered statistically significant. IC50 values were calculated by a non-linear regression analysis of the response and log10 of the inhibitor concentration fitting a curve with a variable slope (4 parameters). Statistical details of the experiments can be found in the figure captions.

References

Ai Q, Ma X, Huang Q, Liu S, Shi T, Zhang C, Zhu M, Zhang Y, Wang B, Ni D, Li H, Zheng T & Zhang X (2012) High-Level Expression of Notch1 Increased the Risk of Metastasis in T1 Stage Clear Cell Renal Cell Carcinoma. *PLoS One* **7:** e35022

Albers J, Rajski M, Schönenberger D, Harlander S, Schraml P, von Teichman A, Georgiev S, Wild PJ, Moch H, Krek W & Frew IJ (2013) Combined mutation of Vhl and Trp53 causes renal cysts and tumours in mice. *EMBO Mol. Med.* **5:** 949–964

van Amerongen R (2020) Celebrating Discoveries in Wnt Signaling: How One Man Gave Wings to an Entire Field. *Cell* **181:** 487–491

Angelotti ML, Ronconi E, Ballerini L, Peired A, Mazzinghi B, Sagrinati C, Parente E, Gacci M, Carini M, Rotondi M, Fogo AB, Lazzeri E, Lasagni L & Romagnani P (2012) Characterization of Renal Progenitors Committed Toward Tubular Lineage and Their Regenerative Potential in Renal Tubular Injury. *Stem Cells* **30:** 1714–1725

Aqeilan RI (2021) Engineering organoids: a promising platform to understand biology and treat diseases. *Cell Death Differ.* **28:** 1–4

Bailey ST, Smith AM, Kardos J, Wobker SE, Wilson HL, Krishnan B, Saito R, Lee HJ, Zhang J, Eaton SC, Williams LA, Manocha U, Peters DJ, Pan X, Carroll TJ, Felsher DW, Walter V, Zhang Q, Parker JS, Yeh JJ, et al (2017) MYC activation cooperates with Vhl and Ink4a/Arf loss to induce clear cell renal cell carcinoma. *Nat. Commun.* **8:** 15770

Barker N, Rookmaaker MB, Kujala P, Ng A, Leushacke M, Snippert H, van de Wetering M, Tan S, Van Es JH, Huch M, Poulsom R, Verhaar MC, Peters PJ & Clevers H (2012) Lgr5+ve Stem/Progenitor Cells Contribute to Nephron Formation during Kidney Development. *Cell Rep.* **2:** 540–552

Batlle E & Clevers H (2017) Cancer stem cells revisited. *Nat. Med.* **23:** 1124–1134

Behrens J (2008) One hit, two outcomes for VHL-mediated tumorigenesis. *Nat. Cell Biol.* **10:** 1127–1128

Behrens J, Jerchow BA, Würtele M, Grimm J, Asbrand C, Wirtz R, Kühl M, Wedlich D & Birchmeier W (1998) Functional Interaction of an Axin Homolog, Conductin, with Beta-Catenin, APC, and GSK3. *Science* **280:** 596–599

Behrens J, von Kries JP, Kühl M, Bruhn L, Wedlich D, Grosschedl R & Birchmeier W (1996) Functional interaction of β-catenin with the transcription factor LEF-1. *Nature* **382:** 638–642

Bertout JA, Patel SA & Simon MC (2008) The impact of O2 availability on human cancer. *Nat. Rev. Cancer* **8:** 967–975

Bhagat TD, Zou Y, Huang S, Park J, Palmer MB, Hu C, Li W, Shenoy N, Giricz O, Choudhary G, Yu Y, Ko Y-A, Izquierdo MC, Park ASD, Vallumsetla N, Laurence R, Lopez R, Suzuki M, Pullman J, Kaner J, et al (2017) Notch Pathway Is Activated via Genetic and Epigenetic Alterations and Is a Therapeutic Target in Clear Cell Renal Cancer. *J. Biol. Chem.* **292:** 837–846

Bielesz B, Sirin Y, Si H, Niranjan T, Gruenwald A, Ahn S, Kato H, Pullman J, Gessler M, Haase VH & Susztak K (2010) Epithelial Notch signaling regulates interstitial fibrosis development in the kidneys of mice and humans. *J. Clin. Invest.* **120:** 4040–4054

Boj SF, Hwang C-I, Baker LA, Chio IIC, Engle DD, Corbo V, Jager M, Ponz-Sarvise M, Tiriac H, Spector MS, Gracanin A, Oni T, Yu KH, van Boxtel R, Huch M, Rivera KD, Wilson JP, Feigin ME, Öhlund D, Handly-Santana A, et al (2015) Organoid Models of Human and Mouse Ductal Pancreatic Cancer. *Cell* **160:** 324–338

Bolck HA, Corrò C, Kahraman A, von Teichman A, Toussaint NC, Kuipers J, Chiovaro F, Koelzer VH, Pauli C, Moritz W, Bode PK, Rechsteiner M, Beerenwinkel N, Schraml P & Moch H (2021) Tracing Clonal Dynamics Reveals that Two- and Three-dimensional Patient-derived Cell Models Capture Tumor Heterogeneity of Clear Cell Renal Cell Carcinoma. *Eur. Urol. Focus* **7:** 152–162

Broutier L, Mastrogiovanni G, Verstegen MMA, Francies HE, Gavarró LM, Bradshaw CR, Allen GE, Arnes-Benito R, Sidorova O, Gaspersz MP, Georgakopoulos N, Koo B-K, Dietmann S, Davies SE, Praseedom RK, Lieshout R, IJzermans JNM, Wigmore SJ, Saeb-Parsy K, Garnett MJ, et al (2017) Human primary liver cancer–derived organoid cultures for disease modeling and drug screening. *Nat.*

Med. **23:** 1424–1435

Bruno S & Camussi G (2012) Isolation and Characterization of Resident Mesenchymal Stem Cells in Human Glomeruli. *Methods Mol. Biol.* **879:** 367–380

Brunskill EW, Park J-S, Chung E, Chen F, Magella B & Potter SS (2014) Single cell dissection of early kidney development: multilineage priming. *Development* **141:** 3093–3101

Bugter JM, Fenderico N & Maurice MM (2021) Mutations and mechanisms of WNT pathway tumour suppressors in cancer. *Nat. Rev. Cancer* **21:** 5–21

Bussolati B, Bruno S, Grange C, Buttiglieri S, Deregibus MC, Cantino D & Camussi G (2005) Isolation of Renal Progenitor Cells from Adult Human Kidney. *Am. J. Pathol.* **166:** 545–555

Büttner F, Winter S, Rausch S, Reustle A, Kruck S, Junker K, Stenzl A, Agaimy A, Hartmann A, Bedke J, Schwab M & Schaeffeler E (2015) Survival Prediction of Clear Cell Renal Cell Carcinoma Based on Gene Expression Similarity to the Proximal Tubule of the Nephron. *Eur. Urol.* **68:** 1016–1020

Calandrini C, Schutgens F, Oka R, Margaritis T, Candelli T, Mathijsen L, Ammerlaan C, van Ineveld RL, Derakhshan S, de Haan S, Dolman E, Lijnzaad P, Custers L, Begthel H, Kerstens HHD, Visser LL, Rookmaaker M, Verhaar M, Tytgat GAM, Kemmeren P, et al (2020) An organoid biobank for childhood kidney cancers that captures disease and tissue heterogeneity. *Nat. Commun.* **11:** 1310

Calzada MJ, Esteban MA, Feijoo-Cuaresma M, Castellanos MC, Naranjo-Suárez S, Temes E, Méndez F, Yánez-Mo M, Ohh M & Landázuri MO (2006) von Hippel-Lindau Tumor Suppressor Protein Regulates the Assembly of Intercellular Junctions in Renal Cancer Cells through Hypoxia-Inducible Factor–Independent Mechanisms. *Cancer Res.* **66:** 1553–1560

Cato ACB, Nestl A & Mink S (2002) Rapid Actions of Steroid Receptors in Cellular Signaling Pathways. *Sci. Signal.* **2002:** re9

Chang WH & Lai AG (2019) Pan-cancer genomic amplifications underlie a WNT hyperactivation phenotype associated with stem cell-like features leading to poor prognosis. *Transl. Res.* **208:** 47–62

Chanrion M, Kuperstein I, Barrière C, El Marjou F, Cohen D, Vignjevic D, Stimmer L, Paul-Gilloteaux P, Bièche I, Tavares SDR, Boccia G-F, Cacheux W, Meseure D, Fre S, Martignetti L, Legoix-Né P, Girard E, Fetler L, Barillot E, Louvard D, et al (2014) Concomitant Notch activation and p53 deletion trigger epithelial-to-mesenchymal transition and metastasis in mouse gut. *Nat. Commun.* **5:** 5005

Chapman JM & Karniski LP (2010) Protein localization of SLC26A2 (DTDST) in rat kidney. *Histochem. Cell Biol.* **133:** 541–547

Chen F, Zhang Y, Şenbabaoğlu Y, Ciriello G, Yang L, Reznik E, Shuch B, Micevic G, De Velasco G, Shinbrot E, Noble MS, Lu Y, Covington KR, Xi L, Drummond JA, Muzny D, Kang H, Lee J, Tamboli P, Reuter V, et al (2016a) Multilevel Genomics-Based Taxonomy of Renal Cell Carcinoma. *Cell Rep.* **14:** 2476–2489

Chen J, Chen J-K, Conway EM & Harris RC (2013) Survivin Mediates Renal Proximal Tubule Recovery from AKI. *J. Am. Soc. Nephrol.* **24:** 2023–2033

Chen J, Vijayakumar S, Li X & Al-Awqati Q (1998) Kanadaptin Is a Protein That Interacts with the Kidney but Not the Erythroid Form of Band 3. *J. Biol. Chem.* **273:** 1038–1043

Chen J, You H, Li Y, Xu Y, He Q & Harris RC (2018) EGF Receptor–Dependent YAP Activation Is Important for Renal Recovery from AKI. *J. Am. Soc. Nephrol.* **29:** 2372–2385

Chen W, Hill H, Christie A, Kim MS, Holloman E, Pavia-Jimenez A, Homayoun F, Ma Y, Patel N, Yell P, Hao G, Yousuf Q, Joyce A, Pedrosa I, Geiger H, Zhang H, Chang J, Gardner KH, Bruick RK, Reeves C, et al (2016b) Targeting renal cell carcinoma with a HIF-2 antagonist. *Nature* **539:** 112–117

Chitalia VC, Foy RL, Bachschmid MM, Zeng L, Panchenko M V., Zhou MI, Bharti A, Seldin DC, Lecker SH, Dominguez I & Cohen HT (2008) Jade-1 inhibits Wnt signalling by ubiquitylating β-catenin and mediates Wnt pathway inhibition by pVHL. *Nat. Cell Biol.* **10:** 1208–1216

Chiu S-C, Liu H-H, Chen C-L, Chen P-R, Liu M-C, Lin S-Z & Chang K-T (2015) Extramedullary Hematopoiesis (EMH) in Laboratory Animals: Offering an Insight into Stem Cell Research. *Cell Transplant.* **24:** 349–366

Cho H, Du X, Rizzi JP, Liberzon E, Chakraborty AA, Gao W, Carvo I, Signoretti S, Bruick RK, Josey JA, Wallace EM & Kaelin WG (2016) On-target efficacy of a HIF-2α antagonist in preclinical kidney cancer models. *Nature* **539:** 107–111

Clark PE, Polosukhina D, Love H, Correa H, Coffin C, Perlman EJ, de Caestecker M, Moses HL & Zent R (2011) β-Catenin and K-RAS Synergize to Form Primitive Renal Epithelial Tumors with Features of Epithelial Wilms' Tumors. *Am. J. Pathol.* **179:** 3045–3055

Clevers H (2016) Modeling Development and Disease with Organoids. *Cell* **165:** 1586–1597

Cole AM, Ridgway RA, Derkits SE, Parry L, Barker N, Clevers H, Clarke AR & Sansom OJ (2010) p21 loss blocks senescence following Apc loss and provokes tumourigenesis in the renal but not the intestinal epithelium. *EMBO Mol. Med.* **2:** 472–486

Courtney KD, Infante JR, Lam ET, Figlin RA, Rini BI, Brugarolas J, Zojwalla NJ, Lowe AM, Wang K, Wallace EM, Josey JA & Choueiri TK (2018) Phase I Dose-Escalation Trial of PT2385, a First-in-Class Hypoxia-Inducible Factor-2α Antagonist in Patients With Previously Treated Advanced Clear Cell Renal Cell Carcinoma. *J. Clin. Oncol.* **36:** 867–874

Cox J & Mann M (2008) MaxQuant enables high peptide identification rates, individualized p.p.b.-range mass accuracies and proteome-wide protein quantification. *Nat. Biotechnol.* **26:** 1367–1372

Creighton CJ, Morgan M, Gunaratne PH, Wheeler DA, Gibbs RA, Robertson G, Chu A, Beroukhim R, Cibulskis K, Signoretti S, Vandin F, Wu HT, Raphael BJ, Verhaak RGW, Tamboli P, Torres-Garcia W, Akbani R, Weinstein JN, Reuter V, Hsieh JJ, et al (2013) Comprehensive molecular characterization of clear cell renal cell carcinoma. *Nature* **499:** 43–49

Cruciat C-M & Niehrs C (2013) Secreted and Transmembrane Wnt Inhibitors and Activators. *Cold Spring Harb. Perspect. Biol.* **5:** a015081

Drost J, van Jaarsveld RH, Ponsioen B, Zimberlin C, van Boxtel R, Buijs A, Sachs N, Overmeer RM, Offerhaus GJ, Begthel H, Korving J, van de Wetering M, Schwank G, Logtenberg M, Cuppen E, Snippert HJ, Medema JP, Kops GJPL & Clevers H (2015) Sequential cancer mutations in cultured human intestinal stem cells. *Nature* **521:** 43–47

Drost J, Karthaus WR, Gao D, Driehuis E, Sawyers CL, Chen Y & Clevers H (2016) Organoid culture systems for prostate epithelial and cancer tissue. *Nat. Protoc.* **11:** 347–358

Edeling M, Ragi G, Huang S, Pavenstädt H & Susztak K (2016) Developmental signalling pathways in renal fibrosis: the roles of Notch, Wnt and Hedgehog. *Nat. Rev. Nephrol.* **12:** 426–439

van Es JH, van Gijn ME, Riccio O, van den Born M, Vooijs M, Begthel H, Cozijnsen M, Robine S, Winton DJ, Radtke F & Clevers H (2005) Notch/γ-secretase inhibition turns proliferative cells in intestinal crypts and adenomas into goblet cells. *Nature* **435:** 959–963

Espana-Agusti J, Tuveson DA, Adams DJ & Matakidou A (2015) A minimally invasive, lentiviral based method for the rapid and sustained genetic manipulation of renal tubules. *Sci. Rep.* **5:** 11061

Espana-Agusti J, Warren A, Chew SK, Adams DJ & Matakidou A (2017) Loss of PBRM1 rescues VHL dependent replication stress to promote renal carcinogenesis. *Nat. Commun.* **8:** 2026

Espana-Agusti J, Zou X, Wong K, Fu B, Yang F, Tuveson DA, Adams DJ & Matakidou A (2016) Generation and Characterisation of a Pax8-CreERT2 Transgenic Line and a Slc22a6-CreERT2 Knock-In Line for Inducible and Specific Genetic Manipulation of Renal Tubular Epithelial Cells. *PLoS One* **11:** e0148055

Fang L, Zhu Q, Neuenschwander M, Specker E, Wulf-Goldenberg A, Weis WI, von Kries JP & Birchmeier W (2016) A Small-Molecule Antagonist of the β-Catenin/TCF4 Interaction Blocks the Self-Renewal of Cancer Stem Cells and Suppresses Tumorigenesis. *Cancer Res.* **76:** 891–901

Fendler A, Bauer D, Busch J, Jung K, Wulf-Goldenberg A, Kunz S, Song K, Myszczyszyn A, Elezkurtaj S, Erguen B, Jung S, Chen W & Birchmeier W (2020) Inhibiting WNT and NOTCH in renal cancer stem cells and the implications for human patients. *Nat. Commun.* **11:** 929

Feng C, Xiong Z, Jiang H, Ding Q, Fang Z & Hui W (2016) Genetic alteration in notch pathway is associated with better prognosis in renal cell carcinoma. *Biofactors* **42:** 41–48

Ferenbach DA & Bonventre J V. (2015) Mechanisms of maladaptive repair after AKI leading to accelerated

kidney ageing and CKD. *Nat. Rev. Nephrol.* **11:** 264–276

Freedman BS, Brooks CR, Lam AQ, Fu H, Morizane R, Agrawal V, Saad AF, Li MK, Hughes MR, Werff R Vander, Peters DT, Lu J, Baccei A, Siedlecki AM, Valerius MT, Musunuru K, McNagny KM, Steinman TI, Zhou J, Lerou PH, et al (2015) Modelling kidney disease with CRISPR-mutant kidney organoids derived from human pluripotent epiblast spheroids. *Nat. Commun.* **6:** 8715

Frew IJ, Thoma CR, Georgiev S, Minola A, Hitz M, Montani M, Moch H & Krek W (2008) pVHL and PTEN tumour suppressor proteins cooperatively suppress kidney cyst formation. *EMBO J.* **27:** 1747–1757

Fujii M, Shimokawa M, Date S, Takano A, Matano M, Nanki K, Ohta Y, Toshimitsu K, Nakazato Y, Kawasaki K, Uraoka T, Watanabe T, Kanai T & Sato T (2016) A Colorectal Tumor Organoid Library Demonstrates Progressive Loss of Niche Factor Requirements during Tumorigenesis. *Cell Stem Cell* **18:** 827–838

Gerlinger M, Horswell S, Larkin J, Rowan AJ, Salm MP, Varela I, Fisher R, McGranahan N, Matthews N, Santos CR, Martinez P, Phillimore B, Begum S, Rabinowitz A, Spencer-Dene B, Gulati S, Bates PA, Stamp G, Pickering L, Gore M, et al (2014) Genomic architecture and evolution of clear cell renal cell carcinomas defined by multiregion sequencing. *Nat. Genet.* **46:** 225–233

Gerlinger M, Rowan AJ, Horswell S, Larkin J, Endesfelder D, Gronroos E, Martinez P, Matthews N, Stewart A, Tarpey P, Varela I, Phillimore B, Begum S, McDonald NQ, Butler A, Jones D, Raine K, Latimer C, Santos CR, Nohadani M, et al (2012) Intratumor Heterogeneity and Branched Evolution Revealed by Multiregion Sequencing. *N. Engl. J. Med.* **366:** 883–892

Gijzen L, Yousef Yengej FA, Schutgens F, Vormann MK, Ammerlaan CME, Nicolas A, Kurek D, Vulto P, Rookmaaker MB, Lanz HL, Verhaar MC & Clevers H (2021) Culture and analysis of kidney tubuloids and perfused tubuloid cells-on-a-chip. *Nat. Protoc.***:** 9–12

Gossage L, Eisen T & Maher ER (2015) VHL, the story of a tumour suppressor gene. *Nat. Rev. Cancer* **15:** 55–64

Grassi L, Alfonsi R, Francescangeli F, Signore M, De Angelis ML, Addario A, Costantini M, Flex E, Ciolfi A, Pizzi S, Bruselles A, Pallocca M, Simone G, Haoui M, Falchi M, Milella M, Sentinelli S, Di Matteo P, Stellacci E, Gallucci M, et al (2019) Organoids as a new model for improving regenerative medicine and cancer personalized therapy in renal diseases. *Cell Death Dis.* **10:** 201

Grigoryan T, Wend P, Klaus A & Birchmeier W (2008) Deciphering the function of canonical Wnt signals in development and disease: conditional loss- and gain-of-function mutations of beta-catenin in mice. *Genes Dev.* **22:** 2308–2341

Grinat J, Heuberger J, Vidal RO, Goveas N, Kosel F, Berenguer-Llergo A, Kranz A, Wulf-Goldenberg A, Behrens D, Melcher B, Sauer S, Vieth M, Batlle E, Stewart AF & Birchmeier W (2020) The epigenetic regulator Mll1 is required for Wnt-driven intestinal tumorigenesis and cancer stemness. *Nat. Commun.* **11:** 6422

Gu Y-F, Cohn S, Christie A, McKenzie T, Wolff N, Do QN, Madhuranthakam AJ, Pedrosa I, Wang T, Dey A, Busslinger M, Xie X-J, Hammer RE, McKay RM, Kapur P & Brugarolas J (2017) Modeling Renal Cell Carcinoma in Mice: Bap1 and Pbrm1 Inactivation Drive Tumor Grade. *Cancer Discov.* **7:** 900–917

Guinot A, Lehmann H, Wild PJ & Frew IJ (2016) Combined deletion of Vhl , Trp53 and Kif3a causes cystic and neoplastic renal lesions. *J. Pathol.* **239:** 365–373

Gustafsson M V., Zheng X, Pereira T, Gradin K, Jin S, Lundkvist J, Ruas JL, Poellinger L, Lendahl U & Bondesson M (2005) Hypoxia Requires Notch Signaling to Maintain the Undifferentiated Cell State. *Dev. Cell* **9:** 617–628

Haase VH, Glickman JN, Socolovsky M & Jaenisch R (2001) Vascular tumors in livers with targeted inactivation of the von Hippel-Lindau tumor suppressor. *Proc. Natl. Acad. Sci.* **98:** 1583–1588

Harada N, Tamai Y, Ishikawa T, Sauer B, Takaku K, Oshima M & Taketo MM (1999) Intestinal polyposis in mice with a dominant stable mutation of the beta-catenin gene. *EMBO J.* **18:** 5931–5942

Harlander S, Schönenberger D, Toussaint NC, Prummer M, Catalano A, Brandt L, Moch H, Wild PJ & Frew IJ (2017) Combined mutation in Vhl, Trp53 and Rb1 causes clear cell renal cell carcinoma in mice. *Nat. Med.* **23:** 869–877

Hendriks D, Artegiani B, Hu H, Chuva de Sousa Lopes S & Clevers H (2021) Establishment of human fetal

hepatocyte organoids and CRISPR–Cas9-based gene knockin and knockout in organoid cultures from human liver. *Nat. Protoc.* **16:** 182–217

Herbst A, Jurinovic V, Krebs S, Thieme SE, Blum H, Göke B & Kolligs FT (2014) Comprehensive analysis of β-catenin target genes in colorectal carcinoma cell lines with deregulated Wnt/β-catenin signaling. *BMC Genomics* **15:** 74

Hill SJ, Decker B, Roberts EA, Horowitz NS, Muto MG, Worley MJ, Feltmate CM, Nucci MR, Swisher EM, Nguyen H, Yang C, Morizane R, Kochupurakkal BS, Do KT, Konstantinopoulos PA, Liu JF, Bonventre J V., Matulonis UA, Shapiro GI, Berkowitz RS, et al (2018) Prediction of DNA Repair Inhibitor Response in Short-Term Patient-Derived Ovarian Cancer Organoids. *Cancer Discov.* **8:** 1404–1421

Hoefflin R, Harlander S, Schäfer S, Metzger P, Kuo F, Schönenberger D, Adlesic M, Peighambari A, Seidel P, Chen C, Consenza-Contreras M, Jud A, Lahrmann B, Grabe N, Heide D, Uhl FM, Chan TA, Duyster J, Zeiser R, Schell C, et al (2020) HIF-1α and HIF-2α differently regulate tumour development and inflammation of clear cell renal cell carcinoma in mice. *Nat. Commun.* **11:** 4111

Holland JD, Györffy B, Vogel R, Eckert K, Valenti G, Fang L, Lohneis P, Elezkurtaj S, Ziebold U & Birchmeier W (2013) Combined Wnt/β-Catenin, Met, and CXCL12/CXCR4 Signals Characterize Basal Breast Cancer and Predict Disease Outcome. *Cell Rep.* **5:** 1214–1227

Holmberg FE, Seidelin JB, Yin X, Mead BE, Tong Z, Li Y, Karp JM & Nielsen OH (2017) Culturing human intestinal stem cells for regenerative applications in the treatment of inflammatory bowel disease. *EMBO Mol. Med.* **9:** 558–570

Hoorn EJ, Nelson JH, McCormick JA & Ellison DH (2011) The WNK Kinase Network Regulating Sodium, Potassium, and Blood Pressure. *J. Am. Soc. Nephrol.* **22:** 605–614

Hou W & Ji Z (2018) Generation of autochthonous mouse models of clear cell renal cell carcinoma: mouse models of renal cell carcinoma. *Exp. Mol. Med.* **50:** 30

Hsieh JJ, Purdue MP, Signoretti S, Swanton C, Albiges L, Schmidinger M, Heng DY, Larkin J & Ficarra V (2017) Renal cell carcinoma. *Nat. Rev. Dis. Prim.* **3:** 17009

Hsu R-J, Ho J-Y, Cha T-L, Yu D-S, Wu C-L, Huang W-P, Chu P, Chen Y-H, Chen J-T & Yu C-P (2012) WNT10A Plays an Oncogenic Role in Renal Cell Carcinoma by Activating WNT/β-catenin Pathway. *PLoS One* **7:** e47649

Hu J, Guan W, Liu P, Dai J, Tang K, Xiao H, Qian Y, Sharrow AC, Ye Z, Wu L & Xu H (2017) Endoglin Is Essential for the Maintenance of Self-Renewal and Chemoresistance in Renal Cancer Stem Cells. *Stem Cell Reports* **9:** 464–477

Huang L, Holtzinger A, Jagan I, BeGora M, Lohse I, Ngai N, Nostro C, Wang R, Muthuswamy LB, Crawford HC, Arrowsmith C, Kalloger SE, Renouf DJ, Connor AA, Cleary S, Schaeffer DF, Roehrl M, Tsao M-S, Gallinger S, Keller G, et al (2015) Ductal pancreatic cancer modeling and drug screening using human pluripotent stem cell– and patient-derived tumor organoids. *Nat. Med.* **21:** 1364–1371

Hülsken J, Birchmeier W & Behrens J (1994) E-cadherin and APC compete for the interaction with beta-catenin and the cytoskeleton. *J. Cell Biol.* **127:** 2061–2069

Janssens N, Andries L, Janicot M, Perera T & Bakker A (2004) Alteration of Frizzled Expression in Renal Cell Carcinoma. *Tumor Biol.* **25:** 161–171

Johansson E, Rönö B, Johansson M, Lindgren D, Möller C, Axelson H & Smith EMK (2016) Simultaneous targeted activation of Notch1 and Vhl-disruption in the kidney proximal epithelial tubular cells in mice. *Sci. Rep.* **6:** 30739

Joosten SC, Smits KM, Aarts MJ, Melotte V, Koch A, Tjan-Heijnen VC & van Engeland M (2018) Epigenetics in renal cell cancer: mechanisms and clinical applications. *Nat. Rev. Urol.* **15:** 430–451

Jung Y-S & Park J-I (2020) Wnt signaling in cancer: therapeutic targeting of Wnt signaling beyond β-catenin and the destruction complex. *Exp. Mol. Med.* **52:** 183–191

Kaidi A, Williams AC & Paraskeva C (2007) Interaction between β-catenin and HIF-1 promotes cellular adaptation to hypoxia. *Nat. Cell Biol.* **9:** 210–217

Kaler P & Prasad R (2007) Molecular cloning and functional characterization of novel zinc transporter rZip10 (Slc39a10) involved in zinc uptake across rat renal brush-border membrane. *Am. J. Physiol. Physiol.*

292: F217–F229

Kanai Y, Clémençon B, Simonin A, Leuenberger M, Lochner M, Weisstanner M & Hediger MA (2013) The SLC1 high-affinity glutamate and neutral amino acid transporter family. *Mol. Aspects Med.* **34:** 108–120

Kandoth C, McLellan MD, Vandin F, Ye K, Niu B, Lu C, Xie M, Zhang Q, McMichael JF, Wyczalkowski MA, Leiserson MDM, Miller CA, Welch JS, Walter MJ, Wendl MC, Ley TJ, Wilson RK, Raphael BJ & Ding L (2013) Mutational landscape and significance across 12 major cancer types. *Nature* **502:** 333–339

Kang HM, Huang S, Reidy K, Han SH, Chinga F & Susztak K (2016) Sox9-Positive Progenitor Cells Play a Key Role in Renal Tubule Epithelial Regeneration in Mice. *Cell Rep.* **14:** 861–871

Karthaus WR, Iaquinta PJ, Drost J, Gracanin A, van Boxtel R, Wongvipat J, Dowling CM, Gao D, Begthel H, Sachs N, Vries RGJ, Cuppen E, Chen Y, Sawyers CL & Clevers HC (2014) Identification of Multipotent Luminal Progenitor Cells in Human Prostate Organoid Cultures. *Cell* **159:** 163–175

Kersten K, Visser KE, Miltenburg MH & Jonkers J (2017) Genetically engineered mouse models in oncology research and cancer medicine. *EMBO Mol. Med.* **9:** 137–153

Kim M, Mun H, Sung CO, Cho EJ, Jeon H-J, Chun S-M, Jung DJ, Shin TH, Jeong GS, Kim DK, Choi EK, Jeong S-Y, Taylor AM, Jain S, Meyerson M & Jang SJ (2019) Patient-derived lung cancer organoids as in vitro cancer models for therapeutic screening. *Nat. Commun.* **10:** 3991

Kim Y, Kang YK, Kim JB, Han SA, Kim K Il & Paik SR (2000) β-Catenin expression and mutational analysis in renal cell carcinomas. *Pathol. Int.* **50:** 725–730

Kimura K, Iwano M, Higgins DF, Yamaguchi Y, Nakatani K, Harada K, Kubo A, Akai Y, Rankin EB, Neilson EG, Haase VH & Saito Y (2008) Stable expression of HIF-1α in tubular epithelial cells promotes interstitial fibrosis. *Am. J. Physiol. Physiol.* **295:** F1023–F1029

Klaus A & Birchmeier W (2008) Wnt signalling and its impact on development and cancer. *Nat. Rev. Cancer* **8:** 387–398

Koch U, Lehal R & Radtke F (2013) Stem cells living with a Notch. *Development* **140:** 689–704

Kopan R & Ilagan MXG (2009) The Canonical Notch Signaling Pathway: Unfolding the Activation Mechanism. *Cell* **137:** 216–233

Kotecha RR, Motzer RJ & Voss MH (2019) Towards individualized therapy for metastatic renal cell carcinoma. *Nat. Rev. Clin. Oncol.* **16:** 621–633

Koury MJ & Haase VH (2015) Anaemia in kidney disease: harnessing hypoxia responses for therapy. *Nat. Rev. Nephrol.* **11:** 394–410

Kreso A & Dick JE (2014) Evolution of the Cancer Stem Cell Model. *Cell Stem Cell* **14:** 275–291

Kretzschmar K & Clevers H (2016) Organoids: Modeling Development and the Stem Cell Niche in a Dish. *Dev. Cell* **38:** 590–600

Kruck S, Eyrich C, Scharpf M, Sievert K-D, Fend F, Stenzl A & Bedke J (2013) Impact of an Altered Wnt1/β-Catenin Expression on Clinicopathology and Prognosis in Clear Cell Renal Cell Carcinoma. *Int. J. Mol. Sci.* **14:** 10944–10957

Kumar S, Liu J, Pang P, Krautzberger AM, Reginensi A, Akiyama H, Schedl A, Humphreys BD & McMahon AP (2015) Sox9 Activation Highlights a Cellular Pathway of Renal Repair in the Acutely Injured Mammalian Kidney. *Cell Rep.* **12:** 1325–1338

Kusaba T, Lalli M, Kramann R, Kobayashi A & Humphreys BD (2014) Differentiated kidney epithelial cells repair injured proximal tubule. *Proc. Natl. Acad. Sci.* **111:** 1527–1532

Lahjouji K, Aouameur R, Bissonnette P, Coady MJ, Bichet DG & Lapointe J-Y (2007) Expression and functionality of the Na+/myo-inositol cotransporter SMIT2 in rabbit kidney. *Biochim. Biophys. Acta - Biomembr.* **1768:** 1154–1159

Lancaster MA & Knoblich JA (2014) Organogenesis in a dish: Modeling development and disease using organoid technologies. *Science* **345:** 1247125

de Lau W, Peng WC, Gros P & Clevers H (2014) The R-spondin/Lgr5/Rnf43 module: regulator of Wnt signal strength. *Genes Dev.* **28:** 305–316

Ledford H & Callaway E (2019) Biologists who decoded how cells sense oxygen win medicine Nobel. *Nature* **574:** 161–162

Lee JN, Chun SY, Lee HJ, Ha Y-S, Kim HT, Yoo ES, Kwon TG & Kim T-H (2016) High Notch1 Expression Correlates with Tumor Stage and Size in Clear Cell Renal Cell Carcinoma. *Korean J. Urol. Oncol.* **14:** 130–137

Lee JW, Chou C-L & Knepper MA (2015) Deep Sequencing in Microdissected Renal Tubules Identifies Nephron Segment–Specific Transcriptomes. *J. Am. Soc. Nephrol.* **26:** 2669–2677

Lee SH, Hu W, Matulay JT, Silva M V., Owczarek TB, Kim K, Chua CW, Barlow LJ, Kandoth C, Williams AB, Bergren SK, Pietzak EJ, Anderson CB, Benson MC, Coleman JA, Taylor BS, Abate-Shen C, McKiernan JM, Al-Ahmadie H, Solit DB, et al (2018) Tumor Evolution and Drug Response in Patient-Derived Organoid Models of Bladder Cancer. *Cell* **173:** 515-528.e17

Leung JY & Kim WY (2017) Bap1 and Pbrm1: Determinants of Tumor Grade and mTOR Activation in VHL-Deficient Mouse Models of Renal Cell Carcinoma. *Cancer Discov.* **7:** 802–804

Li M & Izpisua Belmonte JC (2019) Organoids — Preclinical Models of Human Disease. *N. Engl. J. Med.* **380:** 569–579

Lian X, Duan X, Wu X, Li C, Chen S, Wang S, Cai Y & Weng Z (2012) Expression and Clinical Significance of Von Hippel-Lindau Downstream Genes: Jade-1 and β-Catenin Related to Renal Cell Carcinoma. *Urology* **80:** 485.e7-485.e13

Liao J, Yu Z, Chen Y, Bao M, Zou C, Zhang H, Liu D, Li T, Zhang Q, Li J, Cheng J & Mo Z (2020) Single-cell RNA sequencing of human kidney. *Sci. Data* **7:** 4

Lin S-L, Li B, Rao S, Yeo E-J, Hudson TE, Nowlin BT, Pei H, Chen L, Zheng JJ, Carroll TJ, Pollard JW, McMahon AP, Lang RA & Duffield JS (2010) Macrophage Wnt7b is critical for kidney repair and regeneration. *Proc. Natl. Acad. Sci.* **107:** 4194–4199

Lindgren D, Eriksson P, Krawczyk K, Nilsson H, Hansson J, Veerla S, Sjölund J, Höglund M, Johansson ME & Axelson H (2017) Cell-Type-Specific Gene Programs of the Normal Human Nephron Define Kidney Cancer Subtypes. *Cell Rep.* **20:** 1476–1489

Lindgren D, Sjölund J & Axelson H (2018) Tracing Renal Cell Carcinomas back to the Nephron. *Trends in Cancer* **4:** 472–484

Little MH & Kairath P (2017) Does Renal Repair Recapitulate Kidney Development? *J. Am. Soc. Nephrol.* **28:** 34–46

Liu J, Sato C, Cerletti M & Wagers A (2010) Notch Signaling in the Regulation of Stem Cell Self-Renewal and Differentiation. *Curr. Top. Dev. Biol.* **92:** 367–409.

Liu S, Ma X, Ai Q, Huang Q, Shi T, Zhu M, Wang B & Zhang X (2013) NOTCH1 functions as an oncogene by regulating the PTEN/PI3K/AKT pathway in clear cell renal cell carcinoma. *Urol. Oncol. Semin. Orig. Investig.* **31:** 938–948

Liu Y (2011) Cellular and molecular mechanisms of renal fibrosis. *Nat. Rev. Nephrol.* **7:** 684–696

Lytle NK, Barber AG & Reya T (2018) Stem cell fate in cancer growth, progression and therapy resistance. *Nat. Rev. Cancer* **18:** 669–680

Malyszko J, Tesarova P, Capasso G & Capasso A (2020) The link between kidney disease and cancer: complications and treatment. *Lancet* **396:** 277–287

Mamenko M V., Boukelmoune N, Tomilin VN, Zaika OL, Jensen VB, O'Neil RG & Pochynyuk OM (2017) The renal TRPV4 channel is essential for adaptation to increased dietary potassium. *Kidney Int.* **91:** 1398–1409

di Martino S, De Luca G, Grassi L, Federici G, Alfonsi R, Signore M, Addario A, De Salvo L, Francescangeli F, Sanchez M, Tirelli V, Muto G, Sperduti I, Sentinelli S, Costantini M, Pasquini L, Milella M, Haoui M, Simone G, Gallucci M, et al (2018) Renal cancer: new models and approach for personalizing therapy. *J. Exp. Clin. Cancer Res.* **37:** 217

Marx V (2019) A dream of single-cell proteomics. *Nat. Methods* **16:** 809–812

Masereeuw R & Russel FGM (2012) Regulatory Pathways for ATP-binding Cassette Transport Proteins in Kidney Proximal Tubules. *AAPS J.* **14:** 883–894

Matano M, Date S, Shimokawa M, Takano A, Fujii M, Ohta Y, Watanabe T, Kanai T & Sato T (2015) Modeling colorectal cancer using CRISPR-Cas9–mediated engineering of human intestinal organoids. *Nat. Med.* **21:** 256–262

Mathia S, Paliege A, Koesters R, Peters H, Neumayer H-H, Bachmann S & Rosenberger C (2013) Action of hypoxia-inducible factor in liver and kidney from mice with Pax8-rtTA-based deletion of von Hippel-Lindau protein. *Acta Physiol.* **207:** 565–576

Mazumdar J, O'Brien WT, Johnson RS, LaManna JC, Chavez JC, Klein PS & Simon MC (2010) O2 regulates stem cells through Wnt/β-catenin signalling. *Nat. Cell Biol.* **12:** 1007–1013

Mebius RE & Kraal G (2005) Structure and function of the spleen. *Nat. Rev. Immunol.* **5:** 606–616

Meisel CT, Porcheri C & Mitsiadis TA (2020) Cancer Stem Cells, Quo Vadis? The Notch Signaling Pathway in Tumor Initiation and Progression. *Cells* **9:** 1879

Mercado A, Vázquez N, Song L, Cortés R, Enck AH, Welch R, Delpire E, Gamba G & Mount DB (2005) NH2-terminal heterogeneity in the KCC3 K+-Cl− cotransporter. *Am. J. Physiol. Physiol.* **289:** F1246–F1261

Mertins P, Tang LC, Krug K, Clark DJ, Gritsenko MA, Chen L, Clauser KR, Clauss TR, Shah P, Gillette MA, Petyuk VA, Thomas SN, Mani DR, Mundt F, Moore RJ, Hu Y, Zhao R, Schnaubelt M, Keshishian H, Monroe ME, et al (2018) Reproducible workflow for multiplexed deep-scale proteome and phosphoproteome analysis of tumor tissues by liquid chromatography–mass spectrometry. *Nat. Protoc.* **13:** 1632–1661

Method of the Year 2017: Organoids (2018) *Nat. Methods* **15:** 1

Michels BE, Mosa MH, Streibl BI, Zhan T, Menche C, Abou-El-Ardat K, Darvishi T, Członka E, Wagner S, Winter J, Medyouf H, Boutros M & Farin HF (2020) Pooled In Vitro and In Vivo CRISPR-Cas9 Screening Identifies Tumor Suppressors in Human Colon Organoids. *Cell Stem Cell* **26:** 782-792.e7

Mitchell TJ, Turajlic S, Rowan A, Nicol D, Farmery JHR, O'Brien T, Martincorena I, Tarpey P, Angelopoulos N, Yates LR, Butler AP, Raine K, Stewart GD, Challacombe B, Fernando A, Lopez JI, Hazell S, Chandra A, Chowdhury S, Rudman S, et al (2018) Timing the Landmark Events in the Evolution of Clear Cell Renal Cell Cancer: TRACERx Renal. *Cell* **173:** 611-623.e17

Molenaar M, van de Wetering M, Oosterwegel M, Peterson-Maduro J, Godsave S, Korinek V, Roose J, Destrée O & Clevers H (1996) XTcf-3 Transcription Factor Mediates β-Catenin-Induced Axis Formation in Xenopus Embryos. *Cell* **86:** 391–399

Monteil V, Kwon H, Prado P, Hagelkrüys A, Wimmer RA, Stahl M, Leopoldi A, Garreta E, Hurtado del Pozo C, Prosper F, Romero JP, Wirnsberger G, Zhang H, Slutsky AS, Conder R, Montserrat N, Mirazimi A & Penninger JM (2020) Inhibition of SARS-CoV-2 Infections in Engineered Human Tissues Using Clinical-Grade Soluble Human ACE2. *Cell* **181:** 905-913.e7

Morizane R & Bonventre J V. (2017a) Generation of nephron progenitor cells and kidney organoids from human pluripotent stem cells. *Nat. Protoc.* **12:** 195–207

Morizane R & Bonventre J V. (2017b) Kidney Organoids: A Translational Journey. *Trends Mol. Med.* **23:** 246–263

Morizane R, Lam AQ, Freedman BS, Kishi S, Valerius MT & Bonventre J V. (2015) Nephron organoids derived from human pluripotent stem cells model kidney development and injury. *Nat. Biotechnol.* **33:** 1193–1200

Morris MR & Latif F (2017) The epigenetic landscape of renal cancer. *Nat. Rev. Nephrol.* **13:** 47–60

Murtaugh LC, Stanger BZ, Kwan KM & Melton DA (2003) Notch signaling controls multiple steps of pancreatic differentiation. *Proc. Natl. Acad. Sci.* **100:** 14920–14925

Myszczyszyn A, Czarnecka AM, Matak D, Szymanski L, Lian F, Kornakiewicz A, Bartnik E, Kukwa W, Kieda C & Szczylik C (2015) The Role of Hypoxia and Cancer Stem Cells in Renal Cell Carcinoma

Pathogenesis. *Stem Cell Rev. Rep.* **11:** 919–943

Nanki K, Toshimitsu K, Takano A, Fujii M, Shimokawa M, Ohta Y, Matano M, Seino T, Nishikori S, Ishikawa K, Kawasaki K, Togasaki K, Takahashi S, Sukawa Y, Ishida H, Sugimoto S, Kawakubo H, Kim J, Kitagawa Y, Sekine S, et al (2018) Divergent Routes toward Wnt and R-spondin Niche Independency during Human Gastric Carcinogenesis. *Cell* **174:** 856-869.e17

Nanus DM & Gudas LJ (2016) The Tale of Two Hypoxia-Inducible Factors in Renal Cell Carcinoma. *Eur. Urol.* **69:** 658–659

Nargund AM, Pham CG, Dong Y, Wang PI, Osmangeyoglu HU, Xie Y, Aras O, Han S, Oyama T, Takeda S, Ray CE, Dong Z, Berge M, Hakimi AA, Monette S, Lekaye CL, Koutcher JA, Leslie CS, Creighton CJ, Weinhold N, et al (2017) The SWI/SNF Protein PBRM1 Restrains VHL-Loss-Driven Clear Cell Renal Cell Carcinoma. *Cell Rep.* **18:** 2893–2906

Nassar D & Blanpain C (2016) Cancer Stem Cells: Basic Concepts and Therapeutic Implications. *Annu. Rev. Pathol. Mech. Dis.* **11:** 47–76

Nielsen R, Christensen EI & Birn H (2016) Megalin and cubilin in proximal tubule protein reabsorption: from experimental models to human disease. *Kidney Int.* **89:** 58–67

Ntziachristos P, Lim JS, Sage J & Aifantis I (2014) From Fly Wings to Targeted Cancer Therapies: A Centennial for Notch Signaling. *Cancer Cell* **25:** 318–334

Nusse R & Clevers H (2017) Wnt/β-Catenin Signaling, Disease, and Emerging Therapeutic Modalities. *Cell* **169:** 985–999

O'Rourke KP, Loizou E, Livshits G, Schatoff EM, Baslan T, Manchado E, Simon J, Romesser PB, Leach B, Han T, Pauli C, Beltran H, Rubin MA, Dow LE & Lowe SW (2017) Transplantation of engineered organoids enables rapid generation of metastatic mouse models of colorectal cancer. *Nat. Biotechnol.* **35:** 577–582

Panciera T, Azzolin L, Cordenonsi M & Piccolo S (2017) Mechanobiology of YAP and TAZ in physiology and disease. *Nat. Rev. Mol. Cell Biol.* **18:** 758–770

Park J, Shrestha R, Qiu C, Kondo A, Huang S, Werth M, Li M, Barasch J & Suszták K (2018) Single-cell transcriptomics of the mouse kidney reveals potential cellular targets of kidney disease. *Science* **360:** 758–763

Park JW, Lee JK, Phillips JW, Huang P, Cheng D, Huang J & Witte ON (2016) Prostate epithelial cell of origin determines cancer differentiation state in an organoid transformation assay. *Proc. Natl. Acad. Sci.* **113:** 4482–4487

Peruzzi B, Athauda G & Bottaro DP (2006) The von Hippel-Lindau tumor suppressor gene product represses oncogenic beta-catenin signaling in renal carcinoma cells. *Proc. Natl. Acad. Sci.* **103:** 14531–14536

Posadas EM, Limvorasak S & Figlin RA (2017) Targeted therapies for renal cell carcinoma. *Nat. Rev. Nephrol.* **13:** 496–511

Praetorius J, Kim Y-H, Bouzinova E V., Frische S, Rojek A, Aalkjær C & Nielsen S (2004) NBCn1 is a basolateral Na+-HCO3- cotransporter in rat kidney inner medullary collecting ducts. *Am. J. Physiol. Renal Physiol.* **286:** F903–F912

Praktiknjo SD, Obermayer B, Zhu Q, Fang L, Liu H, Quinn H, Stoeckius M, Kocks C, Birchmeier W & Rajewsky N (2020) Tracing tumorigenesis in a solid tumor model at single-cell resolution. *Nat. Commun.* **11:** 991

Pritchett TL, Bader HL, Henderson J & Hsu T (2015) Conditional inactivation of the mouse von Hippel–Lindau tumor suppressor gene results in wide-spread hyperplastic, inflammatory and fibrotic lesions in the kidney. *Oncogene* **34:** 2631–2639

Qian C-N, Knol J, Igarashi P, Lin F, Zylstra U, Teh BT & Williams BO (2005) Cystic Renal Neoplasia Following Conditional Inactivation of Apc in Mouse Renal Tubular Epithelium. *J. Biol. Chem.* **280:** 3938–3945

Quinn HM, Vogel R, Popp O, Mertins P, Lan L, Messerschmidt C, Landshammer A, Lisek K, Chateau-Joubert S, Marangoni E, Koren E, Fuchs Y & Birchmeier W (2021) YAP and β-catenin cooperate to drive oncogenesis in basal breast cancer. *Cancer Res.*: canres.2801.2020

Ranganathan P, Weaver KL & Capobianco AJ (2011) Notch signalling in solid tumours: a little bit of everything but not all the time. *Nat. Rev. Cancer* **11:** 338–351

Rankin EB, Tomaszewski JE & Haase VH (2006) Renal Cyst Development in Mice with Conditional Inactivation of the von Hippel-Lindau Tumor Suppressor. *Cancer Res.* **66:** 2576–2583

Ricketts CJ, De Cubas AA, Fan H, Smith CC, Lang M, Reznik E, Bowlby R, Gibb EA, Akbani R, Beroukhim R, Bottaro DP, Choueiri TK, Gibbs RA, Godwin AK, Haake S, Hakimi AA, Henske EP, Hsieh JJ, Ho TH, Kanchi RS, et al (2018) The Cancer Genome Atlas Comprehensive Molecular Characterization of Renal Cell Carcinoma. *Cell Rep.* **23:** 313-326.e5

Ringel T, Frey N, Ringnalda F, Janjuha S, Cherkaoui S, Butz S, Srivatsa S, Pirkl M, Russo G, Villiger L, Rogler G, Clevers H, Beerenwinkel N, Zamboni N, Baubec T & Schwank G (2020) Genome-Scale CRISPR Screening in Human Intestinal Organoids Identifies Drivers of TGF-β Resistance. *Cell Stem Cell* **26:** 431-440.e8

Rinkevich Y, Montoro DT, Contreras-Trujillo H, Harari-Steinberg O, Newman AM, Tsai JM, Lim X, Van-Amerongen R, Bowman A, Januszyk M, Pleniceanu O, Nusse R, Longaker MT, Weissman IL & Dekel B (2014) In Vivo Clonal Analysis Reveals Lineage-Restricted Progenitor Characteristics in Mammalian Kidney Development, Maintenance, and Regeneration. *Cell Rep.* **7:** 1270–1283

Ritchie ME, Phipson B, Wu D, Hu Y, Law CW, Shi W & Smyth GK (2015) limma powers differential expression analyses for RNA-sequencing and microarray studies. *Nucleic Acids Res.* **43:** e47

Romagnani P, Remuzzi G, Glassock R, Levin A, Jager KJ, Tonelli M, Massy Z, Wanner C & Anders H-J (2017) Chronic kidney disease. *Nat. Rev. Dis. Prim.* **3:** 17088

Rookmaaker MB, Schutgens F, Verhaar MC & Clevers H (2015) Development and application of human adult stem or progenitor cell organoids. *Nat. Rev. Nephrol.* **11:** 546–554

Saadi-Kheddouci S, Berrebi D, Romagnolo B, Cluzeaud F, Peuchmaur M, Kahn A, Vandewalle A & Perret C (2001) Early development of polycystic kidney disease in transgenic mice expressing an activated mutant of the β-catenin gene. *Oncogene* **20:** 5972–5981

Sachs N, de Ligt J, Kopper O, Gogola E, Bounova G, Weeber F, Balgobind AV, Wind K, Gracanin A, Begthel H, Korving J, van Boxtel R, Duarte AA, Lelieveld D, van Hoeck A, Ernst RF, Blokzijl F, Nijman IJ, Hoogstraat M, van de Ven M, et al (2018) A Living Biobank of Breast Cancer Organoids Captures Disease Heterogeneity. *Cell* **172:** 373-386.e10

Sagrinati C, Netti GS, Mazzinghi B, Lazzeri E, Liotta F, Frosali F, Ronconi E, Meini C, Gacci M, Squecco R, Carini M, Gesualdo L, Francini F, Maggi E, Annunziato F, Lasagni L, Serio M, Romagnani S & Romagnani P (2006) Isolation and Characterization of Multipotent Progenitor Cells from the Bowman's Capsule of Adult Human Kidneys. *J. Am. Soc. Nephrol.* **17:** 2443–2456

Saini S, Majid S & Dahiya R (2011) The complex roles of Wnt antagonists in RCC. *Nat. Rev. Urol.* **8:** 690–699

Sanchez-Vega F, Mina M, Armenia J, Chatila WK, Luna A, La KC, Dimitriadoy S, Liu DL, Kantheti HS, Saghafinia S, Chakravarty D, Daian F, Gao Q, Bailey MH, Liang W-W, Foltz SM, Shmulevich I, Ding L, Heins Z, Ochoa A, et al (2018) Oncogenic Signaling Pathways in The Cancer Genome Atlas. *Cell* **173:** 321-337.e10

Sansom OJ, Griffiths DFR, Reed KR, Winton DJ & Clarke AR (2005) Apc deficiency predisposes to renal carcinoma in the mouse. *Oncogene* **24:** 8205–8210

Sansom OJ, Meniel V, Wilkins JA, Cole AM, Oien KA, Marsh V, Jamieson TJ, Guerra C, Ashton GH, Barbacid M & Clarke AR (2006) Loss of Apc allows phenotypic manifestation of the transforming properties of an endogenous K-ras oncogene in vivo. *Proc. Natl. Acad. Sci.* **103:** 14122–14127

Sato T & Clevers H (2015) SnapShot: Growing Organoids from Stem Cells. *Cell* **161:** 1700-1700.e1

Sato T, Stange DE, Ferrante M, Vries RGJ, van Es JH, van den Brink S, van Houdt WJ, Pronk A, van Gorp J, Siersema PD & Clevers H (2011) Long-term Expansion of Epithelial Organoids From Human Colon, Adenoma, Adenocarcinoma, and Barrett's Epithelium. *Gastroenterology* **141:** 1762–1772

Sato T, Vries RG, Snippert HJ, van de Wetering M, Barker N, Stange DE, van Es JH, Abo A, Kujala P, Peters PJ & Clevers H (2009) Single Lgr5 stem cells build crypt-villus structures in vitro without a mesenchymal niche. *Nature* **459:** 262–265

Sato Y, Yoshizato T, Shiraishi Y, Maekawa S, Okuno Y, Kamura T, Shimamura T, Sato-Otsubo A, Nagae G, Suzuki H, Nagata Y, Yoshida K, Kon A, Suzuki Y, Chiba K, Tanaka H, Niida A, Fujimoto A, Tsunoda T, Morikawa T, et al (2013) Integrated molecular analysis of clear-cell renal cell carcinoma. *Nat. Genet.* **45:** 860–867

Saygin C, Matei D, Majeti R, Reizes O & Lathia JD (2019) Targeting Cancer Stemness in the Clinic: From Hype to Hope. *Cell Stem Cell* **24:** 25–40

Schödel J, Grampp S, Maher ER, Moch H, Ratcliffe PJ, Russo P & Mole DR (2016) Hypoxia, Hypoxia-inducible Transcription Factors, and Renal Cancer. *Eur. Urol.* **69:** 646–657

Schönenberger D, Harlander S, Rajski M, Jacobs RA, Lundby A-K, Adlesic M, Hejhal T, Wild PJ, Lundby C & Frew IJ (2016) Formation of Renal Cysts and Tumors in Vhl/Trp53 -Deficient Mice Requires HIF1α and HIF2α. *Cancer Res.* **76:** 2025–2036

Schönig K, Schwenk F, Rajewsky K & Bujard H (2002) Stringent doxycycline dependent control of CRE recombinase in vivo. *Nucleic Acids Res.* **30:** e134

Schouten LJ, Deckers IAG, van den Brandt PA, Baldewijns MMLL & van Engeland M (2016) Alcohol and Dietary Folate Intake and Promoter CpG Island Methylation in Clear-Cell Renal Cell Cancer. *Nutr. Cancer* **68:** 1097–1107

Schulz N, Dave MH, Stehberger PA, Chau T & Wagner CA (2007) Differential localization of vacuolar H+-ATPases containing a1, a2, a3, or a4 (ATP6V0A1-4) subunit isoforms along the nephron. *Cell. Physiol. Biochem.* ***20*****:** 109–120

Schumacher K, Strehl R & Minuth WW (2003) Urea Restrains Aldosterone-Induced Development of Peanut Agglutinin-Binding on Embryonic Renal Collecting Duct Epithelia. *J. Am. Soc. Nephrol.* **14:** 2758–2766

Schutgens F & Clevers H (2020) Human Organoids: Tools for Understanding Biology and Treating Diseases. *Annu. Rev. Pathol. Mech. Dis.* **15:** 211–234

Schutgens F, Rookmaaker MB, Blokzijl F, van Boxtel R, Vries R, Cuppen E, Verhaar MC & Clevers H (2017) Troy/TNFRSF19 marks epithelial progenitor cells during mouse kidney development that continue to contribute to turnover in adult kidney. *Proc. Natl. Acad. Sci.* **114:** E11190–E11198

Schutgens F, Rookmaaker MB, Margaritis T, Rios A, Ammerlaan C, Jansen J, Gijzen L, Vormann M, Vonk A, Viveen M, Yengej FY, Derakhshan S, de Winter-de Groot KM, Artegiani B, van Boxtel R, Cuppen E, Hendrickx APA, van den Heuvel-Eibrink MM, Heitzer E, Lanz H, et al (2019) Tubuloids derived from human adult kidney and urine for personalized disease modeling. *Nat. Biotechnol.* **37:** 303–313

Schwarz-Romond T, Fiedler M, Shibata N, Butler PJG, Kikuchi A, Higuchi Y & Bienz M (2007) The DIX domain of Dishevelled confers Wnt signaling by dynamic polymerization. *Nat. Struct. Mol. Biol.* **14:** 484–492

Seino T, Kawasaki S, Shimokawa M, Tamagawa H, Toshimitsu K, Fujii M, Ohta Y, Matano M, Nanki K, Kawasaki K, Takahashi S, Sugimoto S, Iwasaki E, Takagi J, Itoi T, Kitago M, Kitagawa Y, Kanai T & Sato T (2018) Human Pancreatic Tumor Organoids Reveal Loss of Stem Cell Niche Factor Dependence during Disease Progression. *Cell Stem Cell* **22:** 454-467.e6

Shibue T & Weinberg RA (2017) EMT, CSCs, and drug resistance: the mechanistic link and clinical implications. *Nat. Rev. Clin. Oncol.* **14:** 611–629

Shimokawa M, Ohta Y, Nishikori S, Matano M, Takano A, Fujii M, Date S, Sugimoto S, Kanai T & Sato T (2017) Visualization and targeting of LGR5+ human colon cancer stem cells. *Nature* **545:** 187–192

Siebel C & Lendahl U (2017) Notch Signaling in Development, Tissue Homeostasis, and Disease. *Physiol. Rev.* **97:** 1235–1294

Siegel RL, Miller KD, Fuchs HE & Jemal A (2021) Cancer Statistics, 2021. *CA. Cancer J. Clin.* **71:** 7–33

Sjölund J, Johansson M, Manna S, Norin C, Pietras A, Beckman S, Nilsson E, Ljungberg B & Axelson H (2008) Suppression of renal cell carcinoma growth by inhibition of Notch signaling in vitro and in vivo. *J. Clin. Invest.* **118:** 217–228

Snippert HJ, van der Flier LG, Sato T, van Es JH, van den Born M, Kroon-Veenboer C, Barker N, Klein AM, van Rheenen J, Simons BD & Clevers H (2010) Intestinal Crypt Homeostasis Results from Neutral Competition between Symmetrically Dividing Lgr5 Stem Cells. *Cell* **143:** 134–144

Soriano P (1999) Generalized lacZ expression with the ROSA26 Cre reporter strain. *Nat. Genet.* **21:** 70–71

Sorrentino G, Ruggeri N, Zannini A, Ingallina E, Bertolio R, Marotta C, Neri C, Cappuzzello E, Forcato M, Rosato A, Mano M, Bicciato S & Del Sal G (2017) Glucocorticoid receptor signalling activates YAP in breast cancer. *Nat. Commun.* **8:** 14073

de Sousa e Melo F, Kurtova A V., Harnoss JM, Kljavin N, Hoeck JD, Hung J, Anderson JE, Storm EE, Modrusan Z, Koeppen H, Dijkgraaf GJP, Piskol R & de Sauvage FJ (2017) A distinct role for Lgr5+ stem cells in primary and metastatic colon cancer. *Nature* **543:** 676–680

Stow LR & Gumz ML (2011) The Circadian Clock in the Kidney. *J. Am. Soc. Nephrol.* **22:** 598–604

Sturmlechner I, Durik M, Sieben CJ, Baker DJ & van Deursen JM (2017) Cellular senescence in renal ageing and disease. *Nat. Rev. Nephrol.* **13:** 77–89

Takasato M, Er PX, Chiu HS & Little MH (2016) Generation of kidney organoids from human pluripotent stem cells. *Nat. Protoc.* **11:** 1681–1692

Takasato M, Er PX, Chiu HS, Maier B, Baillie GJ, Ferguson C, Parton RG, Wolvetang EJ, Roost MS, Chuva de Sousa Lopes SM & Little MH (2015) Kidney organoids from human iPS cells contain multiple lineages and model human nephrogenesis. *Nature* **526:** 564–568

Takebe N, Miele L, Harris PJ, Jeong W, Bando H, Kahn M, Yang SX & Ivy SP (2015) Targeting Notch, Hedgehog, and Wnt pathways in cancer stem cells: clinical update. *Nat. Rev. Clin. Oncol.* **12:** 445–464

Takeda H, Kataoka S, Nakayama M, Ali MAE, Oshima H, Yamamoto D, Park J-W, Takegami Y, An T, Jenkins NA, Copeland NG & Oshima M (2019) CRISPR-Cas9–mediated gene knockout in intestinal tumor organoids provides functional validation for colorectal cancer driver genes. *Proc. Natl. Acad. Sci.* **116:** 15635–15644

Takeichi M (1991) Cadherin cell adhesion receptors as a morphogenetic regulator. *Science* **251:** 1451–1455

Tiriac H, Belleau P, Engle DD, Plenker D, Deschênes A, Somerville TDD, Froeling FEM, Burkhart RA, Denroche RE, Jang G-H, Miyabayashi K, Young CM, Patel H, Ma M, LaComb JF, Palmaira RLD, Javed AA, Huynh JC, Johnson M, Arora K, et al (2018) Organoid Profiling Identifies Common Responders to Chemotherapy in Pancreatic Cancer. *Cancer Discov.* **8:** 1112–1129

Tomasetti C, Li L & Vogelstein B (2017) Stem cell divisions, somatic mutations, cancer etiology, and cancer prevention. *Science* **355:** 1330–1334

Traykova-Brauch M, Schönig K, Greiner O, Miloud T, Jauch A, Bode M, Felsher DW, Glick AB, Kwiatkowski DJ, Bujard H, Horst J, von Knebel Doeberitz M, Niggli FK, Kriz W, Gröne H-J & Koesters R (2008) An efficient and versatile system for acute and chronic modulation of renal tubular function in transgenic mice. *Nat. Med.* **14:** 979–984

Trepiccione F, Gerber SD, Grahammer F, López-Cayuqueo KI, Baudrie V, Păunescu TG, Capen DE, Picard N, Alexander RT, Huber TB, Chambrey R, Brown D, Houillier P, Eladari D & Simons M (2016) Renal Atp6ap2/(Pro)renin Receptor Is Required for Normal Vacuolar H+-ATPase Function but Not for the Renin-Angiotensin System. *J. Am. Soc. Nephrol.* **27:** 3320–3330

Turajlic S, Xu H, Litchfield K, Rowan A, Chambers T, Lopez JI, Nicol D, O'Brien T, Larkin J, Horswell S, Stares M, Au L, Jamal-Hanjani M, Challacombe B, Chandra A, Hazell S, Eichler-Jonsson C, Soultati A, Chowdhury S, Rudman S, et al (2018a) Tracking Cancer Evolution Reveals Constrained Routes to Metastases: TRACERx Renal. *Cell* **173:** 581-594.e12

Turajlic S, Xu H, Litchfield K, Rowan A, Horswell S, Chambers T, O'Brien T, Lopez JI, Watkins TBK, Nicol D, Stares M, Challacombe B, Hazell S, Chandra A, Mitchell TJ, Au L, Eichler-Jonsson C, Jabbar F, Soultati A, Chowdhury S, et al (2018b) Deterministic Evolutionary Trajectories Influence Primary Tumor Growth: TRACERx Renal. *Cell* **173:** 595-610.e11

Tuveson D & Clevers H (2019) Cancer modeling meets human organoid technology. *Science* **364:** 952–955

Uchimura K, Wu H, Yoshimura Y & Humphreys BD (2020) Human Pluripotent Stem Cell-Derived Kidney Organoids with Improved Collecting Duct Maturation and Injury Modeling. *Cell Rep.* **33:** 108514

Visvader JE & Lindeman GJ (2012) Cancer Stem Cells: Current Status and Evolving Complexities. *Cell Stem Cell* **10:** 717–728

Vlachogiannis G, Hedayat S, Vatsiou A, Jamin Y, Fernández-Mateos J, Khan K, Lampis A, Eason K, Huntingford I, Burke R, Rata M, Koh D-M, Tunariu N, Collins D, Hulkki-Wilson S, Ragulan C, Spiteri I, Moorcraft SY, Chau I, Rao S, et al (2018) Patient-derived organoids model treatment response of metastatic gastrointestinal cancers. *Science* **359:** 920–926

van Vlodrop IJH, Joosten SC, De Meyer T, Smits KM, Van Neste L, Melotte V, Baldewijns MMLL, Schouten LJ, van den Brandt PA, Jeschke J, Yi JM, Schuebel KE, Ahuja N, Herman JG, Aarts MJ, Bosman FT, Van Criekinge W & van Engeland M (2017) A Four-Gene Promoter Methylation Marker Panel Consisting of GREM1, NEURL, LAD1, and NEFH Predicts Survival of Clear Cell Renal Cell Cancer Patients. *Clin. Cancer Res.* **23:** 2006–2018

Vogelstein B, Papadopoulos N, Velculescu VE, Zhou S, Diaz LA & Kinzler KW (2013) Cancer Genome Landscapes. *Science* **339:** 1546–1558

Wang S-S, Gu Y-F, Wolff N, Stefanius K, Christie A, Dey A, Hammer RE, Xie X-J, Rakheja D, Pedrosa I, Carroll T, McKay RM, Kapur P & Brugarolas J (2014a) Bap1 is essential for kidney function and cooperates with Vhl in renal tumorigenesis. *Proc. Natl. Acad. Sci.* **111:** 16538–16543

Wang S, Gao D & Chen Y (2017) The potential of organoids in urological cancer research. *Nat. Rev. Urol.* **14:** 401–414

Wang W, Yu Y, Wang Y, Li X, Bao J, Wu G, Chang H, Shi T & Yue Z (2014b) Delta-like ligand 4: A predictor of poor prognosis in clear cell renal cell carcinoma. *Oncol. Lett.* **8:** 2627–2633

Wend P, Fang L, Zhu Q, Schipper JH, Loddenkemper C, Kosel F, Brinkmann V, Eckert K, Hindersin S, Holland JD, Lehr S, Kahn M, Ziebold U & Birchmeier W (2013) Wnt/β-catenin signalling induces MLL to create epigenetic changes in salivary gland tumours. *EMBO J.* **32:** 1977–1989

van de Wetering M, Francies HE, Francis JM, Bounova G, Iorio F, Pronk A, van Houdt W, van Gorp J, Taylor-Weiner A, Kester L, McLaren-Douglas A, Blokker J, Jaksani S, Bartfeld S, Volckman R, van Sluis P, Li VSW, Seepo S, Sekhar Pedamallu C, Cibulskis K, et al (2015) Prospective Derivation of a Living Organoid Biobank of Colorectal Cancer Patients. *Cell* **161:** 933–945

Wiese KE, Nusse R & van Amerongen R (2018) Wnt signalling: conquering complexity. *Development* **145:** dev165902

Wong DWL, Yiu WH, Chan KW, Li Y, Li B, Lok SWY, Taketo MM, Igarashi P, Chan LYY, Leung JCK, Lai KN & Tang SCW (2018) Activated renal tubular Wnt/β-catenin signaling triggers renal inflammation during overload proteinuria. *Kidney Int.* **93:** 1367–1383

Woolf AS (2019) Growing a new human kidney. *Kidney Int.* **96:** 871–882

Wu H, Uchimura K, Donnelly EL, Kirita Y, Morris SA & Humphreys BD (2018) Comparative Analysis and Refinement of Human PSC-Derived Kidney Organoid Differentiation with Single-Cell Transcriptomics. *Cell Stem Cell* **23:** 869-881.e8

Wu K, Xu L, Zhang L, Lin Z & Hou J (2011) High Jagged1 Expression Predicts Poor Outcome in Clear Cell Renal Cell Carcinoma. *Jpn. J. Clin. Oncol.* **41:** 411–416

Yi Y, Polosukhina D, Love HD, Hembd A, Pickup M, Moses HL, Lovvorn HN, Zent R & Clark PE (2015) A Murine Model of K-RAS and β-Catenin Induced Renal Tumors Expresses High Levels of E2F1 and Resembles Human Wilms Tumor. *J. Urol.* **194:** 1762–1770

Young AP, Schlisio S, Minamishima YA, Zhang Q, Li L, Grisanzio C, Signoretti S & Kaelin WG (2008) VHL loss actuates a HIF-independent senescence programme mediated by Rb and p400. *Nat. Cell Biol.* **10:** 361–369

Young MD, Mitchell TJ, Vieira Braga FA, Tran MGB, Stewart BJ, Ferdinand JR, Collord G, Botting RA, Popescu D-M, Loudon KW, Vento-Tormo R, Stephenson E, Cagan A, Farndon SJ, Del Castillo Velasco-Herrera M, Guzzo C, Richoz N, Mamanova L, Aho T, Armitage JN, et al (2018) Single-cell transcriptomes from human kidneys reveal the cellular identity of renal tumors. *Science* **361:** 594–599

Yousef Yengej FA, Jansen J, Rookmaaker MB, Verhaar MC & Clevers H (2020) Kidney Organoids and Tubuloids. *Cells* **9:** 1326

Yu ASL (2015) Claudins and the Kidney. *J. Am. Soc. Nephrol.* **26:** 11–19

Zanconato F, Forcato M, Battilana G, Azzolin L, Quaranta E, Bodega B, Rosato A, Bicciato S, Cordenonsi M

& Piccolo S (2015) Genome-wide association between YAP/TAZ/TEAD and AP-1 at enhancers drives oncogenic growth. *Nat. Cell Biol.* **17:** 1218–1227

Zhang J, Wu T, Simon J, Takada M, Saito R, Fan C, Liu X-D, Jonasch E, Xie L, Chen X, Yao X, Teh BT, Tan P, Zheng X, Li M, Lawrence C, Fan J, Geng J, Liu X, Hu L, et al (2018) VHL substrate transcription factor ZHX2 as an oncogenic driver in clear cell renal cell carcinoma. *Science* **361:** 290–295

Zheng X, Linke S, Dias JM, Zheng X, Gradin K, Wallis TP, Hamilton BR, Gustafsson M, Ruas JL, Wilkins S, Bilton RL, Brismar K, Whitelaw ML, Pereira T, Gorman JJ, Ericson J, Peet DJ, Lendahl U & Poellinger L (2008) Interaction with factor inhibiting HIF-1 defines an additional mode of cross-coupling between the Notch and hypoxia signaling pathways. *Proc. Natl. Acad. Sci.* **105:** 3368–3373

Zhou D, Li Y, Lin L, Zhou L, Igarashi P & Liu Y (2012) Tubule-specific ablation of endogenous β-catenin aggravates acute kidney injury in mice. *Kidney Int.* **82:** 537–547

Zhu L, Finkelstein D, Gao C, Shi L, Wang Y, López-Terrada D, Wang K, Utley S, Pounds S, Neale G, Ellison D, Onar-Thomas A & Gilbertson RJ (2016) Multi-organ Mapping of Cancer Risk. *Cell* **166:** 1132-1146.e7

Zhu Q, Fang L, Heuberger J, Kranz A, Schipper J, Scheckenbach K, Vidal RO, Sunaga-Franze DY, Müller M, Wulf-Goldenberg A, Sauer S & Birchmeier W (2019) The Wnt-Driven Mll1 Epigenome Regulates Salivary Gland and Head and Neck Cancer. *Cell Rep.* **26:** 415-428.e5

Acknowledgements

I would like to thank:

Urological Research Foundation (Stiftung Urologische Forschung) in Berlin for funding me for more than 5 years and Max Delbrück Center for Molecular Medicine (MDC) for my short-term funding. MDC and Berlin School of Integrative Oncology (BSIO) for funding my consumables and attendance to conferences and soft skill workshops.

Prof. Dr. Walter Birchmeier for teaching me how to think, write and talk like a scientist, how to link different concepts and ask relevant questions in the field of preclinical cancer models, how to critically evaluate experimental results and how to overcome my weaknesses, improve and not give up.

Dr. Annika Fendler for theoretical and technical guidance during the first years of my Ph.D. research phase and Simone Jung for performing some routine experiments.

My collaborators from the core technology platforms of the MDC, Dr. Philipp Mertins and Dr. Oliver Popp for phospho-proteomics, Dr. Severine Kunz for electron microscopy, Dr. Anje Sporbert for confocal microscopy and Dr. Hans-Peter Rahn for FACS.

Prof. Dr. med. Wolfgang Schneider and Dr. med. Ann-Christin von Brünneck from the Institute of Pathology at the Charité – Medical University of Berlin for histopathological examinations.

Prof. Dr. Achim Leutz and Prof. Dr. med. Friedrich Luft for critical feedback during my three Thesis Committee Meetings. Prof. Dr. Achim Leutz and Prof. Dr. Michael Hummel for preparing reviews of my dissertation.

Marion Müller and Dr. Kamil Lisek for a true friendship, honest and accurate advice and a joyful atmosphere every day.

Selbständigkeitserklärung

Hiermit erkläre ich, dass ich die vorliegende Abschlussarbeit selbständig verfasst habe und sämtliche Quellen, einschließlich Internetquellen, die unverändert oder abgewandelt wiedergegeben werden, insbesondere Quellen für Texte, Grafiken, Tabellen und Bilder, als solche kenntlich gemacht habe.

Ich versichere, dass ich die vorliegende Abschlussarbeit noch nicht für andere Prüfungen eingereicht habe.

Mir ist bekannt, dass bei Verstößen gegen diese Grundsätze ein Verfahren wegen Täuschungsversuchs bzw. Täuschung gemäß der fachspezifischen Prüfungsordnung und/oder der Fächerübergreifenden Satzung zur Regelung von Zulassung, Studium und Prüfung der Humboldt-Universität zu Berlin (ZSP-HU) eingeleitet wird.

Berlin, 31.03.2021
Adam Myszczyszyn